High-Q Optical Micro-cavity Resonators as High Sensitive Bio-chemical and Ultrasonic Sensors

By

Tao Ling

A dissertation submitted in partial fulfillment
of the requirements for the degree of
Doctor of Philosophy
(Electrical Engineering)
in The University of Michigan
2012

Doctoral Committee:

Professor L. Jay Guo, Chair

Associate Professor Xudong Fan

Assistant Professor Tal Carmon

Assistant Professor Pei-Cheng Ku

To My Family

Acknowledgements

First and foremost I would like to express my deepest gratitude to my advisor, Professor L. Jay Guo, for his supports and guidance throughout my Ph.D. study, and also the freedom that he gave to me during my 5 years research life in the University of Michigan. His scientific intuition and experienced advice are crucial to overcome problems in both theoretical and experimental aspects. I have truly learned a lot of from him.

I would also like to thank my doctoral committee members, Professor Xudong Fan, Professor Tal Carmon and Professor P.C Ku, for their useful comment and advice to the work in my thesis. Some part of the bio-chemical sensing experiment is performed with the help of Dr. Sheereen Majd and Professor Michel Mayer in Biomedical Engineering Department. Also I will like to say thanks to Professor Xueding Wang and Dr. Zhixing Xie for useful discussion and share the knowledge of the photo-acoustic field.

I would like to thank all Guo group former and current members. Former members: Dr. Chung-Yen Chao trained me on the optical measurement before I joined Guo group. Dr. Jingsung Kim served as my mentor in the cleanroom during my first year in University of Michigan and transferred useful fabrication knowledge to me. Dr. Dawen Li helped a lot in my first year's life in UM. Dr. Li-Jing Cheng, Dr. Myunggyu Kang, Dr. Pran Mukherjee helped with all kinds of fabrication process problems related to dry etch, nano-imprint and furnace process. Dr. Philip Choi helped to solve various problems on

Nanonex machine, Dr. Carlos Pina helped to prepare SSQ materials for imprinting applications, Dr. Se Hyun An helped with some flexible mold preparations and some useful discussion with Dr. Yi-Hao Chen and Dr. Ting Xu. All kinds of helps from current members: Dr. Haofei Shi, Dr. Moon Kyu Kwak, Dr. Jin zhou, Yikuei Wu, Xing Tu, Hyoung Won Baac, Sung-Liang Chen, Alex Kaplan, Hyunsoo Kim, Brandon Lucas, Jong G. Ok, Hui Joon Park, Ashwin Panday, Cheng Zhang, Peng Zhu, JaeYong Lee, Kyu-Tae Lee.

Out of Guo group, I would like to say thinks to all my friends and classmates in the UM, Weiming Wang , Chenan Xia, Meng Zhang, Guang Huang, Professor Wei Guo, Xiuquan Ma, Jun Yang, Professor Zetian Mi, etc. Also thanks to all SSEL staff for helping on various fabrication problems.

Finally, I would like to give my sincere appreciation to my parents, my wife and my elder sister, without their continuous support, I can not go that far.

Table of Contents

List of Figures

Abstract

High-Q Optical Micro-cavity Resonators as High Sensitive Bio-chemical and Ultrasonic Sensors

by

Tao Ling

Chair: L. Jay Guo

Optical micro-cavity resonators have quickly emerged in the past few years as a new sensing platform in a wide range of applications, such as bio-chemical molecular detection, environmental monitoring, acoustic and electromagnetic waves detection. In this thesis, we will mainly focus on developing high sensitivity silica micro-tube resonator bio-chemical sensors and high sensitivity polymer micro-ring resonator acoustic sensors.

In high sensitivity silica micro-tube resonator bio-chemical sensors part: We first demonstrated a prism coupled silica micro-tube bio-chemical sensing platform to overcome the reliability problem in a fiber coupled thin wall silica micro-tube sensing platform. In refractive index sensing experiment, a unique resonance mode with sensitivity around 600nm/refractive index unit (RIU) has been observed. Surface sensing experiments also have been performed in this platform to detect lipid monolayer, lipid bilayer, electrostatic self assemble layer-by-layer as well as the interaction between the lipid bilayer and proteins. Then a theoretical study on various sensing properties on the

silica micro-tube based sensing platform has been realized. Furthermore, we have proposed a coupled cavity system to further enhance the device's sensitivity above 1000nm/RIU.

In high sensitivity polymer micro-ring resonator acoustic sensors part: We first presented a simplified fabrication process and realized a polymer microring with a Q factor around 6000. The fabricated device has been used to detect acoustic wave with noise equivalent pressure (NEP) around 230Pa over 1-75MHz frequency rang, which is comparable to state-of-art piezoelectric transducer and the device's frequency response also have been characterized to be up to 90MHz. A new fabrication process combined with resist reflow and thermal oxidation process has been used to improve the Q factor up to 10^5 and the device's NEP has been tested to be around 88Pa over 1-75MHz range. Further improving the device's Q factor has been realized by shifting the device's working wavelength to near-visible wavelength and further reducing the device's sidewall roughness. A record new high Q~$4x10^5$ has been measured and the device's NEP as low as 21Pa has been measured. Furthermore, a smaller size polymer microring device has been developed and fabricated to realize larger angle beam forming applications.

Chapter 1

Introduction

Optical micro-cavity resonators have been extensively studied from later of 20 century to now in many applications. In 1969, Marcatili first proposed micro-ring resonators as integrated optical wavelength filters [1]. Microsphere [2] and micro-droplet [3] resonators have been investigated from early of 1980's to realize lasing and nonlinear optical process. Until 1990s, chip based micro-cavity resonators have been fabricated with the mature of semiconductor technology [4]. Those micro-cavity resonators have shown several advantage properties, such as high Q factor, narrow resonance line-width, compact size and strong optical filed enhancement inside cavities. With these unique characteristics, micro-cavity resonators have been demonstrated lots of applications in both optical passive and active devices. Micro-cavity resonator based optical passive devices included: single resonator/high-order resonators filters [5,6], add/drop filters in wavelength division multiplexing (WDM) system [7,8], tunable filters [9,10], bio-chemical sensors[11-15], mechanical sensors [16] and pressure sensors[17,18]. Micro-cavity resonator based optical active devices included: continuous wavelength lasers [19,20], Raman lasers[21,22], optical switcher/modulators[23-25], optical nonlinear oscillators[26,27,28] and cavity based radiation pressure effects [29] In this introduction, we will mainly introduce the optical micro-cavity based bio-chemical sensors and ultrasonic sensors.

1.1 Optical microcavity based bio-chemical sensors

Recently, micro-cavity resonator based bio-chemical sensors have been raised a lot of attentions because of their unique properties which can reduce the device size by order of magnitude, without sacrificing the interaction length by virtue of the high quality (Q) factor resonances, thereby significantly reducing the amount of sample needed for the detection. The resonance effect also provides an effective long interaction length for the sensor to achieve sufficient sensitivity. Also typical bio-sensing experiment requires that the devices can handle aqueous analytes. Therefore fluidic handling capability is an indispensable part of the sensor platform. High quality-factor microsphere cavities using Whispering Gallery Mode (WGM) resonances have been demonstrated to respond to a monolayer of protein adsorption [11], however integration with fluidic system is very challenging and typically requires fluidic chambers much larger than the active device element. Though micro-ring [11,30] and micro-disk [12] sensors can be mass fabricated using batch processing techniques, they suffer from limited Q factors due to the surface roughness induced scattering loss.

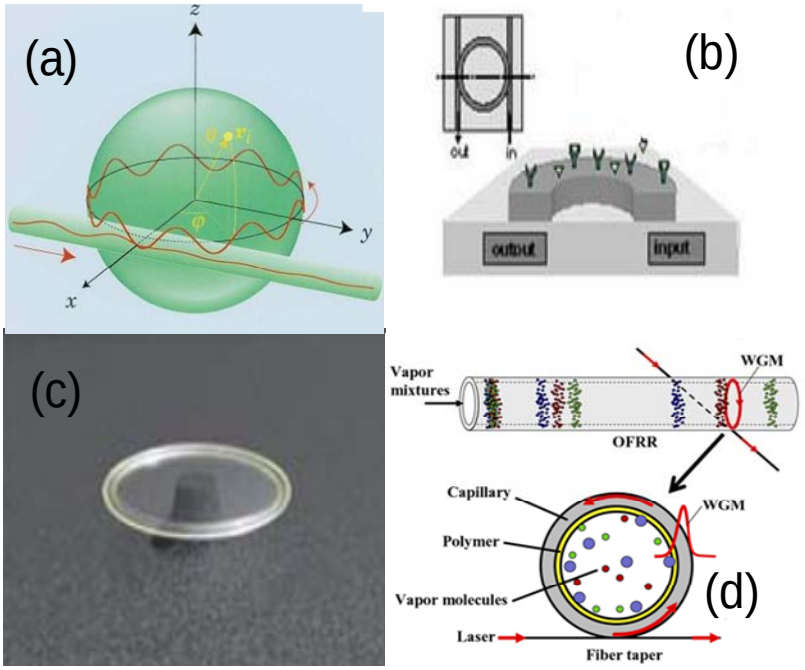

Figure1.1 Various optical micro-cavity biochemical sensors: (a) microsphere [11], (b) microring [28], (c) microdisk [12], micro-tube [15]

The silica micro-tube based resonator sensor is very attractive for biochemical sensing application due to its ability to handle aqueous analytes and its high Q factor [31]. The high-Q (~10^6) is a result of the low scattering loss due to very smooth surfaces and long virtual interaction length. However there are also limitations to the micro-tube resonators. Since only the inner surface can be used as the sensor interface, so the total evanescence optical field interacting with the solutions is less than half that of micro-ring [32] resonators if the two devices have similar field distribution for the guided and evanescent waves, thereby resulting in a lower sensitivity. Moreover, the previously demonstrated micro-tube resonator sensors required a tube thickness of less than 5 microns [15] in order to obtain a refractive index sensitivity of 2.6nm/RIU. Significantly higher index sensitivity can be obtained by further reducing the wall thickness to below sub-micron [33]. But such strategies cause the micro-tube to be very brittle and difficult

to handle in practical sensing applications. In this thesis, we will develop a new strategy to solve this problem to realize reliable and high sensitivity bio-chemical detection.

1.2 Optical microcavity based ultrasonic sensors

Recently, an optical cavity based ultrasound detection platform has attracted increasing attentions [34-37]. Compared with conventional piezoelectric transducers, the new detection platform provides several advantages, such as preserving high sensitivity with reduced element sizes, high-frequency and wideband response with simple fabrication. In this new optical cavity based detection platform, optically transparent polymer material was used because of its high optical elastic coefficient and high deformability, which can provide sensitive response under acoustic pressure. A polymer based fiber tip Fabry-Perot (F-P) cavity ultrasonic hydrophone has been demonstrated with comparable sensitivity and noise equivalent pressure (NEP) to current piezoelectric PVDF ultrasonic sensing devices [36]. An improved sensitivity has been realized in a polymer based plane F-P device by increasing the device's Q factor, which results from an increased reflection of the multi-layer stacks based 1-dimension photonic crystal mirror [37]. Further improvement of the sensitivity can be achieved by further increasing the reflectivity of the 1-D photonic crystal mirror, but requires a sophisticated system to precisely control the thickness and uniformity of the deposited multilayer film. Except the photonic crystal based light confining mechanism, the total internal reflection (TIR) mechanism has been widely used to confine the light in the cavity to achieve much higher Q factor. High Q resonators using the TIR mechanism include micro-spheres [38,11],

micro-disks [39,48], micro-rings [41,42,43] and micro-tubes [15,44]. By combining polymer material's high optical elastic coefficient and high deformability with the TIR-based high Q factor micro-resonators, it is possible to demonstrate high sensitivity ultrasounic detectors.

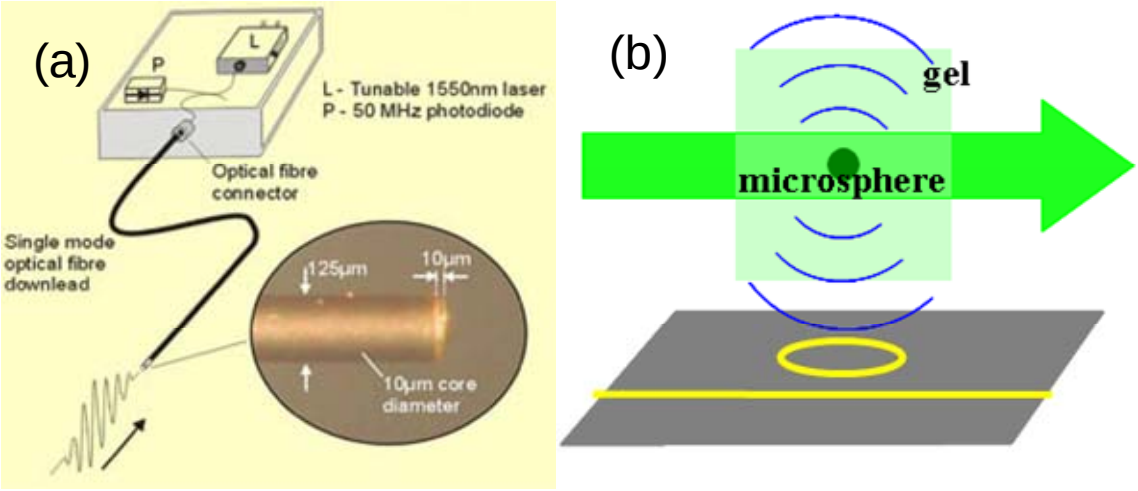

Figure 1.2 (a) Fiber tip Fabry-Perot (F-P) cavity ultrasonic hydrophone (b) On-chip polymer microring ultrasonic hydrophone

1.3 Dissertation overview

Chapter 1 provides a brief introduction of optical micro-cavities and mainly focus on describing optical micro-cavity based bio-chemical sensor and ultrasonic sensors.

Chapter 2 first presents the basic parameters, such as Q factor, free spectrum range (FSR) and fineness. Then the theory of optical micro-cavities is introduced in cylindrical coordinator. Based on this theory, the field distribution in the microring and microtube are provided and at last the optical loss is studied.

Chapter 3 describes to use a prism coupling method to realize a reliable and high sensitivity micro-tube sensing system. In Bulk sensing experiment, a unique high sensitivity 600nm/RIU has been observed and confirmed by simulation. In surface sensing experiment, the detection of lipid monolayer, lipid bilayer, self assemble layer-by-layer have been realized, also the interaction between the lipid membrane and proteins has been studied.

Chapter 4 shows various sensing mechanisms of micro-tube sensors, includes bulk refractive index sensing, surface sensing, absorption sensing. Simulation results of those sensing properties have been well presented. Finally a new coupled cavity system is introduced to realize an ultrahigh sensitivity bio-chemical sensing platform.

Chapter 5 introduces the nano-imprinting technique to fabricate chip-based polymer micro-ring as ultrasonic sensing elements. First a simplified fabrication process has been created to fabrication a polymer micro-ring with similar Q factor as pervious reported. Second, an improved fabricated method has been presented to improve the device's performance by improving the sidewall roughness using resist reflow and thermal oxidation method. A low noise and wideband ultrasonic detection has been demonstrated by using our polymer micro-ring devices.

Chapter 6 presents a new design of polymer micro-ring working at visible wavelength range to reduce material and water absorption loss. A new process has been created to further reduce the device's side wall roughness to realize a polymer microring with Q factor as high as $5x10^5$. Also the device's sensitivity has been greatly improved with the device's extremely high Q factor. Smaller size polymer micro-rings also have been fabricated to realize high frequency beam forming application.

Chapter 7 presents all of the wok done so far and discusses the future experiments to be done

Chapter 2

Optical microcavity resonators

2.1 Introduction

(a)

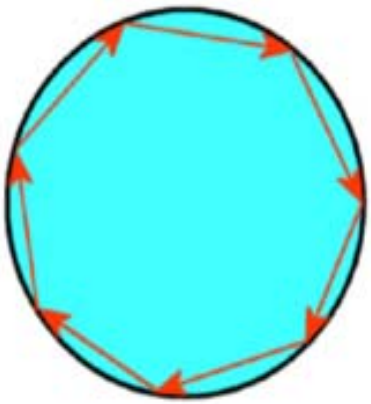

(b)

Figure 2.1 (a) Part of St. Paul's Cathedral in London, (b) Ray optics point of view of whispering gallery mode

Circular optical micro-cavity resonators have been studied over 40 years and the eigen modes of the circular cavities are called whispering gallery modes. Acoustical whispering gallery modes have been studied from early 20 century by Lord Rayleigh [45], in order to explain the curious property of the whispering gallery at the dome of St Paul's Cathedral in London (Figure 2.1(a)). This curious property can be addressed like that if two persons stand at opposite sides of the gallery, and one whispers around the wall of the dome, and the whispers can be heard clearly by another person. This effect does not

work if one speaks at center of the dome or normally to the edge of the dome. The answer to this strange effect is that the sound bounces along the curved wall of the gallery with very little loss, and so it can be heard at a very long distance. The reason that it does not work if you speak at center or normally to the edge of the dome is that the increased amplitude of the noise allows it to circulate the gallery multiple times, and so the sounds all get mixed up and can no longer be heard properly. It can be viewed that there is a narrow region near the edge of the dome where the sound waves propagate with very low loss, and this is known as a "whispering gallery mode" [45] in honor of gallery where it was discovered. This phenomenon which was first observed by sound wave bounding around the edge of the wall, while same picture can also applied to the optical wave by assuming that the inside and the outside of gallery region are filled with high refractive index material, low refractive index optical transparent material, respectively. By choosing properly excitation method, the optical wave can be coupled, generated, confined at the edge of the high refractive index material by the total internal reflection. Figure 2.1(b) shows the ray optical point of view of whispering gallery mode.

In recently, this phenomenon has been found in optical wave region in micro circular cavity, such as micro-disk, micro-ring, microsphere and micro-tube.

2.2 Cavity parameters

2.2.1 Q factor

The most common and important parameter of the cavity is the quality factor (Q factor), the definition of the quality factor for any resonant elements can be simply from one equation [46, 47]:

$$Q = \frac{\omega_0 \cdot U_{cavity}}{P_{Loss}} \tag{2-1}$$

Where the ω_0 is the resonant frequency, U_{cavity} is the store energy in the resonator and P_{Loss} is the power dissipated by the cavity. Also we assume there is no source in the cavity. The P_{Loss} can be written as $P_{loss}=-dU_c/dt$ by the definition. So equation (2-1) can be change to: $\frac{dU_c}{dt} = -\frac{\omega_0}{Q}U_c$, and the solution to this time-dependent differential equation is: $U_c(t) = U_c(0)e^{-\omega_o t/Q} = U_c(0)e^{-t/(Q/\omega_0)}$. So we can define the photon life time in the cavity as:

$$\tau_{ph} = \frac{Q}{\omega_0} \tag{2-2}$$

By using Fourier transfer the cavity Q factor can be measured through the spectrum rather than by using ring down time:

$$Q = \frac{\omega_0}{\Delta\omega} \tag{2-3}$$

Where the ω_0 is the resonant frequency of the cavity, and $\Delta\omega$ is the full width half maximum of the resonant peak.

2.2.2 Free spectrum range

The free spectrum range is defined as the frequency spacing or wavelength spacing between two adjacent modes. If we define the two adjacent modes with resonant wavelength at λ_1 and λ_2, then the Free spectrum range (FSR):

$$\text{FSR}=\lambda_1-\lambda_2 \approx \frac{\lambda_1^2}{L(n_{eff}-\lambda_1\frac{\partial n_{eff}}{\partial \lambda})}=\frac{\lambda_1^2}{L\cdot n_g} \tag{2-4}$$

Where n_{eff} is the effective index of the resonant mode and L is the cavity length.

2.2.3 Finesse (F)

The finesse of a resonator is defined as the ratio of the FSR to the resonant line-width [47]:

$$F=\frac{FSR}{\delta\lambda} \tag{2-5}$$

for an azimuthally symmetric resonance mode, the F can be calculated as F=Q/m, where m is the azimuthal number of the resonance mode. A physical explanation of finesse is the round trip number of the photon in the cavity.

2.3 Optical mode in microtube and microring resonators

Optical modes in a dielectric micro-ring can be obtained by solving the Maxwell equation in cylindrical coordinator. Given the Maxwell equation with no source:

$$\nabla \times \vec{E}(\vec{r},t) = -\frac{\partial \vec{B}(\vec{r},t)}{\partial t} \qquad \nabla \cdot \vec{D}(\vec{r},t) = 0$$

$$\nabla \times \vec{H}(\vec{r},t) = \frac{\partial \vec{D}(\vec{r},t)}{\partial t} \qquad \nabla \cdot \vec{B}(\vec{r},t) = 0 \tag{2-6}$$

Where $\vec{D}(\vec{r},t) = \varepsilon_o \varepsilon_r \vec{E}(\vec{r},t)$ and $\vec{B}(\vec{r},t) = \mu \vec{H}(\vec{r},t)$ are the linear constitutive relations. By considering that all filed $\vec{E}, \vec{D}, \vec{B}, \vec{H}$ have the sinusoidal time dependent term $\exp(-i\omega t)$ and time independent Maxwell equation can be expressed as following:

$$\nabla \times \vec{E}(\vec{r}) = i\omega \vec{B}(\vec{r}) \qquad \nabla \cdot \vec{D}(\vec{r}) = 0$$

$$\nabla \times \vec{H}(\vec{r}) = -i\omega \vec{D}(\vec{r}) \qquad \nabla \cdot \vec{B}(\vec{r}) = 0 \tag{2-7}$$

For micro-ring case, we can get the Helmholtz equation from Maxwell equation and linear constitutive relation:

$$\nabla^2 \vec{F} + k_0^2 n^2(r,\phi,z)\vec{F} = 0 \tag{2-8}$$

where the $\vec{F}$ can be either $\vec{H}$ or $\vec{E}$. The detail of Helmholtz equation in cylindrical coordinates can be written as following:

$$[\frac{\partial^2}{\partial r^2} + \frac{1}{r}\frac{\partial}{\partial r} + \frac{1}{r^2}\frac{\partial^2}{\partial \phi^2} + \frac{\partial^2}{\partial z^2} + k_0^2 n^2(r,\phi,z)]F = 0 \tag{2-9}$$

For TE mode, F can be H_z and for TM mode the F can be E_z. After separate variable we can change the equation to different two equations:

$$\frac{\partial^2 X}{\partial r^2}+\frac{1}{r}\frac{\partial X}{\partial r}+\frac{1}{r^2}\frac{\partial^2 X}{\partial \phi^2}+k_0^2 n_{eff}^2(r,\phi)X=0 \tag{2-10}$$

$$\frac{d^2 Z}{dz^2}+k_0^2[n(z)-n_{eff}^2]Z=0 \tag{2-11}$$

Where $F_z = X(r,\phi)Z(z)$.

Equation (2-10) also can be solved by using separation of variable method by writing: $X(r,\phi)=R(r)\Phi(\phi)$, and then the equation (2-10) can be change to two following equations:

$$\frac{d^2 R}{dr^2}+\frac{1}{r}\frac{\partial R}{\partial r}+[k_0^2 n_{eff}^2(r)-\frac{m^2}{r^2}]R=0 \tag{2-12}$$

$$\frac{d^2\Phi}{d\phi^2}+m^2\Phi=0 \tag{2-13}$$

The solution to equation (2-13) can be simply written as: $\Phi(\phi)=e^{-im\phi}$, where m is the an integer number, and the equation (2-12)'s solution is Bessel function. For integer number Bessel equation's solution should be combination of first order Bessel function J_m and second order Bessel function N_m. But when r=0, the second order Bessel function go to infinity, so inside the micro-ring region the solution just can be first order Bessel function, and outsider use combination of first order and second order Bessel function.

2.4 Mode field distribution

For simplicity, we only consider TM mode, The E_z component can be expressed as:

$$E_z=\begin{cases} B_1 J_m(k_0 n_1 r)\exp[i(m\theta-\omega t)] & 0\le r<R_1 \\ B_2 J_m(k_0 n_2 r)+B_3 N_m(k_0 n_2 r)]\exp[i(m\theta-\omega t)] & R_1\le r<R_2 \\ B_4 H_m^{(1)}(k_0 n_3 r)\exp[i(m\theta-\omega t)] & R_2\le r<+\infty \end{cases} \tag{2-14}$$

where m is the azimuthal order number. At the boundary R_1, E_z field needs to satisfy the boundary condition:

$$E_{z1}(R_1) = E_{z2}(R_1)$$
$$\left.\frac{\partial E_{z1}}{\partial r}\right|_{r=R_1} = \left.\frac{\partial E_{z2}}{\partial r}\right|_{r=R_1} \tag{2-15}$$

This leads to two equations:

$$B_1 J_m(k_0 n_1 R_1) = B_2 J_m(k_0 n_2 R_1) + B_3 N_m(k_0 n_2 R_1) \tag{2-16}$$

$$B_1 n_1 J'_m(k_0 n_1 R_1) = B_2 n_2 J'_m(k_0 n_2 R_1) + B_3 n_2 N'_m(k_0 n_2 R_1) \tag{2-17}$$

At the boundary R_2, E_z field also needs to satisfy the boundary condition:

$$E_{z2}(R_2) = E_{z3}(R_2)$$
$$\left.\frac{\partial E_{z2}}{\partial r}\right|_{r=R_2} = \left.\frac{\partial E_{z3}}{\partial r}\right|_{r=R_2} \tag{2-18}$$

Then we get two more equations

$$B_4 H_m^{(1)}[k_0 n_3 (R+d)] = B_2 J_m[k_0 n_2 (R+d)] + B_3 N_m[k_0 n_2 (R+d)] \tag{2-19}$$

$$B_4 n_3 H'^{(1)}_m[k_0 n_3 (R+d)] = B_2 n_2 J'_m[k_0 n_2 (R+d)] + B_3 n_2 N'_m[k_0 n_2 (R+d)] \tag{2-20}$$

Dividing Eq. (2-16) by Eq.(2-17) and Eq. (2-19) by (2-20) we get:

$$\frac{J_m(k_0 n_1 R_1)}{n_1 J'_m(k_0 n_1 R_1)} = \frac{(B_2/B_3) J_m(k_0 n_2 R_1) + N_m(k_0 n_2 R_1)}{(B_2/B_3) n_2 J'_m(k_0 n_2 R_1) + n_2 N'_m(k_0 n_2 R_1)} \tag{2-21}$$

$$\frac{H_m^{(1)}(k_0 n_1 R_2)}{n_3 H'^{(1)}_m(k_0 n_1 R_2)} = \frac{(B_2/B_3) J_m(k_0 n_2 R_2) + N_m(k_0 n_2 R_2)}{(B_2/B_3) n_2 J'_m(k_0 n_2 R_2) + n_2 N'_m(k_0 n_2 R_2)} \tag{2-22}$$

Form equation (9) we can solve for B_2/B_3:

$$\frac{B_2}{B_3} = \frac{n_2 H_m^{(1)}(k_0 n_1 R_2) N_m'(k_0 n_2 R_2) - n_3 H_m'^{(1)}(k_0 n_1 R_2) N_m(k_0 n_2 R_2)}{n_3 H_m'^{(1)}(k_0 n_1 R_2) J_m(k_0 n_2 R_2) - n_2 H_m^{(1)}(k_0 n_1 R_2) J_m'(k_0 n_2 R_2)} \tag{2-23}$$

Equation (8) and equation (9) or (10) will be used to find the resonance wavelength with different azimuthal numbers in the cavity. We define: $\frac{B_2}{B_3} = C$, then B_2=CB_3

$$B_1 = B_3\left(\frac{CJ_m(k_0 n_2 R_1) + N_m(k_0 n_2 R_1)}{J_m(k_0 n_1 R_1)}\right) = B_3 A_{m1}$$

$$B_4 = B_3\left(\frac{CJ_m(k_0 n_2 R_2) + N_m(k_0 n_2 R_2)}{H_m^{(1)}(k_0 n_3 R_2)}\right) = B_3 A_{m3}$$

Finally the wave equation can be written as:

$$E_z = \begin{cases} B_3\{A_{m1} J_m(k_0 n_1 r)\exp[i(m\theta - \omega t)]\} & 0 \le r < R_1 \\ B_3\{[CJ_m(k_0 n_2 r) + N_m(k_0 n_2 r)]\exp[i(m\theta - \omega t)]\} & R_1 \le r < R_2 \\ B_3\{A_{m3} H_m^{(1)}(k_0 n_3 r)\exp[i(m\theta - \omega t)]\} & R_2 \le r < +\infty \end{cases} \tag{2-24}$$

Where： $A_{m1} = \frac{CJ_m(k_0 n_2 R_1) + N_m(k_0 n_2 R_1)}{J_m(k_0 n_1 R_1)}$, $A_{m3} = \frac{CJ_m(k_0 n_2 R_2) + N_m(k_0 n_2 R_2)}{H_m^{(1)}(k_0 n_3 R_2)}$,

and the parameter B_3 can be obtained from the normalization of the E field.

2.5 Loss in optical micro-cavity

In optical microcavity, due to presence of loss mechanisms, such as radiation loss (confinement loss), material absorption loss and surface scattering loss, energy will be dissipated outside of the cavity. The extent to describe how good the resonant system to

store energy is commonly expressed by the Quality-factor, which is defined by the energy storage time normalized with respect to the period of oscillation

$$Q = \omega_0 \frac{U_{cavity}}{P_{Loss}}$$

Where the ω_0 is the resonant frequency, U_{cavity} is the store energy in the resonator and P_{Loss} is the power dissipated by the cavity. The over all Q factor can be describe as following expression:

$$Q_{total}^{-1} = Q_{absorption.}^{-1} + Q_{radiation}^{-1} + Q_{scattering}^{-1} + Q_{coupling}^{-1} \quad (2\text{-}25)$$

Where Q_{total} , $Q_{absorption}$, $Q_{radiation}$, $Q_{scattering}$, $Q_{coupling}$ are total Q, absorption loss related Q, radiation loss related Q, scattering loss related Q and coupling loss related Q ,respectively. In here we will mainly focus on discussing surface scattering loss and material absorption loss.

2.5.1 Surface scattering loss

In optical waveguides, when the light propagate along the waveguide, random boundary imperfections or surface roughness will scatter the energy out of the waveguide to form the scattering loss. The scattering loss is particularly important when the waveguide is bending, because center of optical filed is shifting away from the center of the waveguide and which will increase the field intensity at the boundary of the waveguide where surface imperfection is located. Thus, the bending waveguide will suffer higher surface scattering loss compared to the straight waveguide with same dimension. The roughness at sidewall is normally generated from photo-lithography step,

metal lift-off step or dry etching step during the device fabrication and it shows a random fashion. Different approaches have been developed to estimate the scattering loss in optical waveguide, such as a volume current method [48], a perturbation approach[49]. One of the simplest ways to describe the scattering loss in straight and bending waveguide can be expressed as following equations [50,51] :

$$\alpha_{scatt,straight} = 2\sigma^2 (n_{eff}^2 - n_{cl}^2) k_0^2 \frac{k_{y,straight}}{\beta} E_s^2 \tag{2-26}$$

$$\alpha_{scatt,bending} = \sigma^2 (n_{eff}^2 - n_{cl}^2) k_0^2 \frac{k_{y,bending}}{\beta} (E_1^2 + E_2^2) \tag{2-27}$$

Where σ is the variance of the surface roughness at the interface, n_{eff} is the effective refractive index of the guided mode in the waveguide and n_{cl} is the refractive index of the cladding

2.5.2 Radiation loss

The optical wave within a straight waveguide can be well confined by total internal reflection at the dielectric and air boundary and guided in the waveguide without loss. However, it is known that total internal reflection at a curved interface is incomplete, and leads to a transmitted wave, which causes loss of optical energy. This loss mechanism is called optical tunneling loss [52] or bending loss. This optical tunneling phenomenon can be understood by drawing an analog to the quantum mechanical treatment of a 1-D particle in a potential well which gives the physical meaning of the bending loss. But an approximation expression of the bending loss will give us more understanding how the bending loss changes with waveguide geometrics. The bending loss can be expressed

as[53]:

$$\alpha_{radiation} = \frac{2\gamma_s^2 k_{y,curved}^2 e^{\gamma_s W}}{(n_{co}^2 - n_{cl}^2) k_0^2 \beta_{curved} (2+\gamma_s W)} \exp\{[\frac{\beta_{curved}}{\gamma_s} \ln(\frac{1+\frac{\gamma_s}{\beta_{curved}}}{1-\frac{\gamma_s}{\beta_{curved}}}) - 2]\gamma_s R_c\} \qquad (2\text{-}28)$$

Where β_{curved} is the propagation constant in curved waveguide, and k_0, $k_{y,\,curved}$, R_c are wave vector in vacuum, k_y in curved waveguide and bending radius of the waveguide, respectively. From this expression, we can clearly see that the bending loss is exponential increasing when the bending radius is reduced. So by choosing a proper bending radius, we can greatly reduce the bending loss in our micro-ring resonator design.

2.5.3 Absorption loss

Silica was used as the material for fabricating the capillary tube which was used as the microcavity resonator in our bio-chemical experiment. Silica has low absorption losses over very board spectrum range. The minimum loss (around 0.2dB/km) located around 1.55 μm wavelength range, for which it has become the operating wavelength for fiber-optic telecommunications. With such low absorption value, the absorption limited Q factor can be calculated to be $Q = \frac{2\pi n_{eff}}{\lambda \alpha} \approx 3x10^{10}$, but normal bio-chemical experiment requires silica microcavity resonator surrounded by water which have very high absorption coefficient at 1.55μm wavelength range, so a silica micro-tube resonator will show a Q factor around 10^4 to 10^6 when it was used as a bio-chemical sensing element.

Polymer material also has been used as optical waveguide material for very long time, because it is easy to be prepared, can be dope with all kinds of functional materials and

can be fabricated on various substrates. But polymer materials have show relative higher absorption loss (around few dB/cm) compared to silica or silicon at telecommunication wavelength range. This is mainly due to carbon-hydrogen bonds harmonic absorption at near-IR range. One possible method to reduce the absorption loss is to replace the H atom in the polymer by F atom. Another possible method to reduce absorption loss is to move device's working wavelength from near IR to visible or near visible wavelength range where polymer materials have shown much lower loss [54], so it has been applied to fabricate polymer optical fiber in short distance optical communication. Recently PMMA has been used to fabricate optical microcavity to shows the material absorption los as low as 0. 0044 dB/cm, yielding Qabs $\approx$ 1. 2 $\times 10^{8}$ [55].

Chapter 3

Prism coupled micro-tubes as sensitive bio-chemical sensors

3.1 Introduction and motivation

Silica capillary tube resonator sensor has attracted a lot of interests on biochemical sensing applications not only due to its ability to handle aqueous analytes, but also its high Q factor., The high-Q (varies from10^4 to 10^6) is a result of the low scattering loss due to its smooth surfaces which is benefited from its high temperature fabrication process. However there are also limitations to the micro-tube resonators. Since only the inner surface can be used as the sensor interface, so the total evanescence optical field interacting with the solutions is less than half that of micro-ring resonators if the two devices have similar field distribution for the guided and evanescent waves, thereby resulting in a lower sensitivity. Moreover, the previously demonstrated micro-tube resonator sensors required a tube thickness of less than 5 microns in order to obtain a refractive index sensitivity of 2.6nm/RIU [15]. Significantly higher index sensitivity can be obtained by further reducing the wall thickness to below sub-micron [33,56],. But such

strategies cause the micro-tube to be very brittle and difficult to handle in practical sensing applications.

In this chapter, we will propose and demonstrate to use the prism coupled thick wall (above 32μm) micro-tube sensor system not only to overcome the reliability problem, but also to realize high sensitivity detection. Bulk refractive index sensing and surface sensing experiments have been demonstrated and experimental results match well with the simulation results. Also this new platform has been used to realize sensitivity surface sensing experiment by detecting lipid monolayer, lipid billayer and electrostatic self assemble layer by layer binding to the inner surface of the microtube. Moreover the interactions between the lipid and protein have been studied.

3.2 Experimental setup

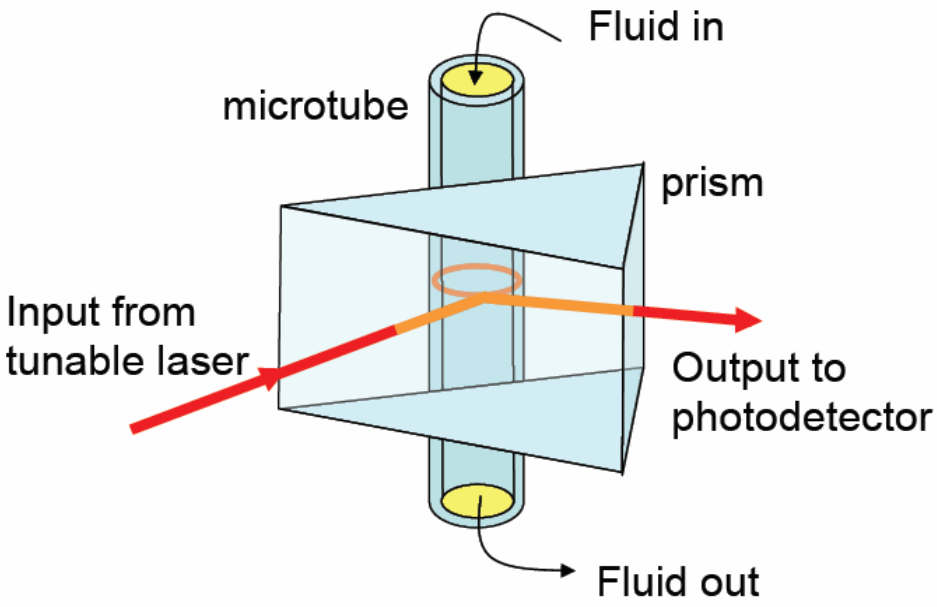

Figure 3.1 Schematic of prism coupled micro-tube sensor system

Figure 3.1 shows the schematic of the experimental setup. Light incident onto a SF11-glass prism was evanescently coupled into a fused silica micro-tube through a controlled air gap. The fused-silica micro-tube was purchased from Polymicro Inc. and has an inner radius of R_1 = 134 μm and an outer radius of R_2 = 166 μm. In our experiment, the silica micro-tube was first connected to two pieces of plastic tube at each end. The analyte solution flowing through the silica tube was controlled by a peristaltic pump. Next, the silica tube was positioned perpendicular to the incident light plane and mounted at the center of the prism. The coupling gap between the micro-tube and the prism was controlled by a deposited Al film with 400-500 nm thickness on one side of the silica micro-tube. The silica micro-tube was then bonded to the prism and mounted on a rotation stage. The output from a wavelength tunable diode laser around 1550 nm wavelength (Santec TSL-220) was collimated by a GRIN lens collimator and incident onto the prism with a spot size of ~ 500um. The incident angle was tuned by rotating the rotation stage so as to satisfy the phase matching condition to the different order resonance modes in the micro-tube resonator. The light reflected from the prism, which was coupled out of the resonator, passed through an aperture and then a polarizer, and finally was focused onto a photo-detector. The polarizer was used to select the TE and TM polarization in the output from the resonator. In our experiment we focused on the measurement of the TE polarization, because the TE mode was observed to posses higher Q factors than did the TM modes.

3.2 Bulk refractive index sensing

3.2.1 Bulk refractive index sensing experiments

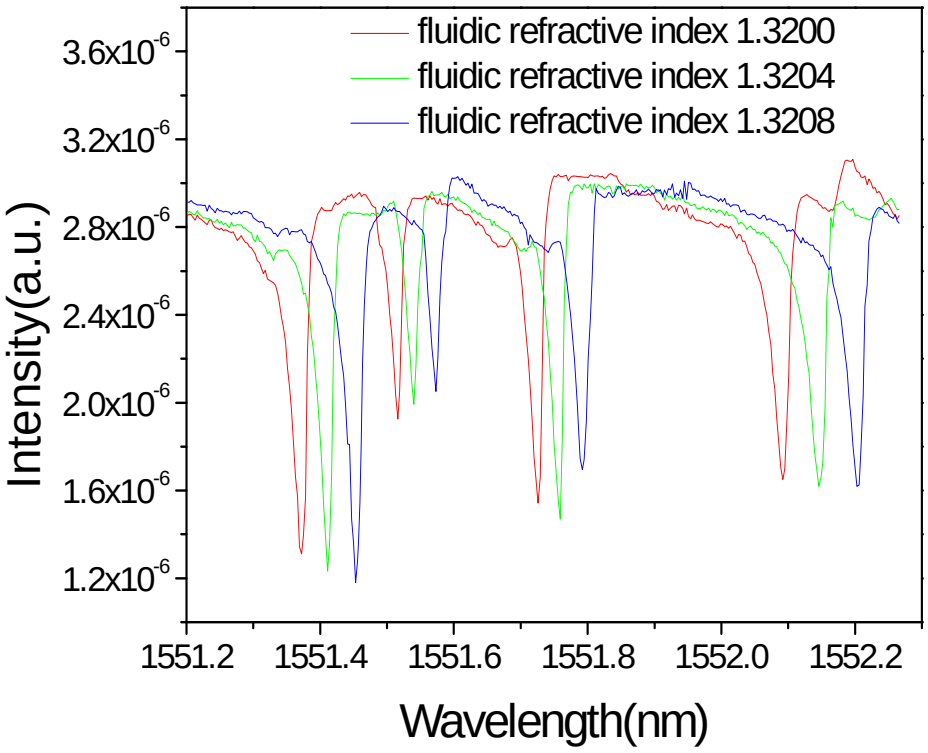

Figure 3.2 Resonance curve shift due to the change of liquid refractive index in the micro-tube at incident angle of 37.5°

The index sensing experiments were performed by changing the refractive index of the liquid that flows through the micro-tube, and simultaneously monitoring the corresponding resonance wavelength shifts. The refractive indices of the liquid were controlled by premixing a very small amount of isopropyl alcohol (IPA) with deionized (DI) water. The refractive index of the solution can be estimated based on the dielectric constants of both liquids and the molar ratio of each component [57]:

$$n = \sqrt{\kappa \cdot n_{IPA}^2 + (1-\kappa) \cdot n_{water}^2} \tag{3-1}$$

where κ is the molar ratio of IPA in the solution. The refractive indices of water and IPA are taken to be 1.320 and 1.378 around the 1550 nm wavelength range

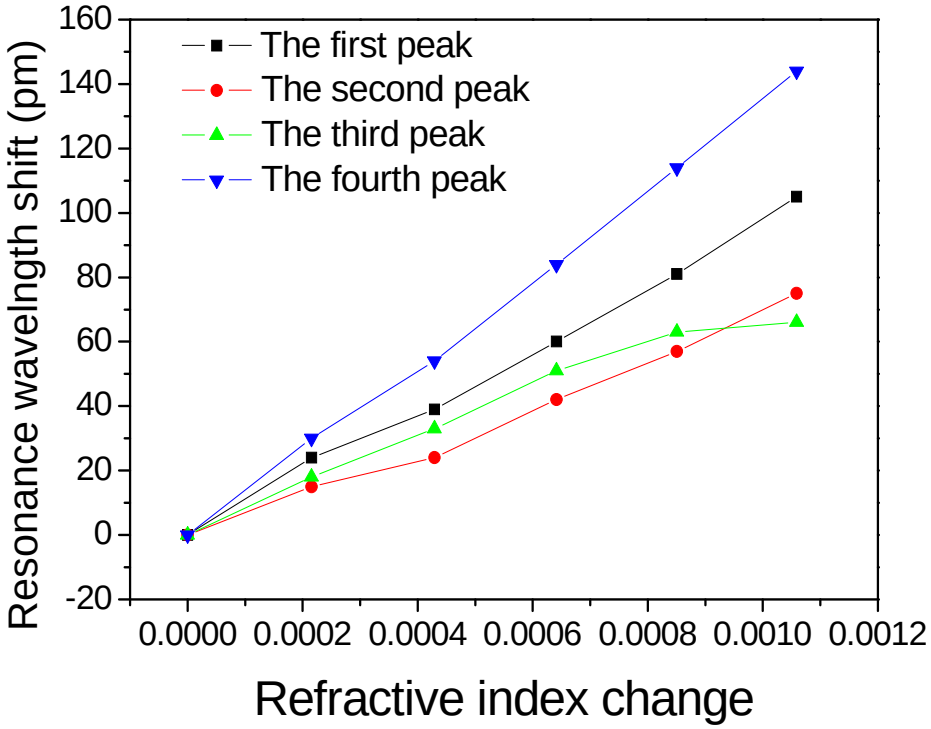

Figure3.3 Resonance wavelength as a function of the change in liquid refractive index in the micro-tube at an incident angle of 37.5^{o}

The beam illuminated on the prism is a Gaussian beam that covers a range of spatial wave vector components. Therefore, the light can be coupled into several resonance modes within a certain wavelength range that satisfies the phase matching condition. Fig. 3.2 shows three resonance spectra measured from the reflected beam for liquids with three different refractive indices filled in the micro-tube. The refractive index difference between each spectrum was ~ 4 x 10^{-4}, and the incident angle to the prism was ~ 37.5^{o}. Four resonant modes are shown in each spectrum. These four resonant modes shift differently for the same fluidic index changes of 4x10^{-4}: the resonance wavelength shift is ~ 39pm for the first peak, ~ 28pm for the second peak, ~ 30pm for the third and ~ 54pm for the fourth. Fig. 3.3 shows the resonant wavelength shifts as a function of the refractive index change. By linearly fitting the curve in Fig. 3.3, the device sensitivity, defined as the resonance shift per unit refractive index unit (RIU) for the four resonance modes are ca. 96.7 nm/RIU, 70 nm/RIU, 74.7 nm/RIU and 135 nm/RIU, respectively.

The sensitivity of these resonance peaks is 40 times higher than the sensitivity reported by White et al., which was about 2.6nm/RIU.

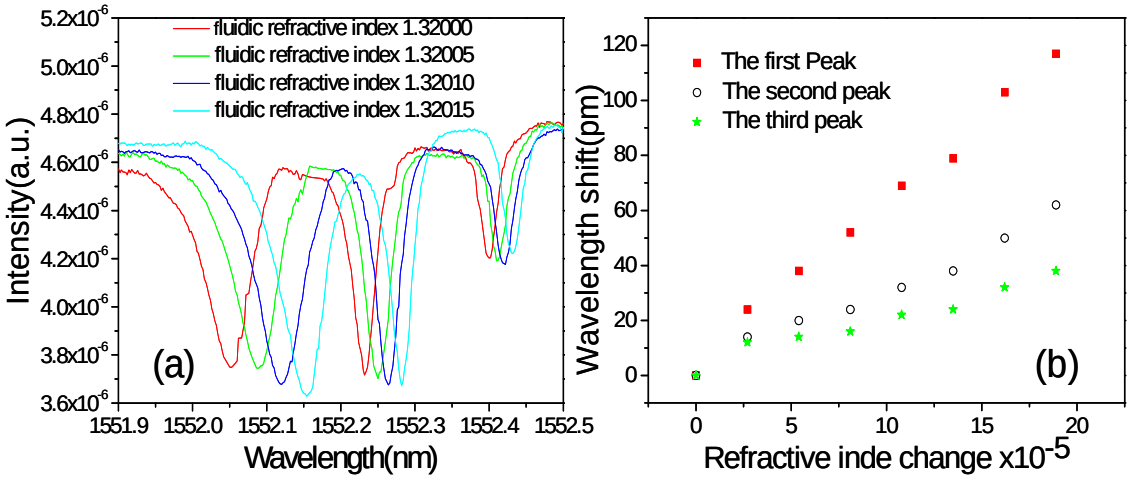

Figure 3.4 (a) Resonance curve shift due to the change of liquid refractive index in the micro-tube, (b) resonance wavelength shift as a function of the change in liquid refractive index at an incident angle of ~35 degree.

Further decreasing the incident angle to ~ 35 ^{o} allows the excitation of much higher order resonance modes in the micro-tube resonator. Figure 3.4 (a) shows four resonance spectra measured for different liquid indices at an incident angle of ~ 35^{o}. Again three resonance modes show different shifts. For the same index change of 5×10^{-5}, the resonance shifts are 30pm for the first mode, 18pm for the second and 10pm for the third. Figure 3.4(b) shows the resonant wavelength shift as a function of the refractive index change. The sensitivity for the three resonance modes are 600 nm/RIU, 360 nm/RIU, and 180 nm/RIU, respectively. The sensitivity corresponding to the first and second mode is much higher than what can be achieved with the typical evanescence wave sensors.

3.2.2 Simulations of bulk refractive index sensing

We anticipate that the very high sensitivity to the refractive index change in the silica micro-tube is due to the large optical field penetrating into the fluidic core region. In order to understand the physics behind the observed high sensitivity, we investigated the optical field distribution in the micro-tube using cylindrical coordinates z, r and ϕ. The

time independent field distribution for the resonance mode can be separated into a radial-dependent mode component and an azimuthal-dependent phase term, $\Psi_Z(r)\exp(im\phi)$, where Ψ_z is the amplitude of the axial magnetic (TE) or electrical (TM) modal field, m is the azimuthal quantization number. For the TE mode in the micro-tube we only need to consider three components: $H_{z,}$ E_r and E_ϕ. The radial dependent field H_z can be expressed by Bessel function in the following [58]:

$$H_Z = \begin{cases} AJ_m(n_1k_0r) & 0 < r \le R_1 \\ [BJ_m(n_2k_0r) + CN_m(n_2k_0r)] & R_1 < r \le R_2 \\ DH_m^{(1)}(n_3k_0r) & R_2 \le r < \infty \end{cases} \tag{3-2}$$

where $n_{1,}$ n_2 and n_3 are the refractive indices of the liquid core region, the silica micro-tube region and the outside air region, k_0 is the wave-vector in the vacuum; $J_m(nk_0r)$, $N_m(nk_0r)$ and $H_m^{(1)}(nk_0r)$ are respectively the m^{th} order cylindrical Bessel function, Neumann function and Hankel function of the first kind. By matching the boundary conditions at the liquid/silica and silica/air interfaces, we obtain the eigen function equation, which can be used to calculate the resonance wavelength. The TE mode resonance with azimuthal number *m* is determined by:

$$\frac{n_1J_m(k_0n_1R_1)}{n_2J_m'(k_0n_1R_1)} = \frac{(B/C)J_m(k_0n_2R_1)+N_m(k_0n_2R_1)}{(B/C)J_m'(k_0n_2R_1)+N_m'(k_0n_2R_1)} \tag{3-3}$$

where $\frac{B}{C} = \frac{n_3H_m^{(1)}(k_0n_3R_2)N_m'(k_0n_2R_2) - n_2H_m^{(1)'}(k_0n_3R_2)N_m(k_0n_2R_2)}{n_2H_m^{(1)'}(k_0n_3R_2)J_m(k_0n_2R_2) - n_3H_m^{(1)}(k_0n_3R_2)J_m'(k_0n_2R_2)}$

For a given m number, there are a series of k_0 satisfying equations (3), which are referred to as the ν^{th} ($n = 1, 2, 3, \ldots$) order resonance mode. The radial and tangential components of the electrical field in the TE mode can be expressed in terms of H_z as:

$$E_r = -\frac{m}{\omega \varepsilon_o \varepsilon_r r} H_z \tag{3-4}$$

and

$$E_\phi = \frac{1}{i\omega \varepsilon_o \varepsilon_r} \frac{\partial H_z}{\partial r} \tag{3-5}$$

The magnetic field distribution in the micro-tube resonator at the resonance wavelength can be obtained from Eq. (3-2) and the electrical field distribution can be obtained from equations (3-4) and (3-5). In the simulation we chose the following parameters for the micro-tube and its environment: inner radius $R_1 = 134$ μm, outer radius $R_2 = 166$ μm, and the refractive indices of the silica microtube $n_2 = 1.450$, the liquid (water) in the silica tube $n_1 = 1.320$, and the air outside the micro-tube $n_3 = 1.000$. The electrical field is responsible for the resonance wavelength shift due to the refractive index change in the liquid. Therefore, our study will mainly focus on the electrical field distribution in the micro-tube. In the micro-tube resonator the radial electrical field of TE mode is much larger than the angular electrical field, thus it will suffice to plot the radial electrical field (E_r) distribution in the silica micro-tube. Figure 3.5(a) shows the electrical field distribution of the TE_{714}^{35} mode in the silica micro-tube resonator with a resonance wavelength around 1.55 μm, where the subscript, 714, stands for azimuthal mode number and the superscript, 35, stands for radial mode number. As shown in Fig. 3.5(a), the optical field is predominantly guided in the high index region (silica tube wall) and decay

exponentially in the low refractive index regions (liquid core and air regions). Such a mode is confined in the tube wall by the total internal reflections from the silica/air and silica/water interfaces. Thus, refractive index change transduced by the TE_{714}^{35} mode is via a typical evanescence wave sensing mechanism.

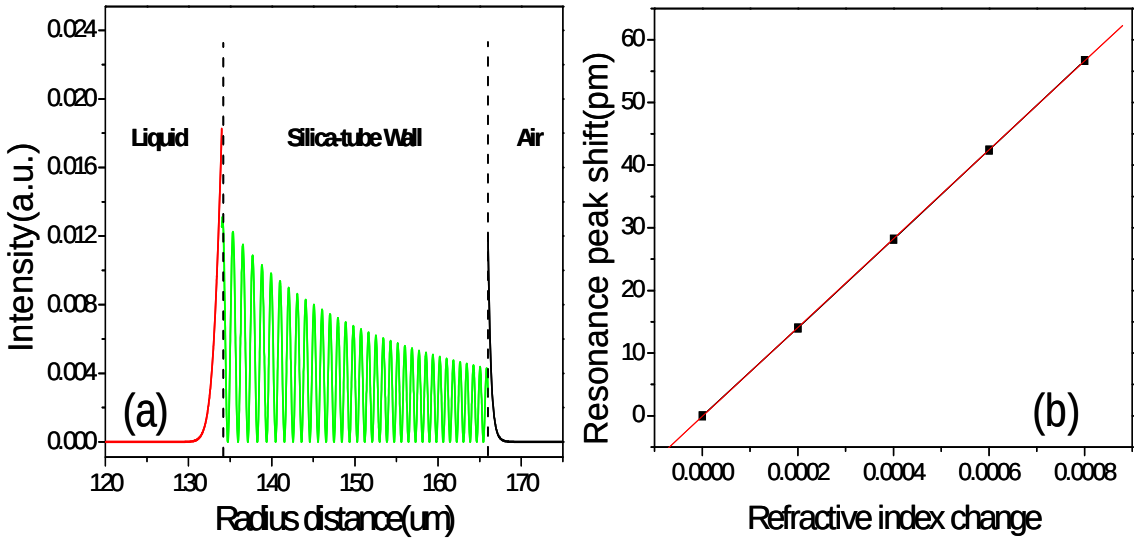

Figure 3.5 (a) Radial electrical field intensity distribution for the resonance mode. (b) Resonance wavelength shift related to liquid's refractive index change for the resonance mode

We simulated the resonance wavelength shift related to the refractive index change of liquid by using the Mie theory. In Mie theory calculation [59], the optical field outside the tube wall is replaced by:

$$H_z = H_z^{inc.} + H_z^{scat.} \tag{3-6}$$

where $H_z^{inc.} = J_m(k_0 n_3 r)$ represents the incident wave, and $H_z^{scat.} = D_1 H_m^{(1)}(k_0 n_3 r)$ represents the scattered wave. The coefficient of the scattered wave D_1 can be calculated by matching H_z and E_θ at the boundaries r = R1 and r

= R2. The resonance curve can be obtained by plotting the coefficient $\left|D_1^2\right|$ as a function of the wavelength by choosing a specific azimuthal mode number *m*. When changing the refractive index of the liquid by $2\text{x}10^{-4}$, the resonance peak gradually moves to the longer wavelength. The resonance peak shift as a function of the refractive index change is plotted in Fig. 3.5 (b). A linear fit of the calculated data points gives the sensitivity of this mode, which is ~ 70nm/RIU. This number is very close to the experimental sensitivity obtained at the incident angle of ~ 37.5 degree. Generally, for such resonance mode having an evanescence wave in the liquid core region, the sensitivity normally is lower than 100nm/RIU.

Using a similar approach, we investigated resonance modes having higher radial mode numbers. The radial electrical field distribution of the TE_{700}^{37} mode in the silica micro-tube resonator is plotted in Fig. 3.6 (a). The radial electrical field still decays exponentially in the air region, however the electrical field distribution in the liquid region is drastically different from that of the typical evanescence wave resonance mode (e.g. TE_{714}^{35} discussed above). Not only does the radial electrical field for the first peak completely move into the liquid region, but also it reaches a magnitude that is significantly higher than that in the silica tube walls. The optical field in the liquid region is no longer an evanescent field, but rather account for about 60% of the total field. Such a resonance mode with strong electrical field in the liquid region is very sensitive to the liquid's refractive index change, making it an excellent choice for index sensing. We further simulated the resonance peak shift resulting from the index change of liquid by using the Mie scattering method. The results are shown in Fig. 3.6 (b). As can be seen in

the figure, the index sensitivity of this mode is around 560nm/RIU, which is very close to the 600nm/RIU that we observed in the experiment.

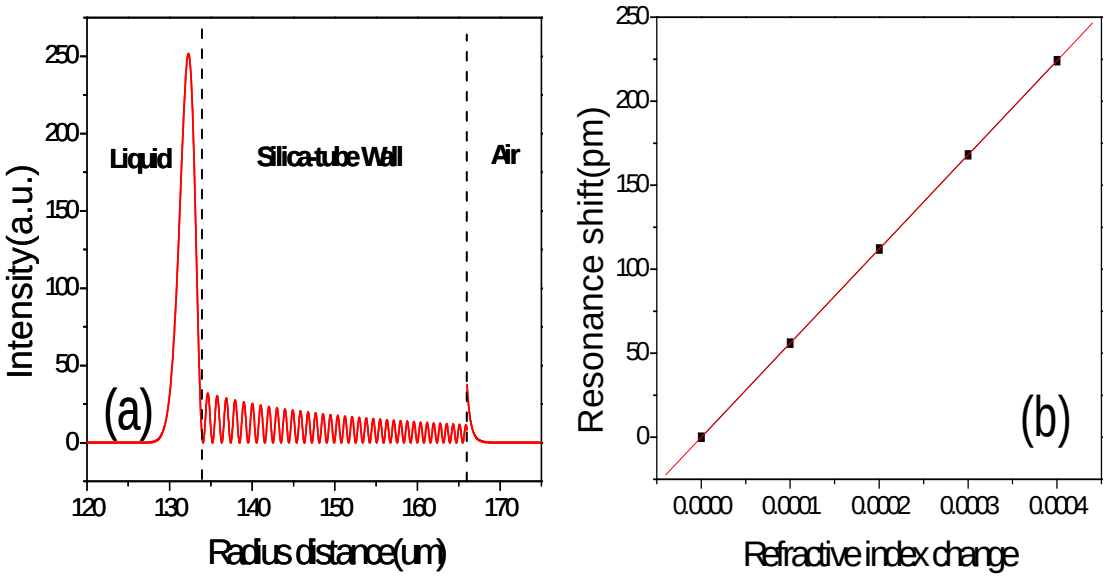

Figure 3.6 (a) Radial electrical field intensity distribution for resonance mode (b) Resonance wavelength shift related to liquid's refractive index change for resonance mode

3.2.3 Discussions

In order to understand the origin of resonance modes which have the significant field penetration into the liquid region, we presented a ray optics picture on this kind of mode. This kind of resonance modes exist as if the rays are bounced by the liquid/silica interface and confined in the liquid region. From the ray optics point of view, when the light propagating in the liquid region is incident onto the liquid/silica interface ($r = R_1$), the light will be partially reflected (termed ray 1) and partially transmitted at this inner boundary; and the transmitted rays continue to propagate within the silica tube wall until they hit the silica/air interface ($r = R_2$), where they undergo total internal reflection at this outer boundary (termed ray 2). When these two rays meet again at the liquid/silica

interface at the same location and are in phase, they will interfere constructively [60]. Furthermore, if the two rays form closed loop within the tube circumference, a resonance mode is created. The schematic ray picture of this mode is shown in Figure 3.7.

This type of modes can exist only under certain conditions related to the geometry of the micro-tube and the refractive indices of the three regions. Let us assume that the refractive index of the liquid is n_1, micro-tube n_2 and outer media n_3. We first define the incident and reflection angles at the inner boundary ($r = R_1$) as θ_1 and that at the outer boundary ($r = R_2$) as θ_2. In order to have the light transmitted through the inner boundary still well confined at the outer boundary by the total internal reflection, the angles θ_1 and θ_2 should satisfy the following three conditions:

$$\frac{\sin(\pi-\theta_1)}{R_2}=\frac{\sin\theta_2}{R_1},\ \sin\theta_1<\frac{n_1}{n_2}\ \text{ and }\ \sin\theta_2>\frac{n_3}{n_2} \tag{3-7}$$

These conditions will lead to another condition on the dimensions of the micro-tube: $\frac{R_2}{R_1}<\frac{n_1}{n_3}$. Therefore if the liquid inside the tube is water and outside media is air that corresponds to our experiment, the requirement on the ratio of the outer and inner radius of the micro-tube is $\frac{R_2}{R_1}<1.32$. This condition is satisfied for the silica micro-tube used in our experiment ($R_2/R_1 = 166/134 = 1.24 < 1.32$).

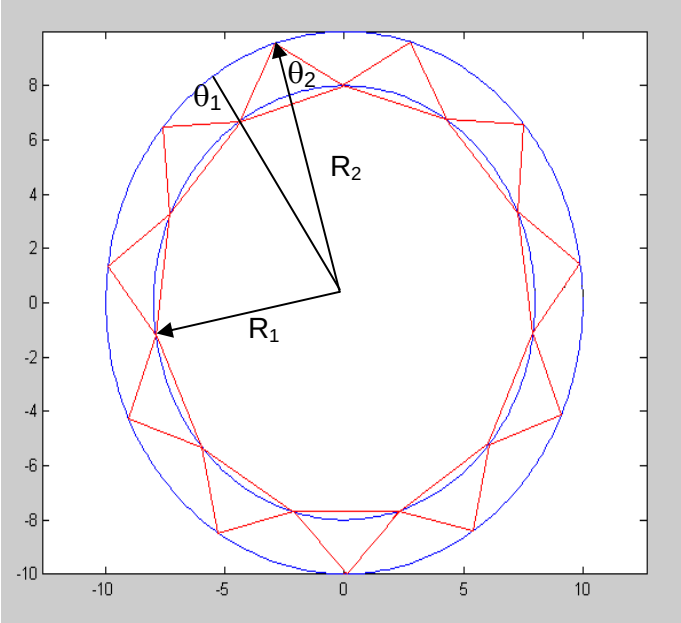

Figure 3.7 The schematic ray picture of resonance mode with light transmitted into the inner boundary.

The detection limit of the micro-resonator-based refractive index sensing device is directly related to the Q factor of the resonator and the sensitivity of the resonance mode discussed above. In our experiment we can resolve the one twenty-fifth of the resonance line width change, given that resonance mode with the high field inside the liquid region has a Q factor of ~ $2x10^4$. The limit of the smallest detectable liquid index change is ~ 5 x 10^{-6} (refractive index units). The Q factor of the micro-tube is determined by the total loss of resonance mode in the resonator, which includes the radiation loss, the absorption loss and the scattering loss. Thus, the resonator's overall Q factor can be expressed as:

$$\frac{1}{Q} = \frac{1}{Q_{radiation}} + \frac{1}{Q_{absorption}} + \frac{1}{Q_{scattering}} \qquad (3\text{-}8)$$

Because the micro-tube forms a curved waveguide, even for the special mode described above that has high field intensity in the liquid region, the optical wave transmitted into the liquid region still can return to the same loop and well confined by the total internal

reflection at outer boundary; thus, the radiation loss in this kind of resonance mode is still very low. The scattering loss also can be reduced by choosing the mode with low field intensity at the inner boundary interface. The Mie scattering method revealed that the intrinsic Q value of this kind of mode is around 10^7 without considering the water absorptions loss. When the loss due to high water absorption around 1.55 μm wavelength is taken into account in the Mie Scattering calculation, the Q factor is reduced to about 5 x 10^4, which is consistent with experimental result of Q ~ 2 x 10^4. Therefore we believe that the water absorption loss limited Q is the dominant term in determining the overall Q factor of the resonance mode. Based on these considerations, we can infer that the refractive index detection limit of the micro-tube resonator sensor can be greatly increased by moving the working wavelength from near the IR to the visible range. Using the Mie theory calculation we predict the intrinsic Q of the resonance mode with high field inside the liquid region is above 5x10^6 in the visible range. If in experiment we can achieve a Q factor in visible range around 10^6, the smallest detection limit can reach ~ 5 x 10^{-8} (refractive index units), resulting in the micro-tube resonator being one of the best index sensing devices.

3.3 Surface sensing experiment

3.3.1 Resonant mode characterizations

Before we start to do the surface sensing experiment, we need pick up a resonance mode which will be highly sensitive to the bio-film absorbed to the inner surface of the micro-tube. To test the sensitivity of the resonance mode in micro-tubes, an index sensing experiment is first performed by changing the refractive index of the liquid that flows

through the micro-tube, and simultaneously monitoring the corresponding resonance wavelength shifts. The refractive indices of the liquid were controlled by premixing a very small amount of isopropyl alcohol (IPA) with deionized (DI) water. The refractive index of the solution can be estimated based on the dielectric constants of both liquids and the molar ratio of each component: Figure.3.8 shows two resonance spectra measured from the reflected beam for liquids with two different refractive indices filled in the micro-tube. In the index sensing experiment, one liquid is the DI water and another is DI water mixed with IPA with volume ratio 1:0.02. The refractive index difference between each spectrum was ~ $2x10^{-4}$, and the incident angle to the prism was ~ 36^{o}. One resonant mode is monitored in each spectrum and the resonance wavelength shift is around 38pm for index change 2 x 10^{-4}. The sensitivity is estimated by $\Delta\lambda/\Delta n$=190nm/RIU.

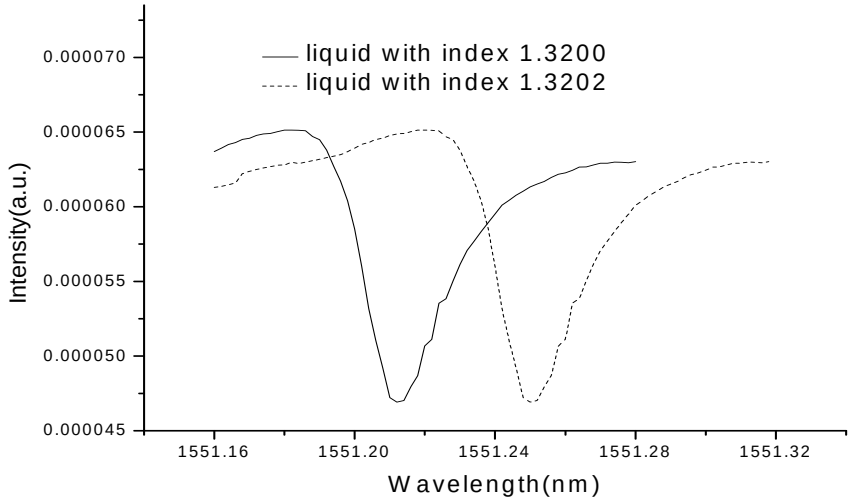

Figure 3.8 Resonance cure shift due to change of liquid index in the micro-tube

Figure 3.9 shows the electrical field distribution of TE_{707}^{36} mode in the silica micro-tube resonator where the azimuthal mode number is 707, and the radial mode number is 36. As shown in Figure 3.9, the optical field is predominantly guided in the

high index region (silica tube wall) and decay exponentially in the low refractive index regions (liquid core and air regions). Unlike the special mode we exploited for bulk refractive index sensing that has main optical field residing in the liquid core region, in the experiment on detecting lipid membrane binding on the tube wall, we prefer the resonance mode represented in Fig 3.9 since it offers a very large electrical field right at the inner surface of the tube wall, allowing maximum interaction with the thin lipid membrane layer. Such a mode is confined in the tube wall by the total internal reflections from the silica/air and silica/water interfaces.

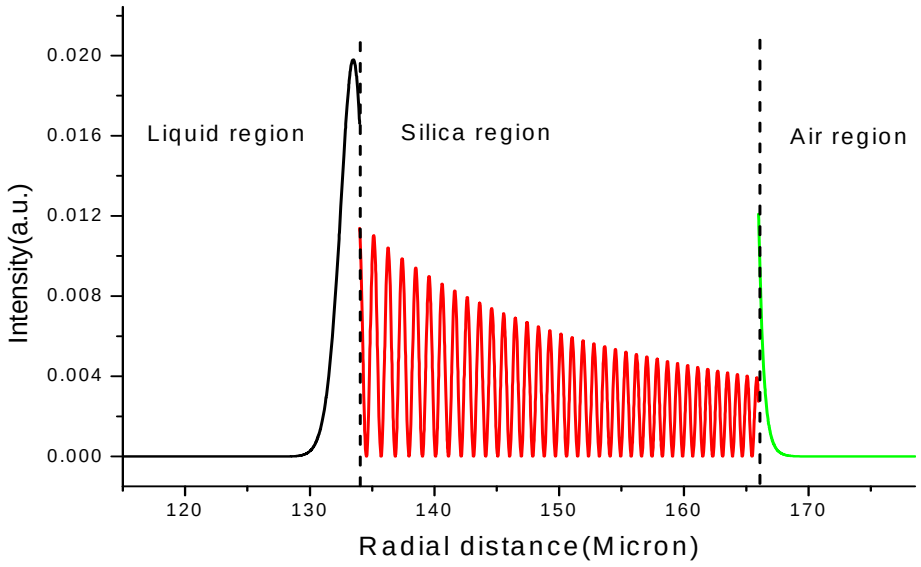

Figure 3.9 Radial electrical field intensity distributions for the resonance mode $E_{r\,707}^{36}$

3.3.2 Lipid monolayer detection

The micro-tube resonator sensor system is used to perform first surface sensing experiment by detecting the formation of a lipid monolayer on the inner wall of the micro-tube. It starts with a piranha solution (H_2SO_4:H_2O_2=2:1) cleaned micro-tube treated with a silane to render its inner surface to hydrophobic. After surface treatment,

the micro-tube is filled with DI water and the resonant curve is recorded as a baseline, then 1-palmitoyl-2-oleoyl-sn-glycero-3-phosphocholine (POPC) liposome is injected into the micro-tube. It is known that POPC lipid will form a monolayer to such a surface by orienting their hydrophobic tails toward the hydrophobic wall [61]. The POPC liposome is staying in the micro-tube for 30mins to make sure that it forms a good monolayer coverage on the inner wall of the micro-tube, after that we wash those unbounded liposome out with DI water. All the spectra are recorded in the figure 3.10. The resonance net shift in this case is ~22pm, which is the contribution from the monolayer coating on the inner wall of the micro-tube.

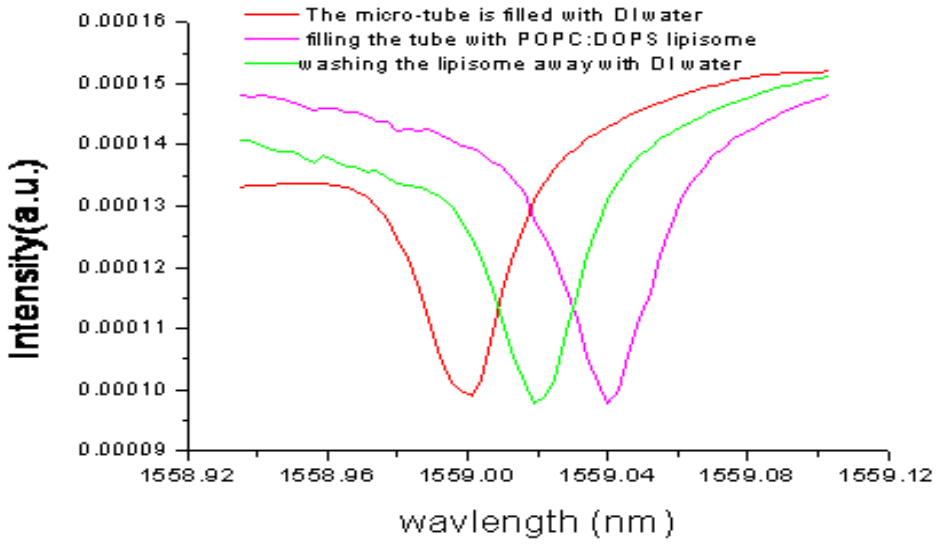

Figure 3.10 Resonance curve shift due to the lipid monolayer binding to the inner wall of micro-tube.

3.3.3 Lipid bi-layer detection

The second experiment to characterize our micro-tube resonator sensor system is to detect the lipid bi-layer absorbed on to the inner wall of the micro-tube by using the

resonant mode with similar sensitivity in our pervious experiment. The resonant spectra of the process are shown in the figure 3.11. First the piranha cleaned micro-tube is filled with the buffer solution Tris as to establish the baseline, then the POPC liposome is injected into the silica micro-tube, after 30 minutes the resonant spectrum was measured and showed a red shift of ~74 pm. This shift is due to the lipid membrane binding to the inner surface of the micro-tube and the unbound liposome remained in the solution. After that the Tris buffer is used to wash away the unbound liposome in the micro-tube and replace it with Tris buffer and the resonant curve is shown a back shift around 30pm. The net shift is about 44pm which represents the lipid membrane absorbed onto the inner surface of the micro-tube. The resonant wavelength shift from the lipid bi-layer is almost double of the shift from the lipid monolayer, which is quite reasonable.

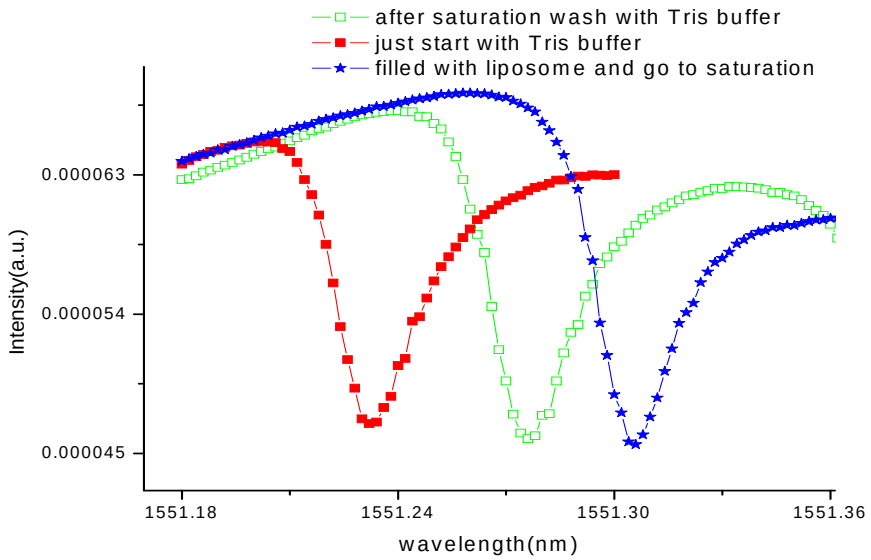

Figure 3.11 resonance curve shift due to lipid membrane binding to inner surface of micro-tube

3.3.3 Self assemble layer by layer detection

To further investigate the capability and the repeatability of the micro-tube resonator sensor system in detecting the adsorption of an ultrathin film, we performed another experiment by investigating a layer-by-layer polymer film formation on the inner wall of silica micro-tube. This experiment is done by using the electrostatic self-assembly of nanometer thick polyelectrolyte films. Electrostatic self-assembly relies on the electrostatic interactions between an adjacent polycation and polyanion layers. The substrate is preprocessed to have charges (e.g., the oxide surface has a negative charge in dilute acid solution). In our experiment, we used poly-diallyldimethylammonium chloride (PDDA) as the polycation and polydye s-119 as the polyanion. To start, the micro-tube is cleaned with piranha solution for 30 minutes, which helps to form $-O^-H^+$ groups on tube surface where H^+ ions can be readily exchanged with other cations. Then cationic solution PDDA solution is flow through the tube to allow the negatively charged silica wall surface to be completely covered with a layer of positively charged PDDA molecules. After a DI water rinse, ionic solution poly dye S-119 flows through the tube and form a negatively charged monolayer that bond to the pervious cationic layer by electrostatic interaction [62]. This sequence can be repeated to form a multi-layer coating at the inner tube wall. The experiment results of coating 7 alternating mono-layers are shown in Fig. 3.12. The resonance shift induced by PDDA monolayer is ~ 9pm, while that of poly dye s-119 monolayer is ~ 24pm. This reason for this difference is that the refractive index and thickness of poly dye s-119 monolayer is much larger and thicker than that of PDDA.

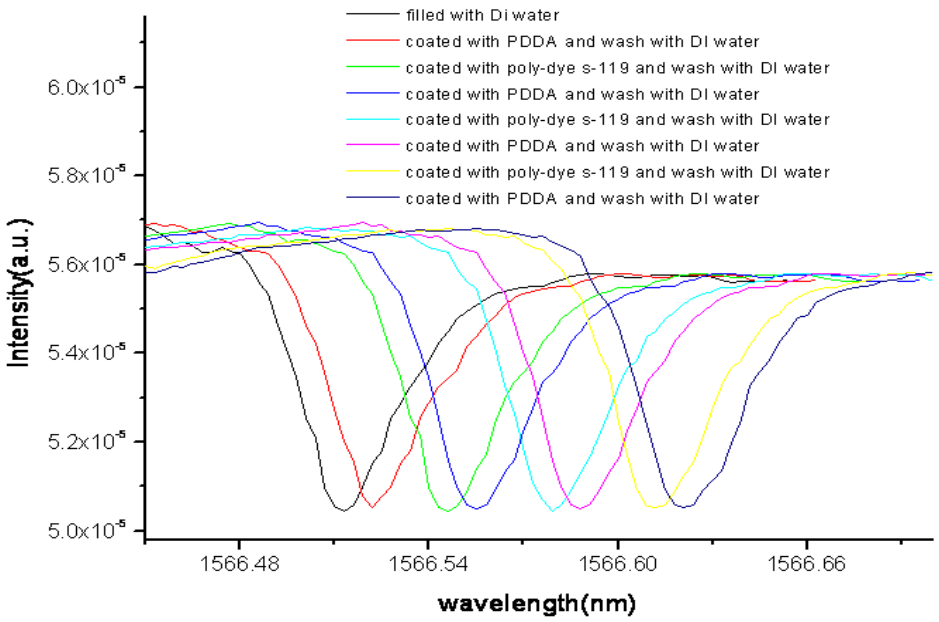

Figure 3.12 Resonance curve shift due to the electrostatic self –assembly thin film coating at the inner wall of the silica micro-tube.

3.3.4 Quantification of bio-film layer binding

We simulated the resonance wavelength shift related to the refractive index change of liquid and due to the adsorption of an organic layer on the inner tube wall by using the Mie theory. By changing the refractive index of the liquid with $1x10^{-4}$, the resonance peak gradually moves to longer wavelength. By fitting the calculated data points, we can get this mode's sensitivity for refractive index as ~ 170nm/RIU. This number is very close to the experimental sensitivity obtained at index sensing experiment which is around.190nm/RIU, which also supports our interpretation of the optical field distribution for such a resonance mode

Using the Mie scattering method, we investigate the resonance wavelength shift due to the lipid membrane absorbed onto the inner wall of the micro-tube. We keep the

micro-tube's geometry the same like before and we consider the lipid bilayer's refractive index around 1.46. When the inner surface of the tube is coated with lipid membrane, for TE mode the magnetic field distribution can be described in the following form:

$$H_z = \begin{cases} B_1 J_m(k_0 n_1 \rho) & 0 \le \rho < d_1 \\ [B_2 J_m(k_0 n_2 \rho) + B_3 N_m(k_0 n_2 \rho)] & d_1 \le \rho < d_2 \\ [B_4 J_m(k_0 n_3 \rho) + B_5 N_m(k_0 n_3 \rho)] & d_2 \le \rho < d_3 \\ B_6 H_m^{(1)}(k_0 n_4 \rho) & d_3 \le \rho < +\infty \end{cases} \quad (3\text{-}9)$$

where n_1, n_2 , n_3 and n_4 are the refractive indices of the liquid core region, lipid membrane region, the silica micro-tube region and the outside air region. After matching the boundary conditions, the resonance condition can be given by the following equation:

$$\frac{(B_2/B_3)J_m(k_0 n_2 d_2) + N_m(k_0 n_2 d_2)}{(B_2/B_3)n_2^{-1}J'_m(k_0 n_2 d_2) + n_2^{-1}N'_m(k_0 n_2 d_2)} = \frac{(B_4/B_5)J_m(k_0 n_3 d_2) + N_m(k_0 n_3 d_2)}{(B_4/B_5)n_3^{-1}J'_m(k_0 n_3 d_2) + n_3^{-1}N'_m(k_0 n_3 d_2)} \quad (3\text{-}10)$$

Where

$$\frac{B_2}{B_3} = \frac{n_2 J'_m(k_0 n_1 d_1) N_m(k_0 n_2 d_1) - n_1 J_m(k_0 n_1 d_1) N'_m(k_0 n_2 d_1)}{n_1 J_m(k_0 n_1 d_1) J'_m(k_0 n_2 d_1) - n_2 J'_m(k_0 n_1 d_1) J_m(k_0 n_2 d_1)}$$

and $$\frac{B_4}{B_5} = \frac{n_3 H_m^{(1)'}(k_0 n_4 d_3) N_m(k_0 n_3 d_3) - n_4 H_m^{(1)}(k_0 n_4 d_3) N'_m(k_0 n_3 d_3)}{n_4 H_m^{(1)}(k_0 n_4 d_3) J'_m(k_0 n_3 d_3) - n_3 H_m^{(1)'}(k_0 n_4 d_3) J_m(k_0 n_3 d_3)}$$

Figure 3.13 shows the resonance curves shift to longer wavelength when the thickness of the thin film layer absorbed on the micro-tube is increased incrementally by 1nm. This is because the resonance mode's effective refractive index in the cavity is increased with the increase in adsorbed layer thickness. Then the calculated resonance wavelength shift is plotted with respect to the change of the thickness of the lipid membrane, we find that the experimentally observed 44pm shift corresponds to a thickness of the lipid membrane

thickness around 4-5nm with the typical lipid membrane with the refractive index around 1.46. This result is consistent with a bilayer lipid membrane thickness reported in the literature.

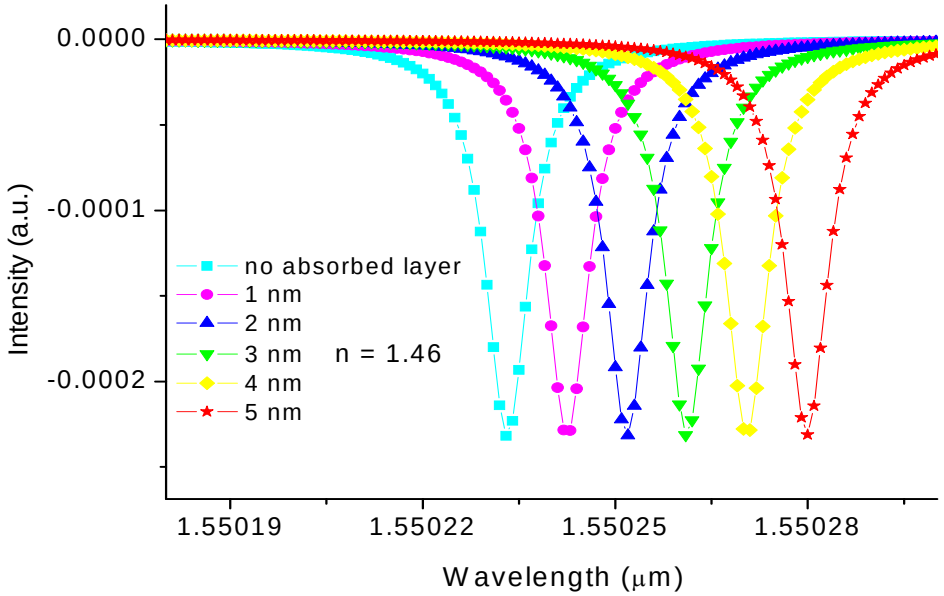

Figure 3.13 Simulated resonance curve shift with the lipid membrane thickness change

The simulation from the layer by layer coating also shows that the PDDA with the refractive index around 1.46 and poly dye s-119's refractive index around 1.6, and both of the monolayer's thickness is around 1nm, which is consistent to the reported by other paper.

3.3.5 Study interaction between the lipid membrane and proteins

First we have studied the interaction between the lipid bilayers and Annexin V proteins: Annexin V is a member of a large family of proteins, annexins, which bind to negatively-charged lipids in a Ca^{2+}-dependent manner [63]. This protein is known to disrupt the blood coagulation by forming 2-dimensional crystals on the surface of cell membranes. Figure 3.14 shows the experimental results of annexin V interacted with POPC lipid bi-layer. The solid line curve corresponds to the baseline as the micro-tube

filled with 8mM $Cacl_2$ buffer solution; the dash line curve (a net shift of 4pm) is a result of continuous flow of the annexin V protein solution with concentration 26.67ng/ml for 10minutes followed by washing with 8mM $Cacl_2$ solution; and the dash dot line curve (a net shift of 8pm) was obtained after continuous flow of the annexin V protein solution for 40 minutes followed by 8mM $Cacl_2$ washing. The resonance shift is relatively small as compared with the shift we observed in the lipid bilyer experiment. We believe this is because the Annexin V protein does not have full coverage when it binds to the surface of the lipid membrane [64].

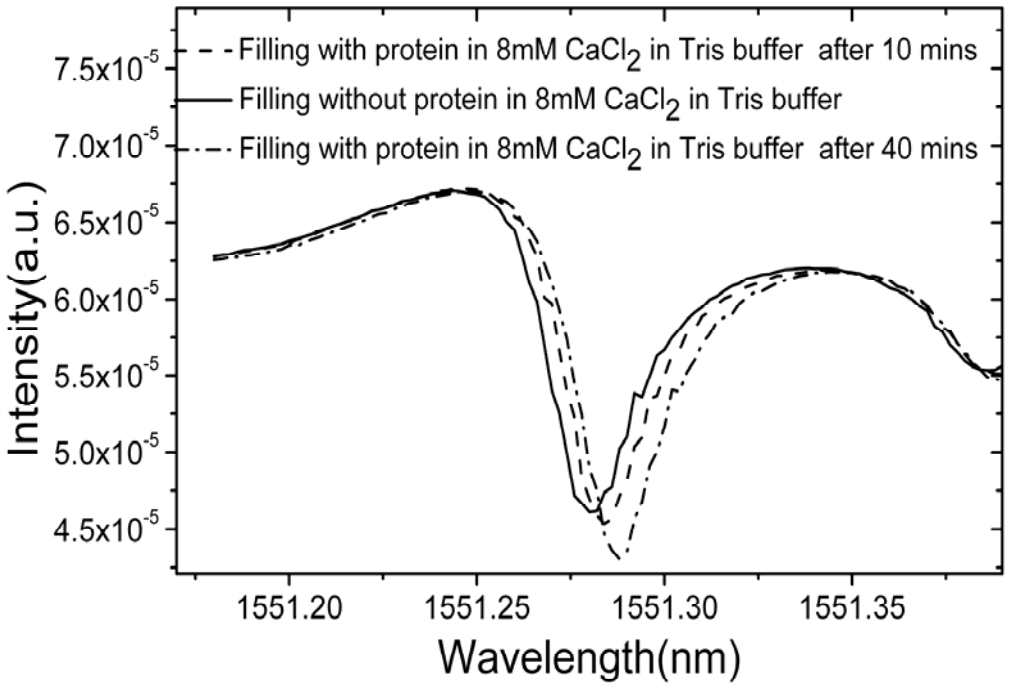

Figure 3.14 Resonance curve shift due to Annexin V binding to POPC lipid bi-layer

Second we have studied the interaction between the lipid bilayers and Alamethicin proteins: Alamethicin is a 20-amino-acid peptide from the fungus *Trichoderma viride* and it is well know that alamethicin acts by creating pores in the cell membrane to form the

ion channel in the lipid membrane [65]. The first experiment we have done is to show the resonant curve shift with time at fixed alamethicin concentration. First we take the signal from the silica micro-tube filling with DI water as a baseline, then the micro-tube is filled with POPC liposome for 15 mins to make sure that the lipid bi-layer membrane is well formed on the inner wall of the micro-tube, after that the un-bounded POPC liposome is washed out with the DI water for 5 mins, we can clearly observe the resonant wavelength red shift due to the POPC lipid membrane binding to the inner wall of the micro-tube. Then the antibiotic peptide alamethicin with concentration 500mg/ml is injected into the micro-tube and we collect the optical signal at different times after the injection. We can find that with the time increased the resonant wavelength shift to short wavelength. In the first 10mins the shift is large, after that the shift is getting smaller and smaller, which is because the concentration of the alamethicin get reduced after it stay in the silica micro-tube for some time. After 40 mins the resonance blue shifting is getting saturated and the total shift is about 9pm (in Figure 3.15). This blue shift which can be explained that the refractive index of the whole film absorbed on the inner wall is decreased or the film thickness of the lipid membrane is reduced.

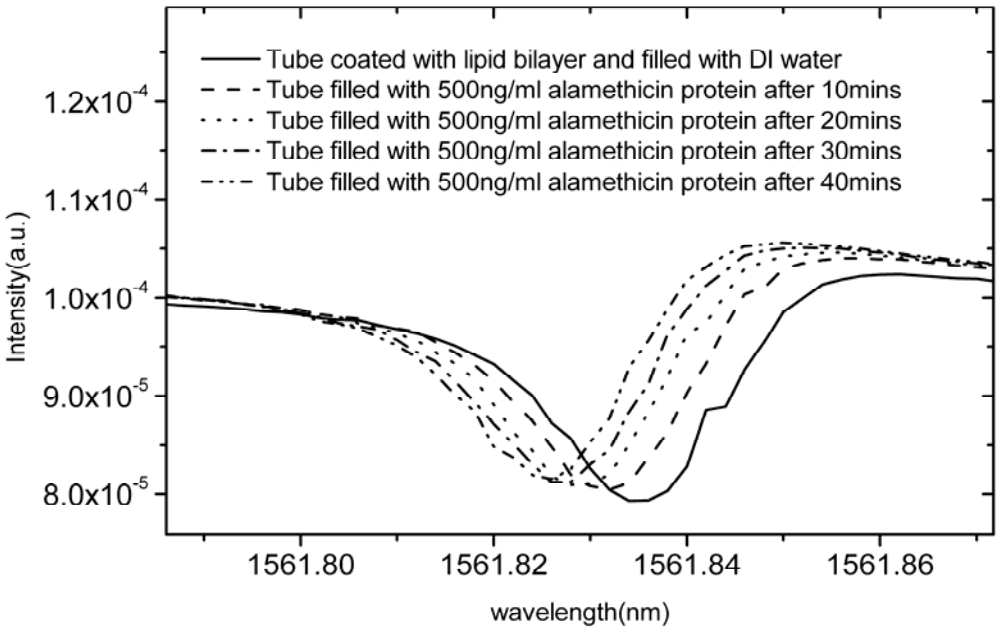

Figure 3.15 Resonance curve shift due to the antibiotic peptide alamethicin interact with lipid bilayer on the inner surface of the micro-tube

Another experiment we have done is that we start with lower concentration of alamethicin and we gradually increase the alamethicin concentration from 5ng/ml to 10ng/ml, 50ng/ml, 100ng/ml, 200ng/ml and 500ng/ml, then we monitored the resonance wavelength shift after the micro-tube is filled by with difference alamethicin concentration solutions for 30mins. At this experiment we also choose the resonance mode which has the high electrical field at the inner boundary by testing its bulk index sensitivity (which is around 200nm/RIU) and the Q factor of this resonance mode is around $3.6x10^4$. We can clearly see from the figure 3.16 that when the alamethicin concentration changes from 5ng/ml to 100ng/ml, the resonance wavelength is continuously shifting to the longer wavelength and the shift is quiet linear. From 200ng/ml to 500ng/ml the resonance wavelength is shifting to shirt wavelength and the shift is quiet dramatically. Those can be explained that at low concentration (lower than

100ng/ml) the alamethicin is just binding to the surface to the lipid membrane which will increase the thickness of the film, so the resonance wavelength will shift to longer wavelength. But at the high concentration (higher than 100ng/ml) , alamethicin will aggregated together to form a pore on the lipid membrane and those holes can be filled by lower index media water, so the total effective index of the film will reduced and which will contribute to the blue shift of the resonance wavelength. If we compare those two experiment results, it is interesting to find that when the alamethicin concentration is change from low to high the total shift almost be zero, but with high concentration we can see that the shift is negative, which means that those alamethicins which is binding to the surface of lipid membrane at lower concentration still will stay on the lipid membrane and which will not have the contribution to form pores in the lipid membrane. And those binding on the surface alamethicin will not effect those one who inserted into the lipid membrane to form pores, so the total blue shift to with this two case are all around 10pm.

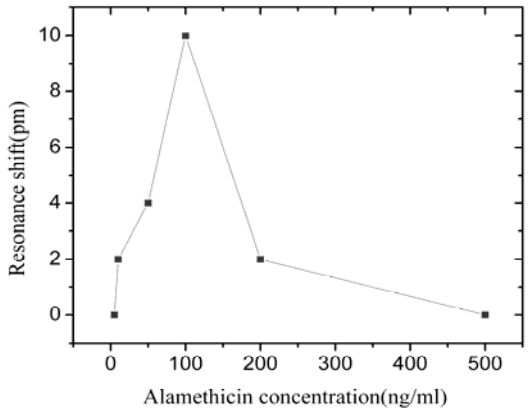

Figure 3.16 Resonance wavelength shift related to different concentration of alamethicin injection.

3.4 Conclusion

We have successfully demonstrated using prism coupled micro-tubes as new bio-chemical sensing platform. In bulk refractive index sensing experiments, we have observed a unique resonance mode with very high sensitivity around 600nm/RIU which is very good for bulk index sensing application. In surface sensing experiments, we have successfully demonstrated to detect lipid mono-layer, lipid bi-layer and electrostatic self assemble layer by layer binding to inner surface of silica micro-tubes and the simulation results match well with those experiments results. Furthermore, the interactions between the lipid bi-layer to some proteins have been studied in our sensor system.

Chapter 4

Sensing properties of micro-tube resonator sensors

4.1 Introduction and motivation

In the silica microtube resonator sensor system we observed two kinds of sensing regimes in our previous experimental studies. The first is the typical evanescent sensing regime in which the optical wave is confined between the inner and outer boundaries of the microtube wall by total internal reflections; only the evanescent wave extending into the microtube liquid core will interact with the liquid or gas to realize the sensing function. The second is a nonevanescent sensing regime in which the optical field is confined by total internal reflection at the outer boundary, but the optical wave is partially transmitted and partially reflected at the inner boundary. The constructive interference between the two waves establishes a much stronger optical field inside the microtube, which also penetrates deeper into the liquid core region and greatly enhances the sensitivity due to the significantly improved field overlap with the analytes in the liquid.

The purpose of this chapter is to provide detailed theoretic alanalysis of the two sensing modes and investigate their advantages and limitations. In this chapter, we first plotted the field distribution of the corresponding WGMs with different radial orders.

Based on the field distribution, the microtube's various sensing properties were investigated in detail by the perturbation method for both evanescent and nonevanescent regimes, which include bulk refractive index, surface, and absorption sensing properties. Also we proposed an ultra-high sensitivity sensor by using a coupled cavity platform..

4.2 Field distribution in micro-tube resonator

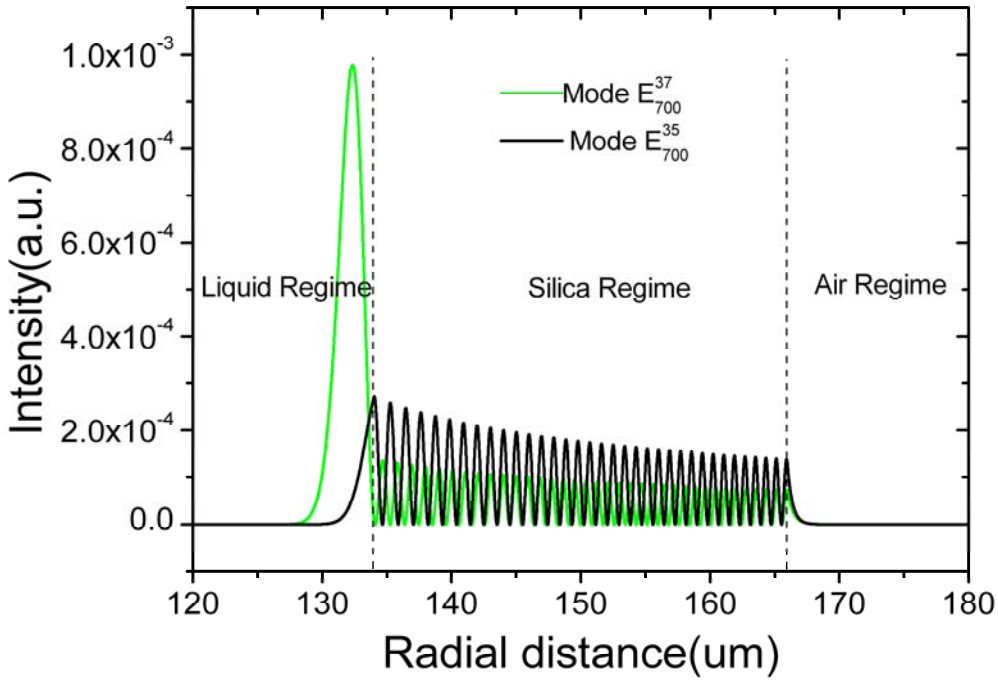

Figure 4.1 The normalized electric field intensity distributions with azimuthal number *M*=700 and radial order number *N*=35 and 37 (denoted by E_{700}^{35} and E_{700}^{37}, respectively)

The normalized electric field intensity distributions (from the equation in chapter 3) with azimuthal number *M*=700 and radial order number *N*=35 and 37 (denoted by E_{700}^{35} and E_{700}^{37}, respectively) are shown in Fig. 4.1. In the simulation we chose the same

microtube dimensions reported in our previous experiment: inner radius R_1=134 μm, outer radius R_2=166 μm, liquid refractive index n_1=1.32, silica refractive index n_2=1.45, and air refractive index n_3=1.00. We can clearly see that with the increase of the radial order number the optical field is penetrated deeper into the liquid region. We found that when the radial order number is equal to or smaller than 35 the first peak of the electric field intensity (counting from the center of the tube) and the rest of the electric field intensity peaks remain in the high index region (silica region). This means that the optical field is well guided within the silica wall and the wave is confined by the total internal reflections at both the inner and outer wall boundaries with only a small evanescent field penetrating into the liquid region. Such modes will be referred to as evanescent sensing modes for sensing applications. However, if the radial number is larger than 35 (e.g., mode E_{700}^{37}), the first peak of the electric field moves completely into the liquid region because the optical wave is partially transmitted and partially reflected at

4.3 Bulk refractive index sensing sensitivity

After the electrical filed intensity distribution in the micro-tube resonators are obtained, the sensitivity of the different resonance modes can be calculated by the perturbation theory. The bulk refractive index sensitivity (S), defined as the ratio of the resonance wavelength shift to the bulk index change, can be described by the following equation [66]:

$$S_{bulk} = \frac{\delta\lambda}{\delta n} = \lambda \frac{\int_{V_1} |E_z|^2 n d\vec{r}}{\int_V n^2 |E_z|^2 d\vec{r}} \tag{4-1}$$

where λ is the resonance wavelength, V is the whole space and V_1 is the space from the origin to the inner boundary.

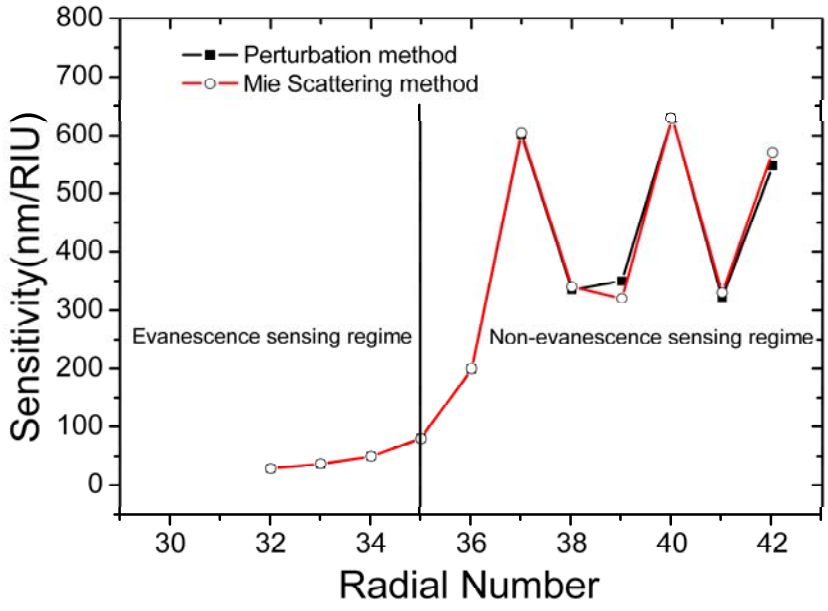

Figure 4.2 Simulated bulk refractive index sensing sensitivity of different radial order modes with the same azimuthal number M=700 by perturbation method and Mie scattering method

Using the electric field distributions obtained for resonance modes of the different radial number (N) but the same azimuthal number M=700, the bulk refractive index sensitivity can be calculated using Eq. (4-1) and plotted in Fig. 4.2. The result from the perturbation method (black curve in Figure 4.2) matches well with that from Mie scattering method (red curve) which is very accurate to predict the resonance wavelength in the micro-cavity. Clearly the bulk refractive index sensing sensitivity increases

dramatically as the radial number increases from N=32 to N=37. This is because with higher radial order number the optical field penetrates deeper into the liquid region. As stated earlier, when the radial number (N) is smaller than 35, the optical wave is still well confined by the total internal reflection at the inner boundary and only weak evanescent field resides in the liquid region and we call this regime (with $N < 35$) as evanescence sensing regime. When the radial number (N) is larger than 35, the first E-field peak of the resonance modes moves into the liquid region and we call the regime with $N > 35$ as non-evanescence sensing regime. For bulk refractive index sensing the non-evanescence regime is preferred due to increased field overlap with the liquid analyte. The sensitivity can be enhanced by a factor of 6 if we compare the maxima sensitivity in the non-evanescence regime (e.g. N=37) to that in the evanescence regime (e.g. N=35).

An interesting finding from this calculation is that the sensitivity in the non-evanescence region (for N>37) oscillates between 300nm/RIU to 600nm/RIU with the increase in the radial order number. Therefore it is important to choose the proper resonance order when performing the bulk index sensing experiment. This can be done, e.g. by tuning the incident angle, in the experimental setting. The oscillatory behavior is somewhat contradictory to our expectation that as the radial order increases the optical field penetrates deeper into the fluid regime and the sensitivity would continue to increase rather than oscillates. We believe this behavior is due to an intricate interference effect between the two optical rays.

4.4 Surface sensing sensitivity

In a typical surface sensing experiment, the bio-molecules adsorbed onto the surface of the inner wall of a micro-tube will cause a resonance shift, and one can define the surface sensing sensitivity as the ratio of the resonance wavelength shift to the thickness of the biomolecular film. Addition of the biomolecular film to the inner surface of the tube will change the wave-vector of a supported mode from k_0 to k_1 and the electrical field from E_0 to E_1. Both the unperturbed (E_0) and perturbed (E_1) electrical fields satisfy the wave equation:

$$\nabla \times \nabla \times E_0 = k_0^2 \varepsilon E_0 \tag{4-2}$$

$$\nabla \times \nabla \times E_1 = k_1^2 \varepsilon_1 E_1 \tag{4-3}$$

where ε and ε_1 are the dielectric constant distributions of the micro-tube system before and after the bio-molecular adsorption. Multiplying Eq. 4-3 by E_0^* and integrating over the entire space gives:

$$\int_{v} E_0^* \cdot \nabla \times \nabla \times E_1 d\vec{r} = k_1^2 \int_{v} E_0^* \cdot \varepsilon E_1 d\vec{r} + k_1^2 \int_{v_1} E_0^* \cdot (\varepsilon_{film} - \varepsilon_{liquid}) E_1 d\vec{r} \tag{4-4}$$

where ε_{film} and ε_{liquid}, are the dielectric constants of the bio-molecular film and the liquid, respectively; ν is the total space of the micro-tube and ν_1 is the space occupied by the adsorbed bio-film on the micro-tube. By using an equality [67]:

$$\int_v E_0^* \cdot \nabla \times \nabla \times E_1 d\vec{r} = \int_v E_1 \cdot \nabla \times \nabla \times E_0^* d\vec{r} = k_0^2 \int_v E_1 \cdot \varepsilon E_0^* d\vec{r}$$

the following equation can be derived:

$$(k_0^2 - k_1^2) \int_v E_1 \cdot \varepsilon E_0^* d\vec{r} = k_1^2 \int_{v_1} E_0^* \cdot (\varepsilon_{film} - \varepsilon_{liquid}) E_1 d\vec{r} \tag{4-5}$$

Assuming that the adsorbed bio-molecular layer thickness T is very thin, the electric field within the film can be taken to be a constant, and the overall change of the field distribution in the resonator is very small, so E_1 can be approximated by E_0 in the perturbation calculation. We can then obtain the following result:

$$\frac{\delta\lambda}{\lambda} = \frac{\int_{v_1} E_0^* \cdot (\varepsilon_{film} - \varepsilon_{liquid}) E_1 d\vec{r}}{2\int_v E_1 \cdot \varepsilon E_0^* d\vec{r}} \approx \frac{\left|E_{R_1}\right|^2 (\varepsilon_{film} - \varepsilon_{liquid}) \pi R_1 T}{\int_v E_0 \cdot \varepsilon E_0^* d\vec{r}} \tag{4-6}$$

and the sensitivity in surface sensing can be then expressed as:

$$S_{surface} = \frac{\delta\lambda}{T} = \lambda \frac{\left|E_{R_1}\right|^2 (\varepsilon_{film} - \varepsilon_{liquid}) \pi R_1}{\int_v E_0 \cdot \varepsilon E_0^* d\vec{r}} \tag{4-7}$$

From Eq. 4-7, we can see that the sensitivity can be enhanced by increasing the ratio of the field intensity at the tube inner boundary to the total optical field, reducing the tube thickness, or enlarging the inner radius of the micro-tube. The first condition can be achieved by exciting higher order evanescent modes. Reducing the tube thickness also

decreases the optical field inside the tube wall, which has a similar effect to the first condition. Increasing the inner radius R_1 creates the evanescence field at the inner surface [68], which leads to improved sensitivity. Calculated surface sensing sensitivity by perturbation method for different radial mode numbers with the same azimuthal number M=700 matches well with the results from the Mie scattering method and the results are plotted in Figure 4.3. In the evanescent sensing regime, the sensitivity increases with radial number because of the increase of the electrical field at the inner boundary. In the non-evanescent sensing regime, the oscillatory behavior as a function of the mode numbers has been again observed but with opposite trend to the case of bulk index sensing sensitivity.

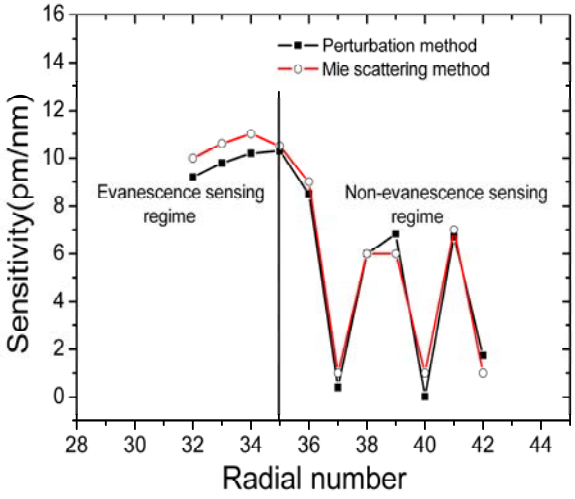

Figure 4.3 Simulated surface sensing sensitivity of different radial order modes with the same azimuthal number M=700 by perturbation method and Mie scattering method. The bio-film's refractive index is assumed to be 1.46

4.5 Absorption sensing sensitivity

Detection of the presence of certain analytes in the fluid can also be accomplished if the analytes exhibit absorption in the wavelength range of interest. The sensitivity can be enhanced by using the micro-resonator structure due to the increased interaction length between the light propagating in the resonator and the analytes. For simplicity, we consider the case of analytes dissolved in the bulk liquid flowing through the micro-tube. Light absorption can be included in our model by taking into account the imaginary part of the refractive indices. The presence of the light absorbing analytes changes the imaginary part of refractive index of the liquid from κ_1 to κ_2, which will cause the imaginary part of the resonance wave vector change from k_1 to k_2 and the electrical field of the resonance mode changes from E_1 to E_2. The unperturbed and the perturbed electrical field still satisfy the wave vector equation:

$$\nabla \times \nabla \times E_1 = (k_0 - ik_1)^2 \varepsilon_1 E_1 \tag{4-8}$$

$$\nabla \times \nabla \times E_2 = (k_0 - ik_2)^2 \varepsilon_2 E_2 \tag{4-9}$$

where the ε_1 and ε_2 are the dielectric constant distributions for micro-tube filled with liquid with optical absorption coefficient κ_1 and κ_2, respectively. In the liquid region the dielectric constants are $\varepsilon_1 = n_0^2 - \kappa_1^2 + 2in_0\kappa_1$ and $\varepsilon_2 = n_0^2 - \kappa_2^2 + 2in_0\kappa_2$. In real sensing experiment κ_1 and κ_2 are much smaller than n_0, so the resonance wavelength and the field distribution will mostly remain unchanged. Only the resonance mode's Q factor will

change with the optical absorption coefficient. From the equations (4-8) and (4-9), we can give another new equation:

$$(k_0 - ik_1)^2 \int \varepsilon_1 E_1 \cdot E_1^* d\vec{r} = (k_0 - ik_2)^2 \int \varepsilon_2 E_2 \cdot E_2^* d\vec{r} \tag{4-10}$$

By comparing the real and the imagery part of equation (4-10) and we assume the Q factor of the micro-tube resonator is predominantly determined by the absorption loss, we can find two equations:

$$\frac{k_2 - k_1}{k_0} = \frac{n_0 \int_{v_1} E_1 \cdot E_1^* d\vec{r}}{\int_v \varepsilon E_1 \cdot E_1^* d\vec{r}} (\kappa_2 - \kappa_1) \tag{4-11}$$

$$k_1 \kappa_2 = k_2 \kappa_1 \tag{4-12}$$

The quality factor of the micro-tube resonator can be defined as flowing: $Q_i = \frac{k_0}{2k_i}$, where i=1,2., We define an interaction factor of the resonance mode $\Gamma = \frac{2n_0 \int_{v_1} E_1 \cdot E_1^* d\vec{r}}{\int_v \varepsilon E_1 \cdot E_1^* d\vec{r}}$, then we can get:

$$Q = \frac{1}{\kappa \Gamma} = \frac{4\pi}{\lambda \alpha \Gamma} \tag{4-13}$$

We define the sensitivity of the absorption sensing as the ratio of the Q factor change with the change of the imaginary part of the refractive index of the liquid change:

$$S_{abs} = \left|\frac{\delta Q}{\delta \alpha}\right| = \frac{4\pi}{\lambda \alpha^2 \Gamma} = \frac{Q}{\alpha} \tag{4-14}$$

It is interesting to show that the absorption sensitivity is increased with Γ decreased, which also means that the sensitivity is increased with increasing Q factor, consistent to one's expectation.

The simulated absorption sensing sensitivity with different radial number (same azimuthal number M=700) of the resonance modes with absorption coefficient α=0.327cm^{-1} is shown in the figure 4.4. The black curve is simulated by perturbation method and the red curve is simulated by Mie scattering method. We can clearly see that the sensitivity (for radial number N<36) linearly decreases with the increasing radial number. This is because modes with higher radial mode number have more overlap with the absorbing media and therefore lower Q factor. The perturbation method again matches very well with Mie scattering method when N is smaller than 38, after that the Mie scattering shows smaller sensitivity comparing with the perturbation method. We think this is because that at large radial number the Q factor is not only dominated by the absorption loss, but also the radiation loss due to bending also becomes important.

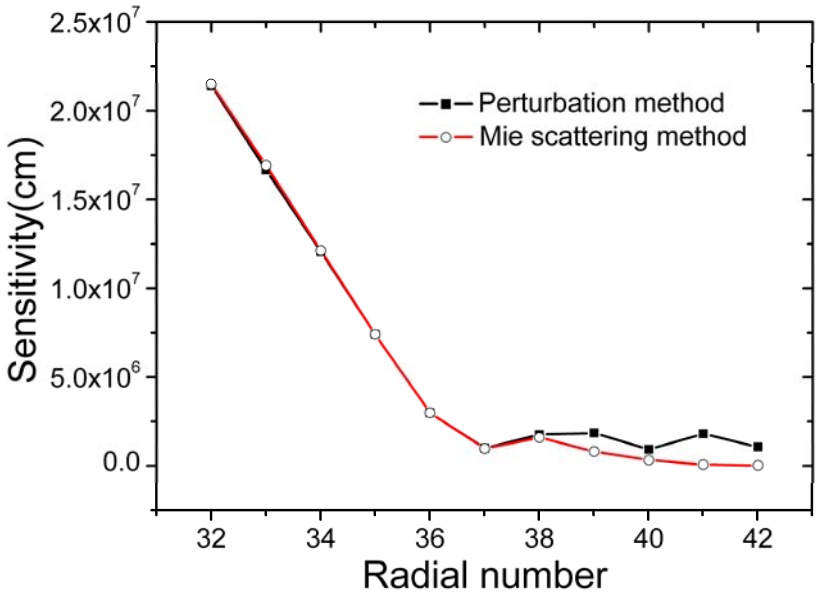

Figure 4.4 Simulated absorption sensing sensitivity of different radial order modes with same azimuthal number M=700 by perturbation method and Mie scattering method. The absorption coefficient of liquid is assumed to be α=0.327cm^{-1}

4.6 Sensitivity enhancement using a coupled cavity

As we can find from section 4.3 that the micro-tube resonator sensor's sensitivity can not be further improved by using much higher order mode. And the sensitivity starts to oscillate between 300nm/RIU and 600nm/RIU between different higher-order-modes. Can we still further improve the device's sensitivity? Couple of methods have been proposed and realized in cavity based microcavity sensor system: Professor Arnold's group has realized an idea to improve the device's sensitivity by coating the surface of the resonator with a relatively high refractive index nano-layer. The high refractive index layer tends to draw light in and pulls the energy from the sphere interior and brings it closer to the surface. As a result, the evanescent field of the coated microsphere would extend deeper into the outside medium containing the molecules to be detected. They

experimentally reported the sensitivity enhancement around 7 times, and theoretically the sensitivity can be enhanced up to 50 times [69]. M. Sumetsky [70], et al reported to using a curable low index polymer to fix the position between the capillary tube and the coupling fiber after it solidified. Meanwhile, the capillary tube's wall can be thinned down to few hundred nanometers to push more optical field into the liquid region to realize much higher sensitivity. The sensitivity has been demonstrated as high as 800nm/RIU in the bulk refractive index sensing experiment. But there still has significant part of the optical field in the outside polymer region, so the sensitivity can not be further improved up to 1000nm/RIU. In here, we proposed a new kind of resonance mode as a sensing mode in low index material inner coated micro-tube resonator sensors. Such a kind of resonant mode can have an extremely high optical field in the liquid region, which could lead to extremely high optical sensitivity up to 1000nm/RIU.

The proposed inner-coated silica micro-tube resonator sensor is shown in the Figure 4.5(a), where R_1 and R_3 are the inner and outer inner radii of the silica micro-tube and R_2-R_1 is the thickness of the inner coated low refractive index layer. And we treat it as four-layer system in cylindrical coordinate in which the first layer is liquid core with refractive index n_1 (1.32, water), the second layer is coated low refractive index layer with refractive index n_2 (1.275, Teflon AF 2400), the third layer is silica tube layer with refractive index n_3 (1.45, Silica) and the fourth layer is the air with refractive index n_4 (1, air). The radial field distribution in the cavity can be described in the following:

$$E_m(r) = \begin{cases} B_1 J_m(k_0 n_1 r) & 0 \le r < R_1 \\ [B_2 J_m(k_0 n_2 r) + B_3 N_m(k_0 n_2 r)] & R_1 \le r < R_2 \\ [B_4 J_m(k_0 n_3 r) + B_5 N_m(k_0 n_3 r)] & R_2 \le r < R_3 \\ B_6 H_m^{(1)}(k_0 n_4 r) & R_3 \le r < +\infty \end{cases} \quad (4\text{-}15)$$

Where J_m , N_m and $H_m^{(1)}$ are the m th Bessel function, Neumann function and Hankel function of the first kind, respectively.

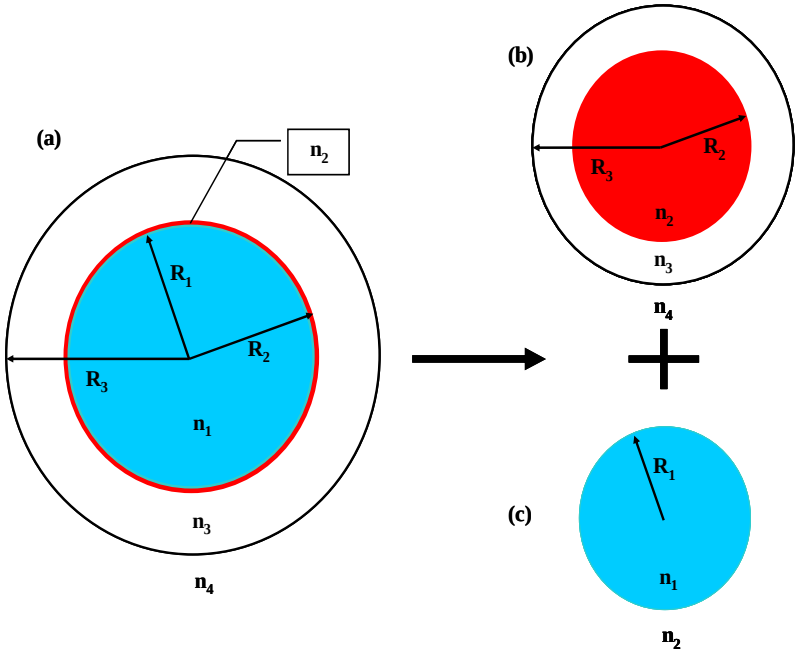

Figure 4.5 (a) a schematic of inner coated silica micro-tube sensor, the cavity can be decomposed into two cavities: (b) a silica micro-tube cavity filled with low index materials and (c) a water cylinder cavity covered with low index materials

Such a cavity also can be decomposed into two individual cavities which are shown in the Fig. 4.5(b) which is a silica micro-tube filled with low index material and Fig. 4.5(c) which is a liquid micro-cylinder with a low refractive index media outside. When we put those two resonator cavity together, those two sets of resonance in those two cavities can be coupled to each other and understood in terms of 2x2 Hamiltonian matrix [71]:

$$H = \begin{pmatrix} E_1 & V \\ W & E_2 \end{pmatrix}$$

Where E_1 and E_2 are the complex energies of the uncoupled system, W and V are the coupling constants between two different states. For weak

coupling $2\sqrt{VW} < \left|\mathrm{Im}(E_2) - \mathrm{Im}(E_1)\right|$, there is a crossing for the real part of the energy and anti-crossing of the imaginary part. For a strong coupling condition, $2\sqrt{VW} > \left|\mathrm{Im}(E_2) - \mathrm{Im}(E_1)\right|$ and there is an anti-crossing of the real part of the energy and a crossing of the imaginary part.

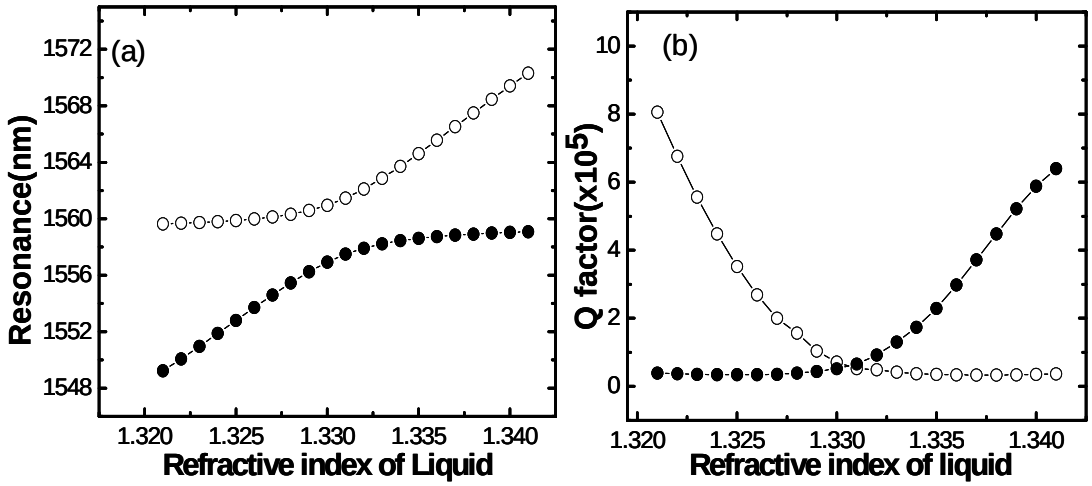

Figure 4.6(a) Anti-crossing behavior of the resonant wavelengths when the refractive index of liquid is around 1.331, (b) the Quality factor shows crossing behavior when the refractive index of liquid is around 1.331

Figure 4.6 (a) shows a pair of coupled mode's resonance wavelength changes with the refractive index of the liquid core. A clear anti-crossing [72, 73, 74] behavior was shown in the figure 4.6(a), where two resonance wavelengths come close but then repel each other at liquid refractive index around 1.331, and resonance Q factor presents a crossing in figure 4.6(b) at the same liquid refractive index position. These phenomena indicate that those two modes are strong coupled. No Q factor enhancement was observed around anti-crossing region, this mainly is due to the Q factor in the cavity is dominated by water absorption loss.

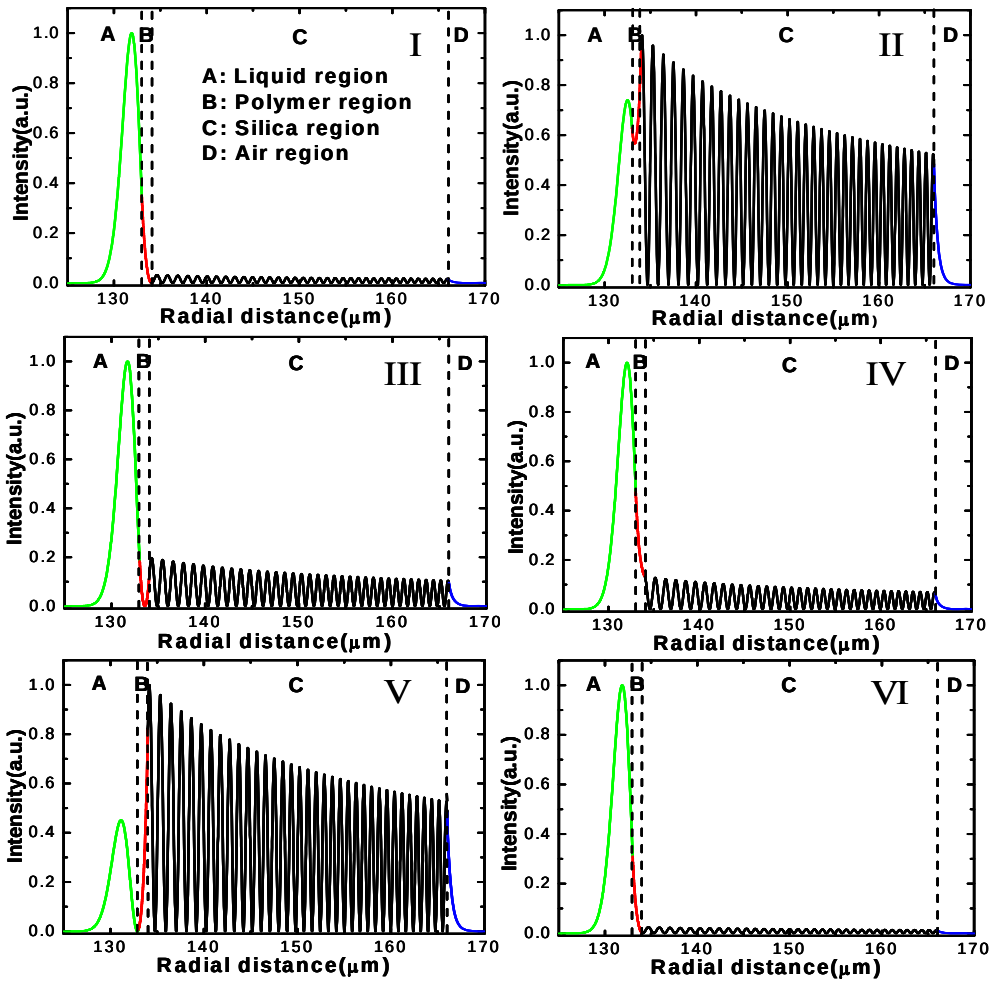

Figure 4.7 Calculated field distributions in the cavity with difference refractive index of liquid, (I,II) liquid refractive index around 1.325, (III,IV) liquid refractive index around 1.331, (V, VI) liquid refractive index around 1.338.

The device's strong coupling phenomena have been studied by plotting the device's spatial field distribution with different refractive index of the liquid core. Figure 4.7 shows the calculated field distributions in the cavity with difference refractive index of liquid: (I,II) belong to the pair of resonance mode with liquid refractive index =1.325, (III,IV) belong to the pair of resonance mode with liquid refractive index =1.331, (V, VI) belong to the pair of resonance mode with liquid refractive index = 1.338. Figure 4.7 (I, III, V) belong to the lower branch of the resonance mode in figure 4.6(a) and Figure4.7

(II, IV, VI) belong to the up branch of the resonance mode in figure 4.6(a). We can clearly see that the mode in I (or VI) is mainly a liquid-like mode almost all the optical field is confined in the liquid region, only very small part of the field is in the silica tube region and the mode in II (or V) is mainly a silica tube mode, most of the field is confined in the silica region and only part is in the liquid region. Mode III and IV are the hybridized mode, which are the super-positions of the mode I (or VI) and II (or V) far away from the anti-crossing region. When we sweep the liquid refractive index cross the anti-crossing the region, we can see that the liquid mode start to change from one branch to another branch. This is a clear evidence of the strong coupling that the resonance mode exchanges their mode pattern as well as the energy while passing through the anti-crossing [75] region.

The device's refractive index sensing sensitivities have been obtained by taking the differential of the curves in the figure 4.6 (a) and the sensitivities of those paired modes changing with refractive index of liquid core have been shown in the figure 4.8(a). The coupling nature makes those two modes' sensing sensitivity to have an opposite trend to the changing of the refractive index of liquid. And the sensitivity can achieve as high as 967nm/RIU. Figure 4.8(b) shows that the device's sensitivity can be increased above 1000nm/RIU by reducing the inner coated material's refractive index which is mainly due to change the coupling strength between those two cavity modes.

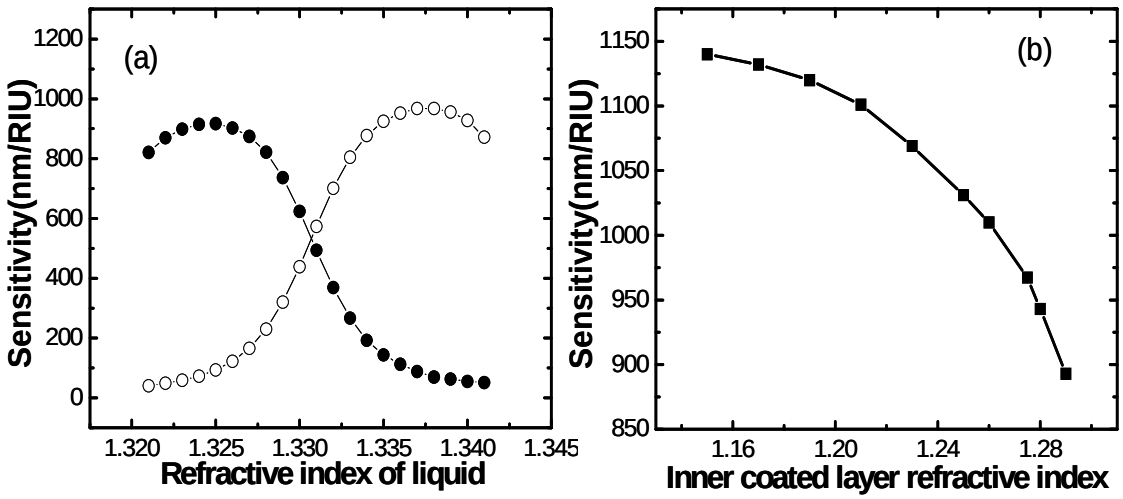

Figure 4.8 (a) sensitivity of two hybrid resonance mode changes with liquid refractive index.(b) the sensitivity changes with the inner coated layer material refractive index.(with fixed thickness d=1μm)

4.7 Conclusion

We provide a theoretical study on various sensing properties on silica micro-tube resonator sensors. We found that the bulk refractive index sensing sensitivity increases with the radial order number in the evanescent sensing regime and oscillates in the non-evanescent sensing regime. The non-evanescent mode is particularly suitable for bulk refractive index sensing and the sensitivity can achieve 600nm/RIU in our structure. The evanescent mode, having a high electric field magnitude at the inner boundary, is preferred in the surface sensing experiment with sensitivity as high as 10pm/nm and high *Q* resonance mode is desirable for absorption-based sensing. Coupled cavity platform was proposed to realize ultra-high (>1000nm/RIU) sensitivity sensing.

Chapter 5

High sensitive ultrasonic detection using polymer microrings

5.1 Introduction and motivation

In ultrasound (pulse-echo) imaging and photoacoustic (also called optoacoustic) imaging, high resolution is achieved using high-frequency ultrasound transducers. High-frequency (above 20 MHz) ultrasound imaging has been applied to intravascular imaging, endosonography, small animal imaging, skin imaging and ophthalmology, and biomedical applications of high-frequency photoacoustic imaging include microvasculature visualization, functional imaging, and intravascular imaging. In these referenced works, piezoelectric transducers were used. Small element size and spacing and large element count greatly limit the feasibility of realizing high-frequency two-dimensional (2D) arrays based on piezoelectric transducers. However, to achieve high frame rate in three-dimensional (3D) ultrasound and photoacoustic imaging, 2D arrays are required. One way to avoid the difficulties inherently associated with piezoelectric transducers is to detect and generate ultrasound optically. Optical detection of ultrasound has been studied for decades. Its advantages include immunity against electromagnetic interference at optical ends, easier realization of large and dense arrays

with element sizes of 10–100 μm, high acoustic bandwidth, and dependency of signal-to-noise ratio (SNR) on optical probing power instead of detector size.

Recently, an optical cavity based ultrasound detection platform has attracted increasing attentions. Compared with conventional piezoelectric transducers, the new detection platform provides several advantages, such as preserving high sensitivity with reduced element sizes, high-frequency and wideband response with simple fabrication. In this new optical cavity based detection platform, optically transparent polymer material was used because of its high optical elastic coefficient and high deformability, which can provide sensitive response under acoustic pressure. High Q resonators using the TIR mechanism include micro-spheres, micro-disks, micro-rings and micro-tubes. By combining polymer material's high optical elastic coefficient and high deformability with the TIR-based high Q factor micro-resonators, it is possible to achieve high sensitivity acoustic detector by using polymer micro-resonator.

5.2 Fabrication process of polymer microrings

5.2.1 Normal mold fabrication process

Previous our group has demonstrated to use Nano-imprinting technique to fabricate polymer micro-ring resonator [76]. The fabrication process starts with creating a master mold. First, e-beam lithography is used to create micro-ring coupled with straight waveguide patterns in the PMMA layer and then the patterns are transferred to the SiO_2 layer by using reactive ion etch (RIE). After RIE, the PMMA residual layer is removed by hot acetone. This master mold is called "shallow mold". Then the shallow mold is treated with surfactant to reduce the surface energy. Then the shallow mold is used to

fabricate a deep mold which is used to directly fabricate the polymer micro-ring by nano-imprinting technique. The shallow mold is used to create patterns in a layer of 15K PMMA on the silicon substrate with 2μm thermal oxide using imprinting technique. After that the residual layer is etched away by O_2 plasma. Then a lift-off process is performed to transfer the patterns to the metal film (Ni or Cr). With this metal as an etch mask, we can etch deep and vertical patterns by using RIE. After RIE, the metal mask is removed by metal etchant. The whole fabrication process is shown in the Figure 5.1 [77]

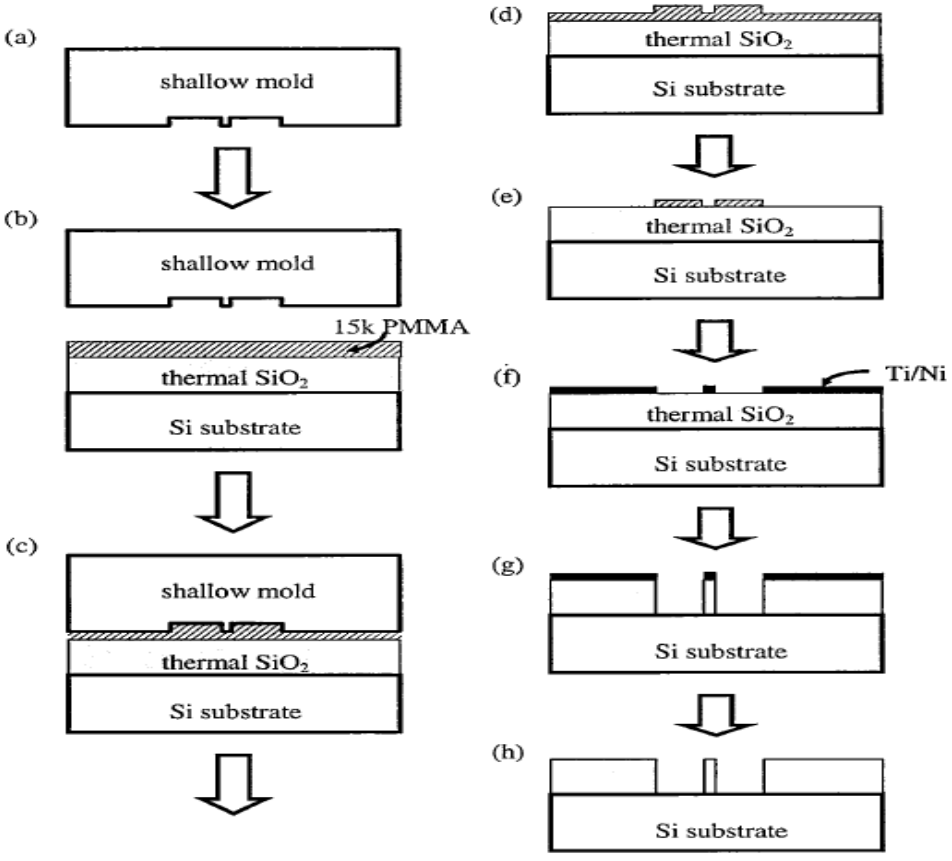

Figure 5.1 Schematic of fabrication of deep mold from the shallow mold. (a) A shallow mold fabricated from EBL and RIE. (b) The shallow mold is contacted onto the sample with 15K PMMA layer. (c) The imprinting process is performed at high pressure and high temperature. (d) The sample is separated from the mold and the PMMA patterns are created on the substrate. (e) PMMA residual layer is etched away by O_2 plasma. (f) Metal

mask Ti/Ni is deposited and lift-off process is performed to transfer the pattern to metal film. (g) The oxide layer is etched using metal mask. (h) The metal layer is removed by the metal etchant.

5.2.2 Simplified mold fabrication process

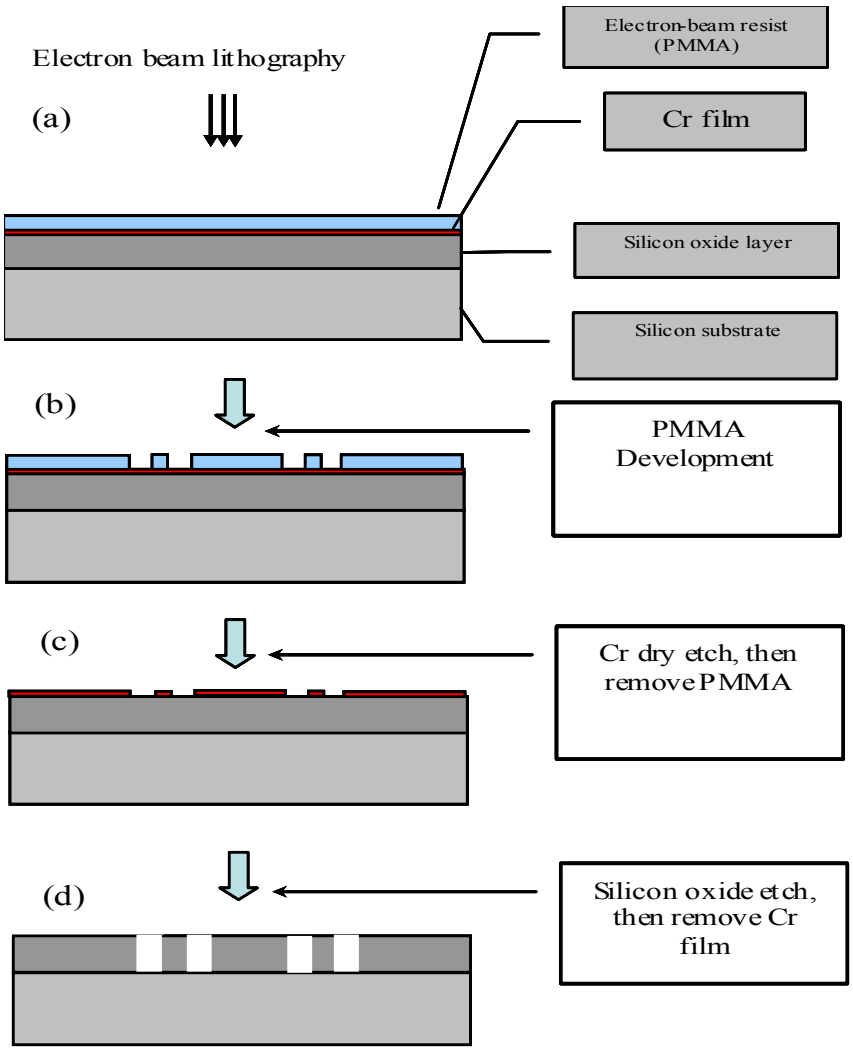

Figure 5.2 schematic of simplified silicon oxide mold fabrication process. (a) E-beam lithography on the 950k PMM layer on the silicon substrate with 2μm silicon oxide and 50nm Cr film. (b) The sample is developed in MIBK:IPA=1:3. (c) The Cr layer is etched by using PMMA as an etching mask, then the PMMA layer is removed by hot acetone. (d) The silicon oxide layer is etched using Cr as an etching mask, then remove the Cr layer by using Cr etchant.

Our previous fabrication process need fabricate a shallow mold first and then create the deep mold using the shallow mold. There are four etching steps in the whole mold

fabrication process, which could increase the surface roughness with too much etching steps. In order to simplify the fabricate process and well control the surface roughness, we developed a new fabrication process start with e-beam lithography on 150nm thick 950k PMMA A4 on silicon substrate with 50nm Cr layer on 2μm thermal oxide, after that the exposed sample is developed in development with MIBK:IPA=1:3 for 1min. and rise in IPA for another 1 min. Then the Cr layer is etched away with Cl_2 gas by using the PMMA layer as an etch mask, after that the PMMA layer is removed in hot acetone. The next step is to etching the silicon oxide layer by using Cr as an etch mask and then the Cr layer is removed by using Cr etchant. The whole process flow is showing on the figure 5.2.

After the deep mold fabrication, the polymer micro-ring coupled with straight waveguide patterns is created using nano-imprinting lithography and then followed by O_2 plasma to remove the residual layer.

5.2 Spectrum and SEM characterization

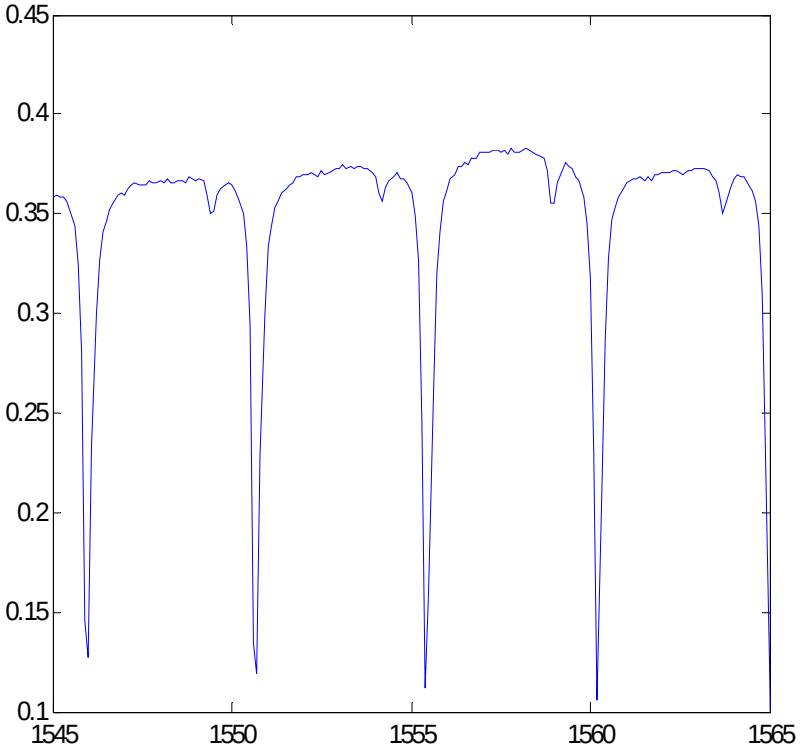

Figure 5.3 Transmission spectrum of the polymer microring

The fabricated polymer microrings were characterized by using a tunable laser at 1.55μm wavelength range. The measured transmission spectrum of polymer microring is shown in the Figure 5.3 and the Q factor of the resonance peak is around 6000. The SEM image of the polymer micrirng is showing in the Figure 5.4(a), and the sidewall view of the polymer microring is showing in Figure 4.4(b). We can clearly see the roughness on the sidewall which is created during the reactive ion etching process. Figure 5.4 (c) shows some holes on the top part of the polymer microring. This may be generated during the RIE process, some of the metal particles are re-deposited in the trench and then those

particles can act as a mask to form some pillars in the trench. This problem can be solved by replacing the metal mask with resist mask.

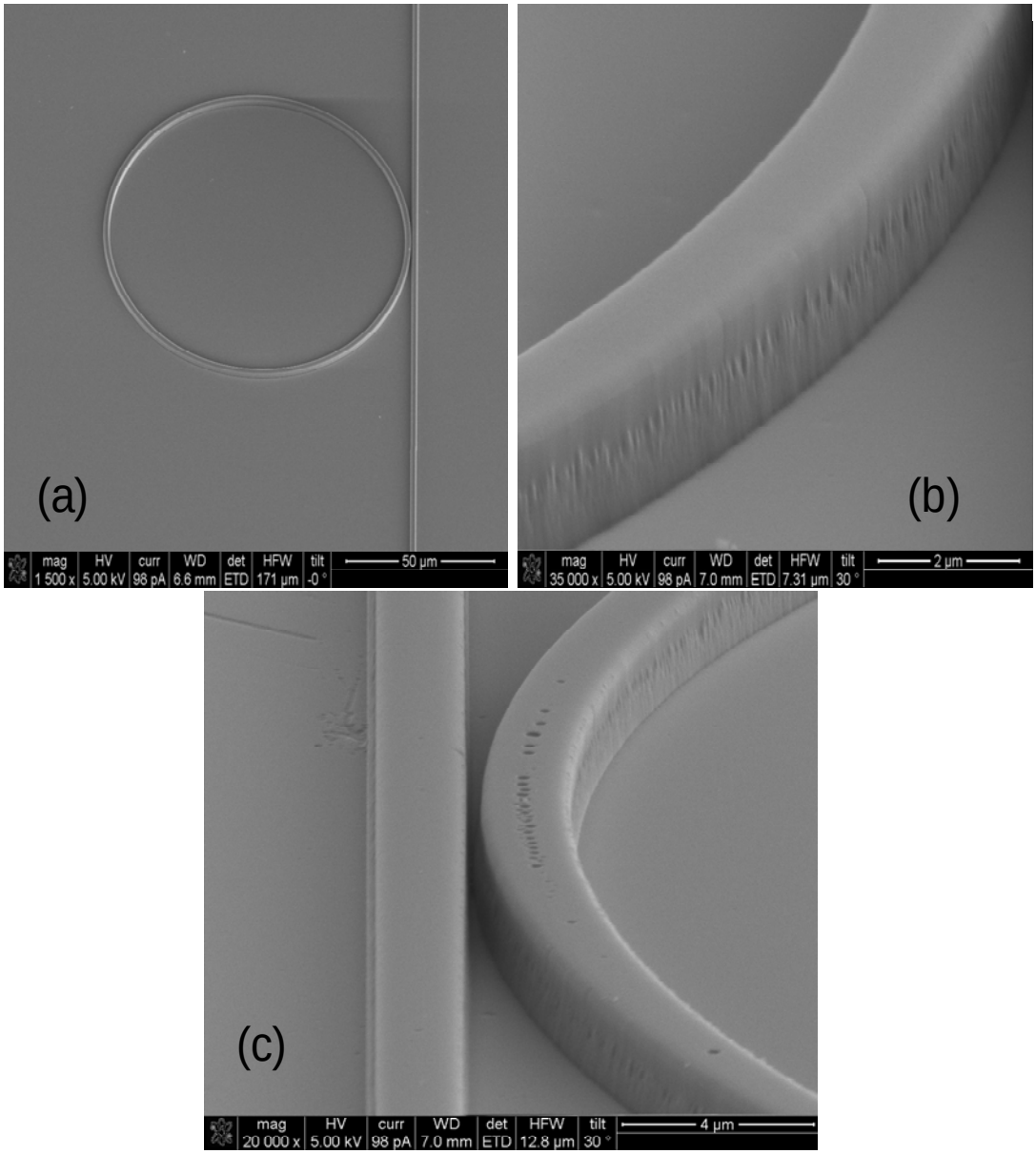

Figure 5.4 (a) SEM image of the polymer micro-ring with R=50µm, (b) the sidewall view of the polymer microring (c) SEM image of the polymer micro-ring with some holes on the top

5.3 Acoustic sensitivity

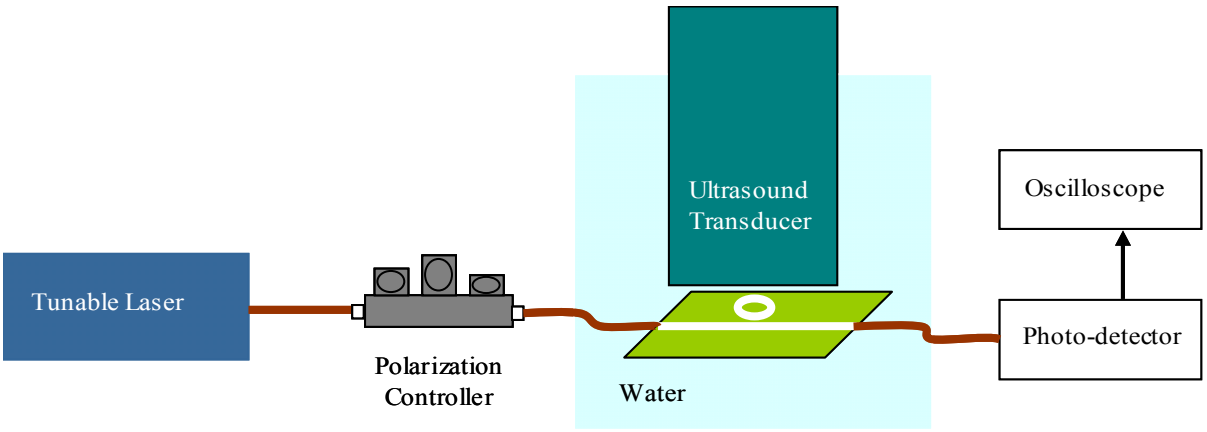

Figure 5.5 The experimental setup to measure the noise-equivalent pressure and sensitivity of a polymer microring resonator. the distance between the ultrasound transducer and the resonator was 1.5 mm.

The setup shown in Figure 5.5 was used to measure the NEP and sensitivity of a polymer micro-ring ultrasound detection device. A continuous-wave tunable laser source (HP 8168F, Agilent Technologies, Santa Clara, CA) was connected to the device's input fiber, and the output fiber was connected to a photodetector (1811-FC, New Focus, San Jose, CA), whose DC output has a gain of 1 V/A and AC output has a gain of $4*10^4$ V/A and an electrical bandwidth of 25kHz–125MHz. These photodetector outputs were connected to a digital oscilloscope (WaveSurfer 432, LeCroy, Chestnut Ridge, NY) for data collection. Using the DC output, we measured the device's transmission spectrum, of which one sample curve is shown in Figure 5.6(a), with an input power of 4.2 mW. The Q-factor was estimated to be 6,000. According to the off-resonance light transmission, 9% of the probing light was collected by the photodetector. A calibrated 20-MHz unfocused transducer (V316, Panametrics NDT, Waltham, MA) with a 3.18 mm diameter was used to insonify the ring. It outputs a peak pressure of 30 kPa around its

surface when driven by a peak-to-peak 10-V one-cycle 20 MHz sinusoidal wave. The acoustic coupling medium was deionized water. The optical probing wavelength and input power were set to 1555.51 nm and 5.5 mW, respectively. To measure the ultrasound signals, the AC output of the photodetector was used. Figure 5.6 (b) shows a recorded signal trace. The ringing following the main signal was due to reflections within the silicon substrate, which can be removed by changing substrate materials and/or structures. Since 30 kPa leaded to an output voltage of 332 mV, the corresponding shift of transmission spectrum was 6 pm according to its slope, and the sensitivity of the polymer microring ultrasound detection device was 11mV/kPa. The root-mean-squared noise levels were 1.5, 2.2, 2.5, and 3.0 mV over 1–25, 1–50 and 1–75, MHz, respectively, and the corresponding NEPs, a measure of the minimum detectable pressure of the device, were 0.14, 0.20, 0.23kPa.

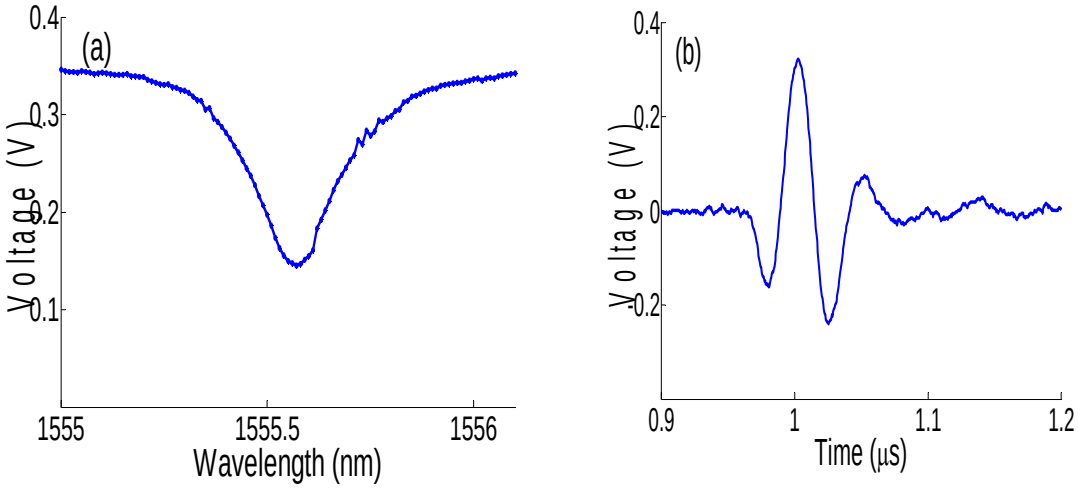

Figure 5.6 (a) Optical transmission spectrum of a polymer microring resonator. The input power was 4.2 mW. (b) Single-shot acoustic waveform measured by the resonator. The positive peak corresponds to 30 kPa. The optical probing wavelength and input power were set to 1555.51 nm and 5.5 mW, respectively.

Compared to the previous best result, 4.1 kPa over 5–75 MHz[78], we have improved NEP by more than one order of magnitude. The same level of NEP was

achieved using a Fabry–Pérot ROUT with a detection bandwidth of 20 MHz and a detector diameter of 50 μm.As a reference, a 75-μm piezoelectric PVDF transducer (HPM075/1, Precision Acoustics, Dorchester, Dorset, UK; http://www.acoustics.co.uk/products/hpm075-1) has an NEP of 6 kPa [=(60 μV)/(10 nV/Pa)] over a 100-MHz bandwidth even if noise only comes from a dedicated preamplifier (HP1, Precision Acoustics). In addition, polymer microring ultrasound detection devices' NEP can be further reduced by coupling more detection light in or increasing their Q-factor

5.4 Frequency response

A wideband optoacoustic source was realized to measure the detection bandwidth of a polymer microring ultrasound detection device. A 100-nm thick chromium film was deposited onto a glass substrate. Illuminating such a film with a wide-spot nanosecond laser pulse generates a planar optoacoustic wave with a temporal profile duplicating the exciting pulse shape (after vertical normalization) [79, 80]. In a short propagation distance, the wave can maintain its temporal shape and therefore be used as an acoustic source with a known spectrum. We put the chromium film 540 μm from a polymer microring ultrasound detection device and illuminated it using a 532 nm pulsed frequency-doubled Nd-YAG laser (Surelite I-20, Continuum, Santa Clara, CA) with a spot size of 4.5 mm in diameter. The acoustic coupling medium was deionized water. An acoustic signal detected by the device and a laser pulse profile detected by the same photodetector are shown in Fig. 5.7(a). Their close temporal durations suggest a short impulse response of the device. Figure 5.7(b) shows the signals' spectra together with the

estimated frequency response of the device, which was obtained by taking the difference of these two spectra to equalize the effects of finite laser pulse duration and photodetector bandwidth. The detection bandwidth of the P polymer microring ultrasound detection device was over 90 MHz at –3 dB.

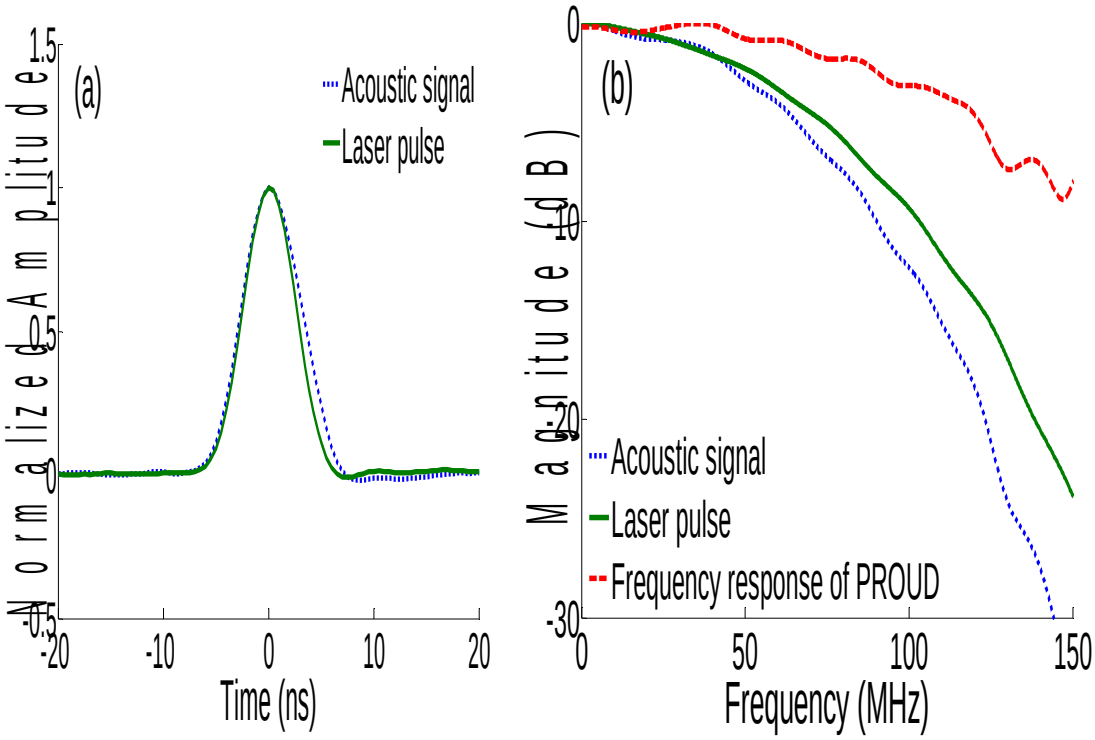

Figure 5.7 (a) Acoustic signal detected by a polymer microring resonator and laser pulse profile detected by the photodetector. (b) Spectra of the signals and frequency response of the resonator. The detection bandwidth of the resonator was over 90 MHz at –3 dB.

5.5 Device's performance Improvement

5.5.1 Fabrication process to improve Q factor

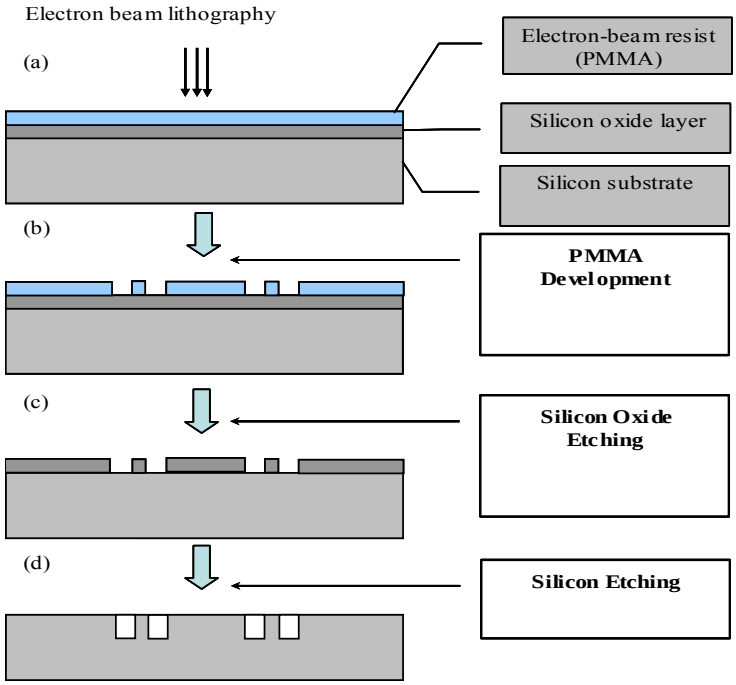

Figure 5.8 Schematic of typical silicon mold fabrication process

In order to fabricate high Q factor polymer micro-rings using nano-imprint technique, a mold with smooth sidewalls is needed. Many materials such as glass, polymer, metal, and silicon have been examined for mold applications. Among these materials, silicon is the most attractive material candidate due to the excellent processibility of silicon and a wide range of fabrication processes developed by the integrated circuit (IC) industry. Especially dry etching of silicon has been shown to achieve smooth and vertical sidewalls [81], which is ideal for our application. Our silicon mold is fabricated using electron beam lithography followed by reactive ion etch (RIE). Two important modification steps are used to further smooth the silicon mold sidewalls. The fabrication starts with a silicon

wafer with an initial 400 nm thermal oxide layer. Electron beam lithography is used to create a pattern with a micro-ring and a straight bus waveguide on a 800 nm thick positive electron-beam resist (950k PMMA). The patterns are then transferred to a silicon oxide layer using RIE with PMMA as the etch mask. After this step the PMMA mask is removed in hot acetone. The micro-ring pattern is further transferred onto the silicon wafer by deep silicon etching process with the silicon oxide layer as etch mask. After deep silicon etching, the silicon oxide masking layer is removed by buffered hydrofluoric acid (BHF), which completes the master mold fabrication (the schematic of the fabrication process is showing in Figure 5.8). Two important steps have been added to in this silicon mold fabrication process for getting smooth sidewalls.

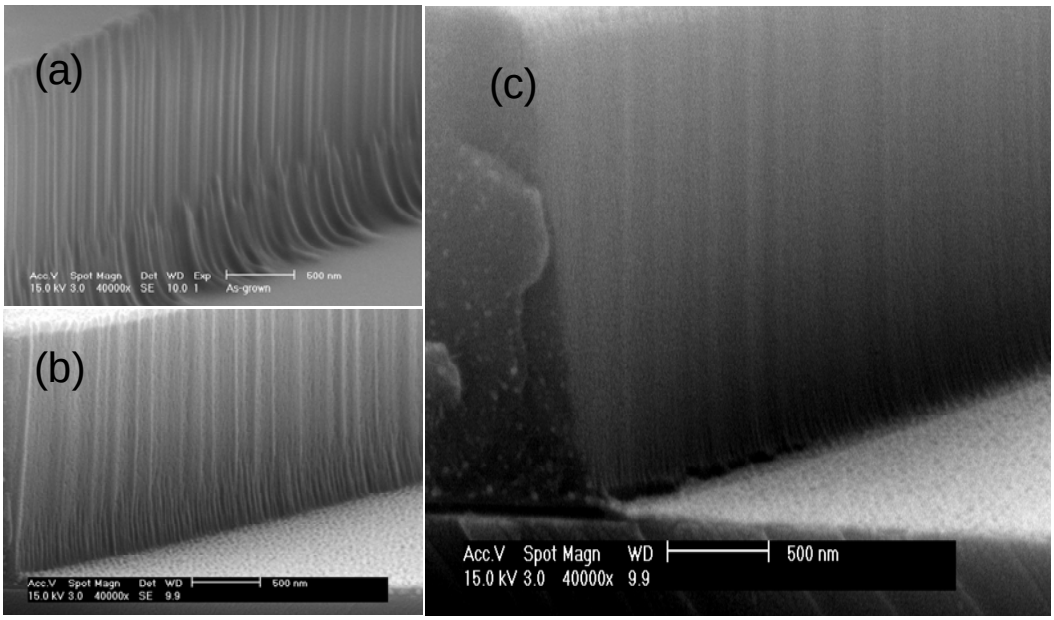

Figure 5.9 Sidewall SEM image of the polymer micro-ring fabricated from the mold: (a) without resist reflow process, (b) with resist reflow process, (c) with resist reflow and thermal oxidation process.

The first important step is the PMMA resist reflow, which is applied before the silicon oxide etch step. By choosing a suitable temperature and time duration, this reflow process can greatly reduce imperfections in the PMMA resist patterns and harden the

edge of the PMMA resist. Too low of a temperature will not cause the resist to reflow, while too high of a temperature will cause deformation in the coupling gap region, which could significantly increase the optical loss. After a number of experiments, the appropriate PMMA resist patterns reflowing temperature and time duration was determined to be 115^{o}C for 90 seconds. Figure 5.9 show the SEM pictures of imprinted polystyrene micro-ring waveguide sidewalls by using the silicon molds with (5.9b) and without (5.9a) PMMA resist reflow process, respectively. We can clearly see from Figure 5.9(a) that there is huge roughness on the sidewall of the polymer micro-ring, which is thought to be due to the damage caused by RIE on the edge of the PMMA pattern during etching of SiO2, which eventually gets transferred onto the silicon mold. However, in Figure 5.9(b), the sidewall of the polymer micro-ring fabricated from the mold with PMMA reflowing process has relatively small vertical roughness, which means that the edges of the PMMA are well protected during the RIE process.

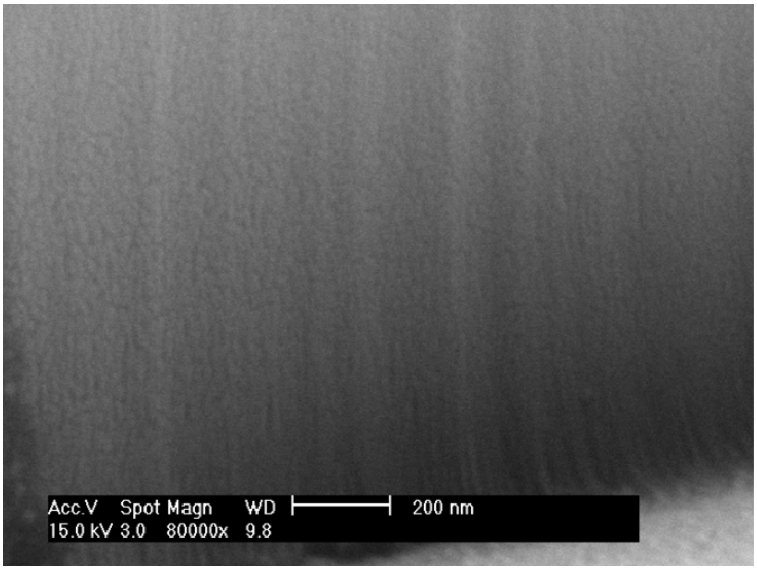

Figure 5.10, High magnification SEM picture of the sidewall roughness

The second important step is the thermal oxidation followed with BHF etching step,

which was used to smooth out the roughness after deep silicon etching. The oxidation step is performed in a high temperature furnace that grows around 100 nm thermal oxide on the silicon surface. As the oxidation consumes about 44% of Si, the rough Si surface layer is converted to SiO2 in this step and removed by BHF etching after the oxidation step. Figure 5.9(c) shows the sidewall of the imprinted polymer micro-ring using the silicon mold after thermal oxidation and BHF etching step. We see a major improvement in the sidewall roughness compared to Figure 5.9(b). Most of the sharp ripple-like roughness and small holes on the sidewall seen in Fig. 5.9(b) have disappeared in Figure 5.9(c) and figure 5.10.

5.5.2 Loss characterization

The Q factors of waveguide-coupled micro-rings can be classified as two components: $Q_{intrinsic}$ and Q_{couple}, where the former is the Q of an isolated resonator and the latter takes into account of the coupling loss to the bus waveguide. $Q_{intrinsic}$ is primarily limited by the optical losses in an isolated resonator, and can be attributed to these loss mechanisms: radiation loss, surface scattering loss, material absorption loss. Therefore the micro-resonator's overall Q factor can be expressed as:

$$\frac{1}{Q_{total}} = \frac{1}{Q_{intrinsic}} + \frac{1}{Q_{couple}} = \frac{1}{Q_{rad}} + \frac{1}{Q_{scatt}} + \frac{1}{Q_{abs}} + \frac{1}{Q_{couple}}, \qquad (4\text{-}1)$$

where Q_{rad}, Q_{scatt}, and Q_{abs} are radiation loss-related Q, surface scattering loss-related Q, and absorption loss-related Q, respectively. The total loss-related Q and coupling related Q can be extracted from the fitted transmission spectrum[82], the radiation related Q can be obtained from the simulation, the absorption loss-related Q can be measured from a

thermal bi-stability effect (will be described in more detail below), and finally the scattering related Q can be extracted from equation (4-1).

Figure 5.11(a) and 5.11(b) show the transmission spectrum of polymer micro-ring imprinted from the silicon mold without and with resist reflowing process, respectively. Figure 5.11 (a) shows the total Q of around 1×10^4, and Figure 5.11(b) shows the total Q of around 3×10^4. The amplitude attenuation factor can be obtained from micro-ring transmission equation, which can be expressed as:

$$T = \frac{\tau^2 + a^2 - 2a\tau\cos\phi}{1 + \tau^2 a^2 - 2a\tau\cos\phi}, \tag{4-2}$$

where τ is amplitude self-coupling coefficient, a is the amplitude attenuation factor, and ϕ is the round trip phase. The amplitude attenuation is due to the various optical losses in the micro-ring, and therefore can be used to obtain the $Q_{intrinsic}$. The amplitude attenuation factor a is related to the intrinsic Q from the following equation[83] :

$$Q_{\text{int}\,rinsic} = \frac{4\pi^2 R n_{eff}}{|2\ln a|\lambda_0} \tag{4-3}$$

where R is the radius of the micro-ring, n_{eff} is the effective refractive index of the resonance mode and λ_0 is the resonance wavelength.

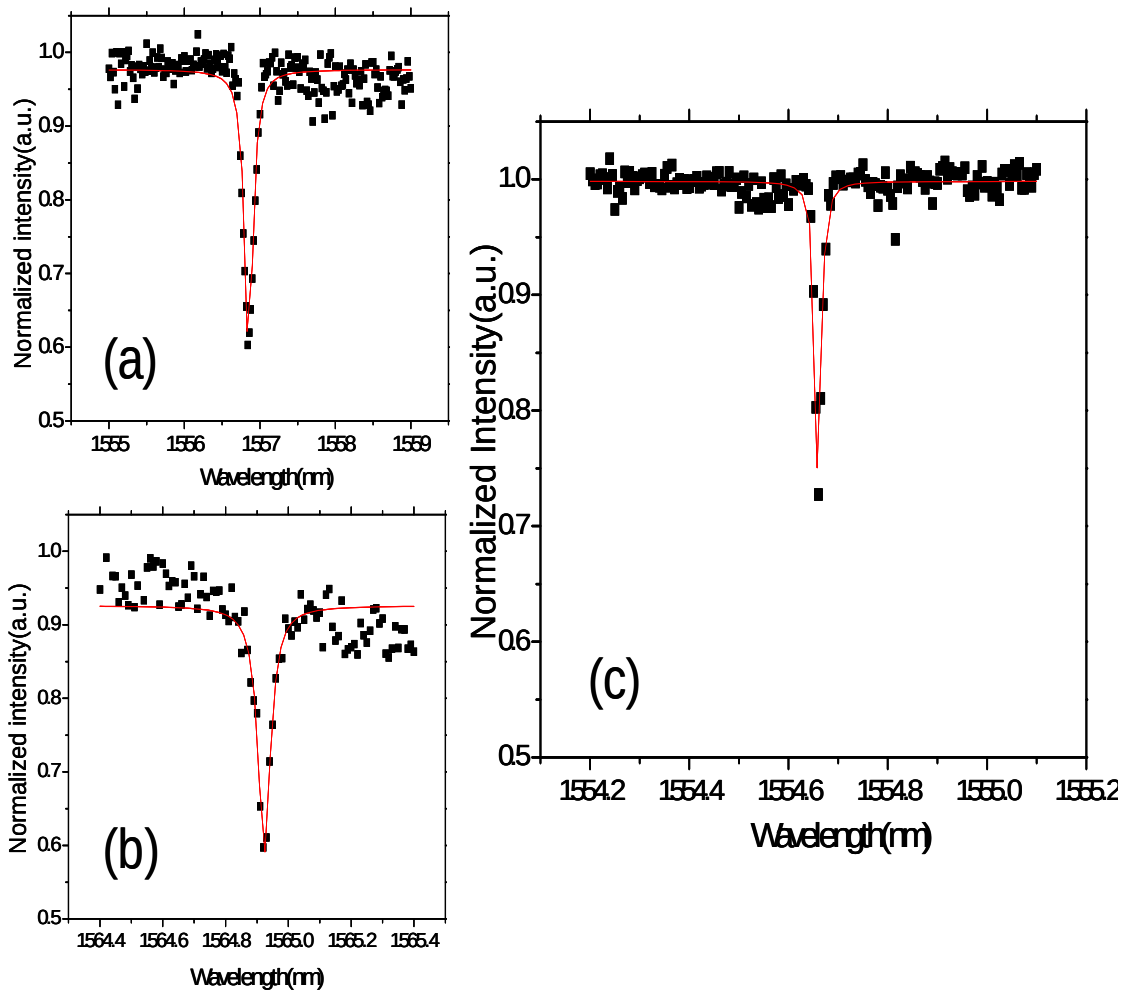

Figure 5.11.Transmission spectrum of polymer micro-ring fabricated from the mold (a) without resist reflow process, (b) with resist reflow process, (c) with resist reflow and thermal oxidation process. All the black dot curves are experimental data and red line curves are Lorentz fitting cure

By fitting with equation (4-2), we can get the amplitude self-coupling coefficient $\tau =$ 0.990 and the amplitude attenuation factor $a = 0.925$ for the micro-ring device fabricated using the mold without resist reflow process. The calculated intrinsic Q according to Eq (4-3) is around 1.2×10^4, corresponding to a propagation loss of around 22.7 dB/cm. For the device created from the mold with resist reflow process, we find that the amplitude self-coupling coefficient $\tau = 0.996$ and the amplitude attenuation factor $a = 0.975$. The

calculated intrinsic Q is around 3.5×10^4, corresponding to the propagation loss of 7.7 dB/cm. Therefore the resist reflow process can reduce the optical propagation loss by a factor of 3. Figure 5.11(c) shows the transmission spectrum of the waveguide coupled micro-ring devices fabricated from the mold made with the process including the resist reflow and thermal oxidation steps. The total Q is fitted to be around 1.1×10^5, and the amplitude self-coupling co-efficient $\tau = 0.99946$ and the amplitude attenuation factor $a = 0.994$. The intrinsic Q is calculated ~ 1.5×10^5, which represents propagation loss of 1.8 dB/cm. Thermal oxidation step further helps with reducing surface roughness leading to a total reduction of propagation loss by more than one order of magnitude.

COMSOL multi-physics software was used to simulate the radiation loss of the polymer micro-ring devices [84]. By taking the advantage of the axial-symmetry of the resonance modes in the micro-ring, the 3-dimensional eigenvalue problem can be transformed to an equivalent 2-dimensional problem. The exact dimensions of micro-rings and the refractive index of polymer, which are used in the simulation, are obtained from scanning electron microscope (SEM) and spectroscopic ellipsometry. By solving the eigenvalue problem in COMSOL, we obtained the eigen frequency for the transverse electrical mode's in the micro-ring with real part equal to 1.930625×10^{14} and imagery part equal to 1.00754×10^8 Hz. Therefore the radiation loss-related Q = $\mathrm{Re}(\omega)/2\mathrm{Im}(\omega)$ [85] is 9.6×10^5.

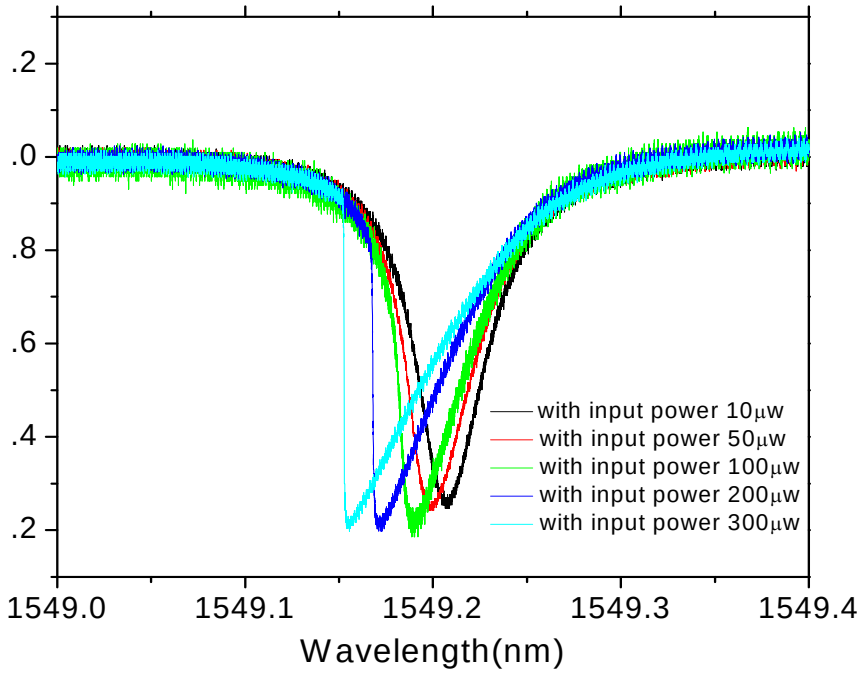

Figure 5.12.Transmission spectra of polymer micro-rings with different input power

To determine the absorption loss-related Q factor in the polymer micro-ring, we adopted a method based on the thermal-instability phenomenon of the polymer resonators. We measured the transmission spectrum for different input powers, and the results are shown in Figure 5.12. When increasing the input power, we found that the transmission spectra exhibit two notable changes: (1) resonance peak shift to a shorter wavelength, which is mainly due to the negative value of the opto-thermal coefficient of the polymer, and (2) distortion of resonance line shape, which is due to the material absorption induced thermal bi-stability effect [86]. The absorption loss-related Q can be extracted from the linear relation between the internal cavity energy and absorbed power by following the method described in reference 86. Assuming steady-state condition, the absorbed power in the cavity can be expressed $P_{abs}=\Delta T/R_{th}$, where ΔT is the temperature change from the cavity, and effective thermal resistance (R_{th}), which includes the thermal resistance of heat sink from the polymer cavity to ambient and thermal resistance of

cavity itself, was modeled using COMSOL multi-physics to be 9.5×10^3 W/K.

Then absorbed power then can be expressed as:

$$P_{abs} = \frac{1}{\lambda\left(\alpha + \frac{1}{n}\frac{dn}{dT}\right)R_{th}}\Delta\lambda \quad , \tag{4-4}$$

where n is the refractive index of the polymer, λ is the resonance wavelength, dn/dT is the thermo-optical coefficient，α is the thermal expansion coefficient and $\Delta\lambda$ is the resonance wavelength shift. Figure 5.13 shows the power dependence of absorption effect of the polymer micro-ring. The intra-cavity energy is calculated according to the reference 26. The linear absorption coefficient can be extracted to be 5.6×10^9 Hz, which can be used to calculate the absorption loss-related Q = 2.1×10^5[87]. This corresponds to a material absorption loss of 1.3dB/cm for polystyrene used for our devices, which is consistent to the published data [88].

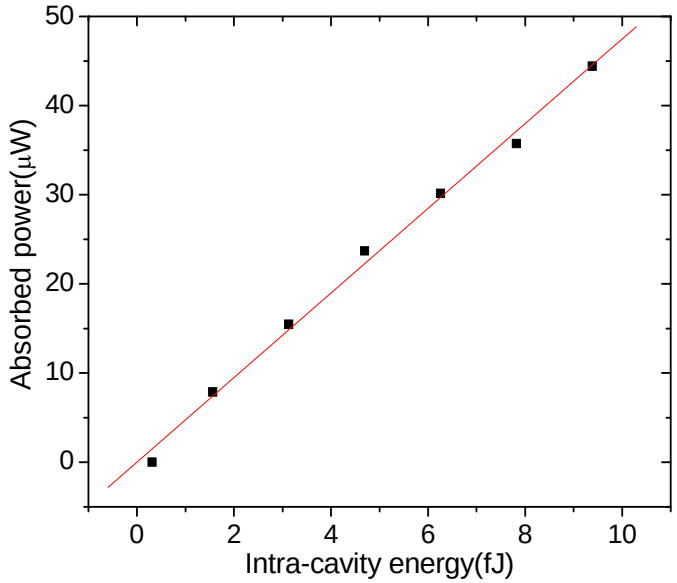

Figure 5.13.Transmission spectra of polymer micro-rings with different input power

Finally, the surface scattering loss-related Q can be calculated from the equation (4-1)

and is ~ 1.2×10^6, and the surface scattering loss can be shown as low as 0.23 dB/cm. From this analysis, we can know that the dominated loss in polymer micro-rings at 1.55 μm wavelength range is the material absorption loss (~1.3dB/cm), which is attributed to the carbon-hydrogen bonds harmonic absorption at near-IR range. Such absorption loss can be minimized by replacing H with F atoms. Fortunately, at visible wavelength range, polymer materials can have the absorption loss as low as 0.004dB/cm [89]. Therefore, we believe that our polymer micro-ring's total Q can be greatly increased by moving the working wavelength from NIR to the visible range.

5.5.3 Acoustic sensitivity

A 20 MHz unfocused transducer (V316, Panametrics NDT, Waltham, MA) was used to characterize the ultrasonic sensitivity of the high Q polymer micro-ring. During the experiment, the micro-ring device is immerged in de-ionized (DI) water used as a coupling media for acoustic wave. The device's transmission spectrum (Figure 5.14(a)) was measured in DI water with a Q factor of 2×10^4 and coupling contrast of 93% at resonance wavelength. The intrinsic Q of the polymer micro-ring in water is fitted to be 4×10^4, which is nearly 4 times lower than that in air. This reduction of Q is mainly due to the increase in bending loss due to reduced refractive index contrast between the waveguide core and the water cladding and absorption loss by the surrounding DI water. The transducer is driven by a 10 V peak-to-peak one cycle 20 MHz sinusoidal wave, outputting a peak pressure of 30 kPa, which was calibrated by a commercial hydrophone. The laser input was set at 1555.975 nm wavelength and the power at 5 mW. When the acoustic pressure pulse is hitting on the polymer micro-ring, it modulates the resonance

wavelength, thereby the output power at fixed probing wavelength. Figure 4.14(b) shows the recorded signal trace from a single-shot acoustic wave. The device produces an output of 1089 mV with an input of 30 kPa acoustic pressure, which means the device's acoustic sensitivity is around 36.3 mV/kPa. This is 3.3 times larger than what we recorded before using a device with Q of ~6000 and the same measurement system, including the laser, photodetecor, and oscilloscope. The root-mean-square noise levels were 1.8, 2.7, and 3.2 mV for 1–25, 1–50, and 1–75 MHz bandwidths, respectively. Thus, the corresponding NEPs are 51, 74, and 88 Pa for 1–25, 1–50, 1–75 MHz bandwidths, respectively. Therefore we have improved the NEPs nearly three times as compared with our previous best result of 230 Pa, which represents the highest sensitivity ultrasound transducer of similar physical size.

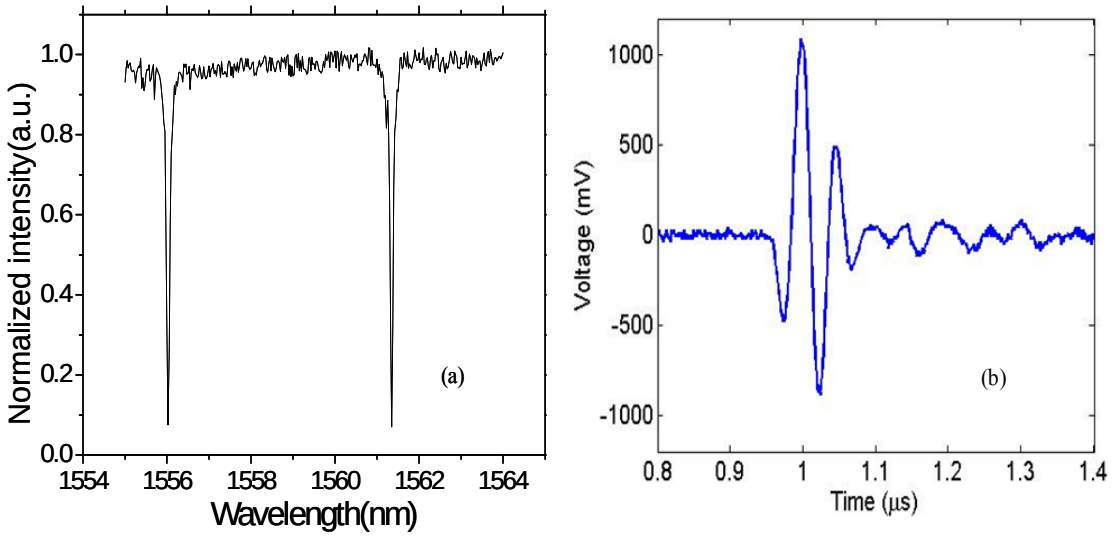

Figure 5.14 Transmission spectrum of polymer micro-ring immerged in DI water. (b) Single shot of acoustic waveform measured by high Q polymer micro-ring

5.6 Conclusion

A simplified fabrication process has been demonstrated to fabricate polymer micro-ring with more controllable coupling gap and roughness. This newly fabricated device has shown the Q factor around 6000. By using it as an ultrasound detector, a noise equivalent pressure of 0.23kPa over 1-75MHz and a detection bandwidth of over 90MHz at -3dB were measured. By further improving the fabrication process using resist reflow and thermal oxidation methods, we have successfully fabricated a silicon mold with smooth sidewalls. The imprinted devices can achieve an intrinsic Q factor as high as 1.5×10^5 in air, which corresponds to optical propagation loss of 1.8 dB/cm. Due to increased Q factor of the polymer resonator in water, we have obtained a noise equivalent pressure of 88 Pa over 1-75MHz which has improved around 3 times. Further reduction of NEPs is possible by making much higher Q polymer micro-rings..

Chapter 6

Ultra-high sensitive ultrasonic detectors using ultra-high Q microring

6.1 Introduction and motivation

Further improving our polymer microring detector's sensitivity to lower down device's detection limit as low as tens of Pascal will greatly benefit to *in vivo* photoacoustic imaging where a low laser energy is required for safety reasons [90]. In order to realize much higher sensitivity, a polymer microring detector with ultra-high Q factor is desired. But polymer materials' high absorption loss at near-IR range, which is attributed by the carbon-hydrogen bonds harmonic absorption, will prevent us to achieve ultra-high Q factor. One possible method to minimize polymer material's absorption loss is to replace hydrogen atom with fluorine atoms [91]. But by doping fluorine atom in the polymer, polymer material's refractive index will get decreased which will limit its application to form a compact device. Fortunately, at visible or near visible wavelength range, polymer material can have the very low absorption loss. Polymer material, such as PMMA, has been used to fabricate polymer optical fiber working around 800nm wavelength because of its low loss. Therefore, we believe that our polymer micro-ring's

total Q can be greatly increased by moving the working wavelength from NIR to the visible or near visible wavelength range.

Another advantage to move the working wavelength to near visible is that it can allow much small device size to realize similar Q factor compared to near IR wavelength range, which is good for high frequency ultrasound detection. To detect high-frequency ultrasound wave, a detector with both wideband response and small element size is needed. Small device size minimizes the spatial averaging effect for high-frequency waves, which is essential for high-resolution imaging. For example, phased-array imaging systems working at a center frequency of 30 MHz require $\lambda/2$ element size and spacing on the order of 25μm, where λ is the acoustic wavelength. Another example is that the small device size for tomographic imaging provides high resolution and high contrast over a large imaging region [92, 93]. Although the piezoelectric material polyvinylidene fluoride (PVDF) based needle hydrophones can reach the requirement of wide bandwidth and small element size (e.g., 40 μm (HPM04/01, Precision Acoustics, Dorchester, Dorset, UK)), the device lacks sufficient sensitivity: the noise-equivalent pressure (NEP) is relatively high ~10 kPa, and limits the imaging depth. Moreover, arrays with small element size and spacing and large element count, required for real-time imaging, are very difficult to realize using piezoelectric transducers because of the increased noise level, complexity of electrical interconnects and fabrication challenges. Optical microring detection of ultrasound could potentially address the above issues. It can achieve a low NEP with relative small element size and wideband response, and would be easier to create dense arrays with small element size.

6.2 Devices simulation and fabrication

Figure 6.1 shows the E field intensity of the polymer microring with R=30μm at resonance wavelength around 800nm.The polymer microrings (with refractive index around 1.585) with width and height are all equal to 1μm and it is sitting on the silica substrate with refractive index =1.45 with water as top cladding. From the figure, we still can see that some of the field is leaking down to the substrate region. The simulated radiation loss limited Q can be above 10^7, which is much higher than normal absorption loss limited Q. so we think the design the structure is good enough to realize higher Q factor.

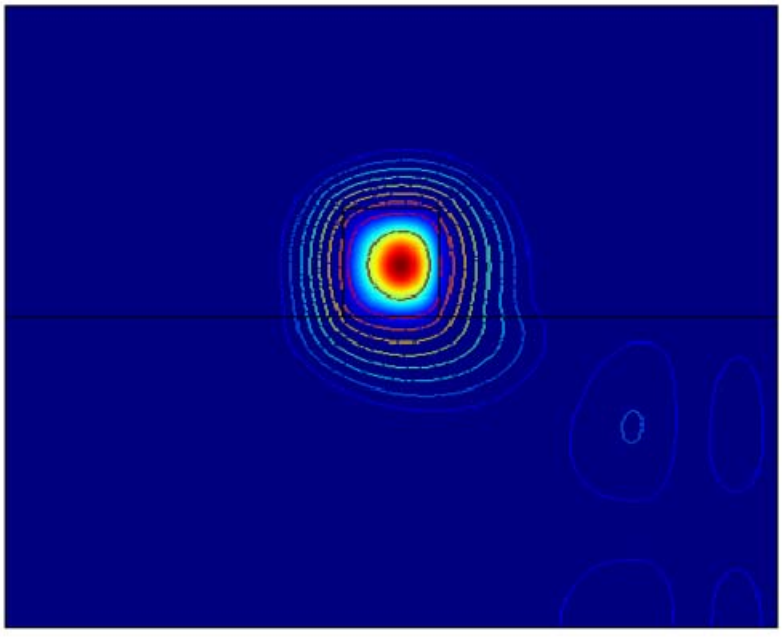

Figure 6.1 Simulated E filed intensity distribution of R=30μm polymer micro-ring at resonance wavelength around 800nm with bottom and top cladding are silica and water.

By switching working wavelength to a short wavelength, one potential problem is that it will increase the surface scattering. This is because that the scattering is proportional to $1/\lambda^4$. By switching the working wavelength from 1.55μm to 0.8um, it could potentially increase the surface scattering by 16 times. So further improving the device's sidewall roughness is desired. Also pervious we have demonstrated to use E-beam resist as an etch mask to etch silicon oxide, then use silicon oxide as an etch mask to etch Silicon. The problem is that the silicon oxide etching recipe requiring higher platen bias (above 50W) which will damage the resist mask during the etching process. Eventually, it will cause the roughness on the silicon mold. In order to solve this problem, we develop a new etching process by only using e-beam resists as an etch mask.

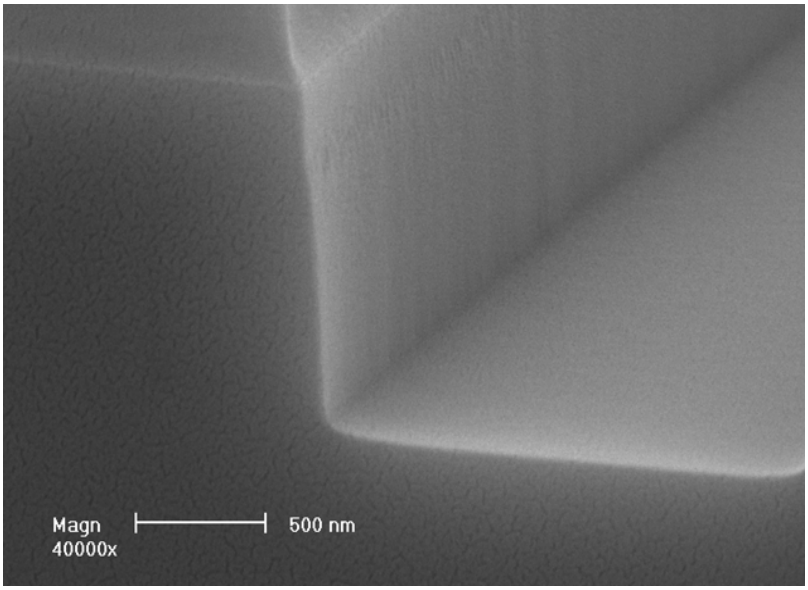

Figure 6.2 sidewall view of the silicon mold with new recipe

First resist reflow [86] process has been applied to harden the edge of the resist pattern to prevent potential damage during the reactive ion etch process. By choosing suitable temperature and time duration, this reflow process can greatly reduce imperfections in the PMMA resist patterns and harden the edge of the resist. Optimal temperature and heating

time were found to be 115°C and 90 seconds, respectively. Next the resist patterns were transferred into the silicon layer using SF_6 gas and C_4F_8 gas based inductively coupled plasma (ICP) reactive-ion etch (RIE) on a Surface Technology Systems (STS) deep silicon etcher system. A low platen bias was used in the etching recipe to reduce the damage to the reflowed PMMA mask and the SF_6 gas and C_4F_8 gas flow were optimized to minimize the sidewall roughness [94]. Figure 6.2 shows the etched silicon trench with the resist remained on top of the silicon trench. After RIE, the rest of PMMA mask is removed in hot acetone. A combination of resist reflow and modified Bosch process for Si etching are the keys to produce silicon master with smooth sidewalls

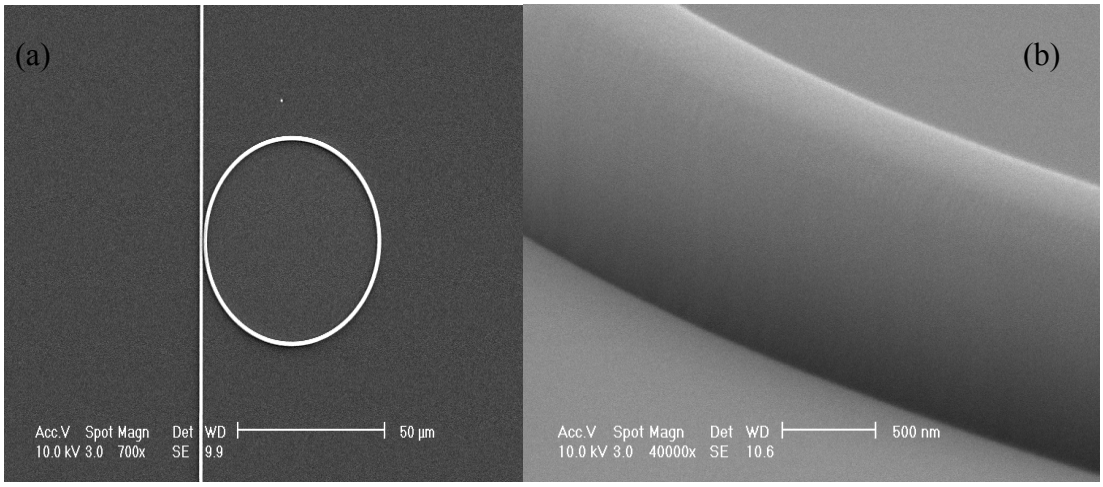

Figure 6.3 (a) SEM image of the polymer microrings with R=30μm, (b) SEM image of the sidewall of polymer micro-ring

The detail of using the nanoimprint process to create polystyrene micro-rings can be found in reference 10. Figure 6.3(a) shows the top view of a scanning electron microscopy (SEM) picture of a polystyrene micro-ring resonator with a diameter D = 60 μm coupled to a straight waveguide. Figure 6.3(b) shows the SEM picture of the sidewall of the imprinted polymer micro-ring. The smoothness is dramatically improved as compared with our previous results. The device's transmission spectrum was measured

using a tunable laser (New Focus TLB-6312) with tuning range from 765-781 nm. A single mode fiber (Nufern 780-HP) and a conventional multimode fiber were aligned to the input and output waveguide, respectively. The polarization of the input light was controlled by a fiber based optical polarization controller; and for consistency the input light was fixed as TE polarization. The output light signal from the multimode fiber was measured by a photo-detector. The measured transmission spectrum in de-ionized water (in Fig.6.4) shows a sharp resonance dip with a Q factor of 4×10^5. The device's intrinsic loss of 1.1 dB/cm is extracted from the transmission spectrum, which implies an intrinsic cavity Q factor of 5.1×10^5. The bending and leakage loss limited Q is obtained to be 10^7 and the material absorption limited Q can be also as high as 10^7, so we believe that the Q factor of our current 60 μm polymer micro-rings is still limited by the surface scattering loss, which can be further improved in the future.

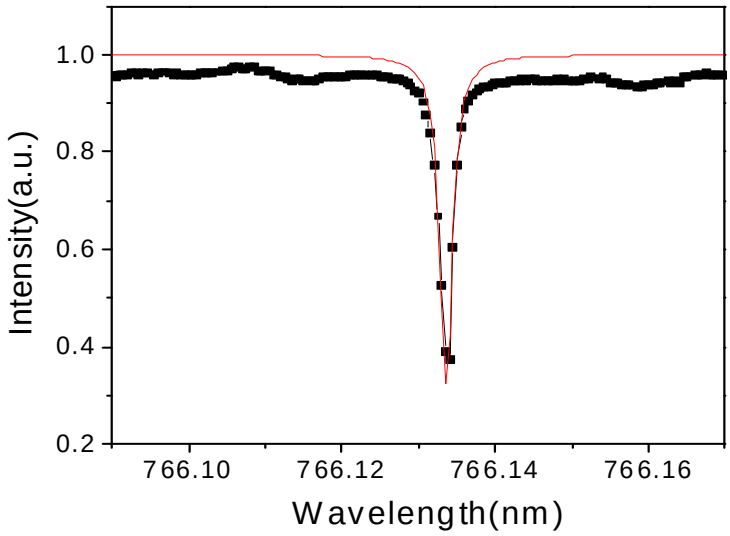

Figure 6.4 The transmission spectrum of polymer microring with R=30μm

6.3 Acoustic sensitivity

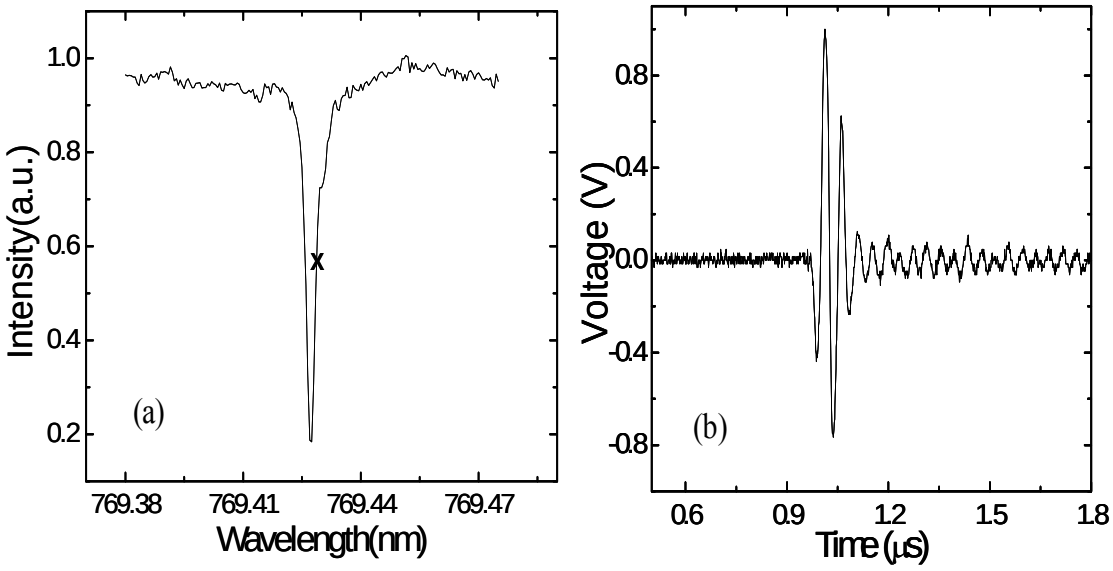

Figure 6.5 (a) Transmission spectrum of polymer micro-ring immerged in DI water. (b)Single shot of acoustic waveform measured by high Q polymer micro-ring

The experimental setup used to characterize the device's acoustic sensitivity is the same as in the last chapter. The micro-ring resonator detector was immersed in de-ionized water which served as top cladding of the micro-ring and coupling medium for acoustic wave. The output wavelength of light from the tunable laser was set to 769.4285 nm where the resonance transmission curve has the highest slope (in figure 6.5(a)) . The laser power from the input fiber was about 2 mW and a ~120 μW laser power was coupled into the input waveguide. The output power was collected by a multimode fiber which is connected a low-noise photodetector (New Focus, 1801-FC). The photo-detector output is connected to an oscilloscope to collect the data. A 20 MHz unfocused transducer (V316, Panametrics NDT, Waltham, MA), driven by a 5 V peak-to-peak one cycle 20 MHz sinusoidal wave with an output peak pressure of 15 kPa, was used to insonify the

micro-ring. When the acoustic pressure pulse hits on the polymer micro-ring, it modulates the resonance wavelength and thereby the output power at fixed probing wavelength. Figure 6.5(b) shows the recorded signal trace from a single-shot acoustic wave. The device produces an output of 1000 mV with an input of 15 kPa peak acoustic pressure, which means the device's acoustic sensitivity is around 66.7 mV/kPa. The root-mean-square noise levels were 0.7, 1.01 and 1.43 mV over 1-25, 1-50 and 1-75 MHz bandwidth, respectively, leading to NEPs of 10.5, 15.2 and 21.4 Pa at the corresponding bandwidth. Compared to our published best results, 88 Pa over 1-75 MHz, we have further improved the NEPs by over 4 folds. This result is 16 times better than the best Fabry-Perot cavity based optical ultrasound detector [95] and 300 times better than the similar size piezoelectric polyvinylidene fluoride (PVDF) transducer (HPM075/1, Precision Acoustics, Dorchester, Dorset, UK). Since our simulation results show that the device's intrinsic Q can be as high as10^7, we anticipate that the device's NEP can reach single digit Pa by further improving the fabrication and increasing the device's Q factor. Detectors with such ultra-low NEPs will directly benefit the ultrasound and photoacoustic imagingto significantly increase the imaging depth. It also pushes the photoacoustic imaging towards clinical applications on humans because much lower laser fluence is required.

6.5 Angular response

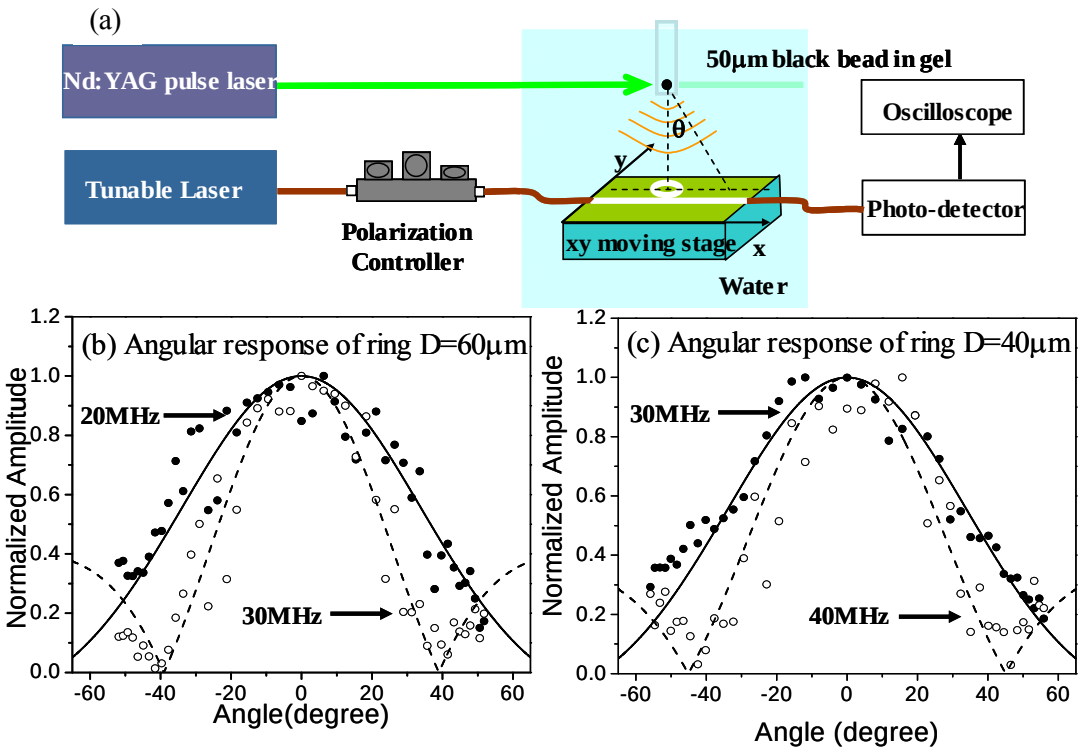

Figure 6.6 (a) Experimental setup for measure the angular response of the polymer micro-ring, experimental data (dot) and theoretical calculation (line) of angular response of the polymer micro-rings with D = 60 μm at 20 MHz (solid dot and line) and 30 MHz (empty dot and dash line) (b), and with D = 40 μm at 30 MHz (solid dot and line) and 40 MHz (empty dot and dash line) (c)

The angle-dependent sensitivity of the polymer microring was characterized using a photoacoustic method. Fig. 6.6 (a) shows the schematic of the experimental setup. A 50 μm polystyrene black bead embedded in the gel was illuminated by a pulsed, frequency-doubled Nd:YAG laser at 532 nm wavelength with pulse duration of 6 ns (Surelite I-20, Continuum, Santa Clara, CA). The energy from the pulsed laser was efficiently absorbed by the black bead, generating a spherical acoustic wave by the optoacoustic effect. The photoacoustic wave was then detected by the polymer microring detector at a distance of about 3 mm from the bead. The detectors, with diameters of 60

and 40 μm (detail will show in next section), are linearly scanned to receive the photoacoustic signals at different angles. Bandpass filters centered at different frequencies are applied to the recorded signals at different angles to extract the signal levels at those frequencies. The theoretical angular response can be described by considering a ring transducer: $D(\theta) = J_0(ka\sin\theta)$ [96], where k is the wave-vector of the incident acoustic wave, a the radius of the ring transducer and θ the incident angle of the acoustic wave. Fig. 6.6 (b) and (c) show the theoretical and experimental angular responses of the polymer microring with a diameter D = 60 and 40 μm, respectively. The theoretical curves fit well to our experimental data. Following similar calibration used for 60 μm micro-rings, the Q factor of 7×10^4 with water cladding and a NEP of around 0.1 kPa for 40 μm microrings were obtained. The worse NEP is because the bending-induced loss becomes dominant for 40 μm case.

For beam-forming applications, the detector's angular response should have -6 dB beamwidth of 40^o. Under this criterion, the microring detectors with D = 60 and 40 μm can be used as an imaging element for acoustic central frequency of 20 and 30 MHz, respectively. Compared to our previous polymer microring hydrophone with D = 100 μm, working around 10 MHz range, the new detectors have doubled and tripled the frequency range with better or similar sensitivity, corresponding to resolutions of 75 and 50 μm, respectively. The small size device will also benefit the tomographic imaging, enabling a uniformly high resolution and high contrast over a large region of interest. The details of high-resolution photoacoustic imaging applications using the ultra-low noise small size microring detectors can be found in our recent work.

6.6 Smaller size polymer micro-rings for high frequency imaging

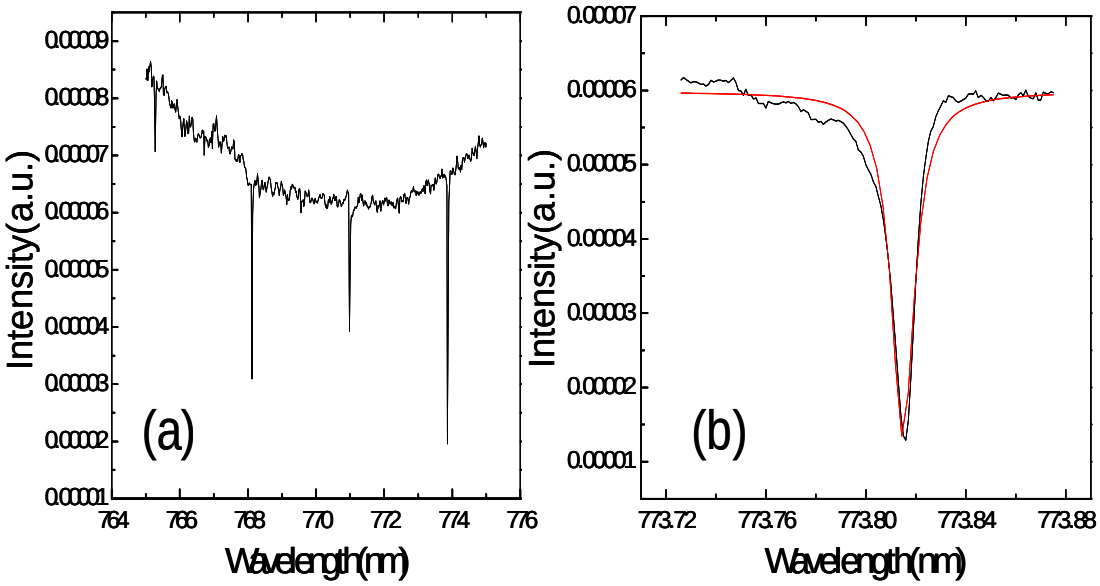

Figure 6.7 (a) The transmission spectrum of polymer microrings with R=20μm (coarse scan), (b) the transmission spectrum of polymer microrings with R=20μm (fine scan).

As we have shown in the pervious section that smaller size micro-ring detectors are good for high frequency ultrasonic imaging applications. This is because that small size device has larger angular response. By using same fabrication techniques that have used in the previous section, we have fabricated R=20μm polymer microrings with reasonable Q factor and sensitivity. Figure 6.7(a) shows the transmission spectrum of the R=20um polymer microring at coarse scanning mode. And figure 6.7(b) shows the transmission spectrum of one resonance mode at fine scanning mode. We can find that the device's Q factor is around $7x10^4$ in the water. The reduction of the Q is mainly due to the increasing of the bending loss at smaller device size. But with current Q factor, it is already good

enough to realize sensitivity high frequency image with detector NEP around 0.1kPa and larger angular response up to 30MHz frequency.

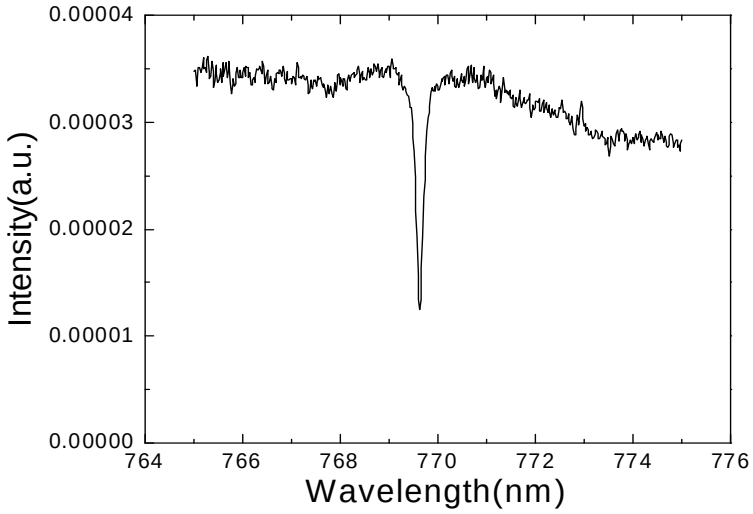

Figure 6.8 The transmission spectrum of polymer microrings with R=10μm (coarse scan) on 4μm thermal oxide wafer

In order to further increase the acoustic image resolution, a microring acoustic detector with a radius as small as 10μm has been developed, but with its compact size, it will suffer much larger leakage loss compared to large size (R≥20μm) device. The transmission spectrum of the imprinted polymer microring with device's R=10μm has been measured and shown in the figure 6.8. We can clearly see that after reducing the device's size, the free spectrum range of the resonator is increased and only one resonance mode is showing up within 12nm wavelength band-width. And the Q factor is indeed much worse than the device with radius R=20um and it is around $4\text{-}5\text{x}10^3$ in the water which translated to optical loss around 90dB/cm. With this Q factor ($4\text{-}5\text{x}10^3$), we can estimate the device's pressure detection limit is around 1.5kPa which is one order magnitude higher than the device with radius R=20um. This will limit the device's application in high sensitivity imaging applications.

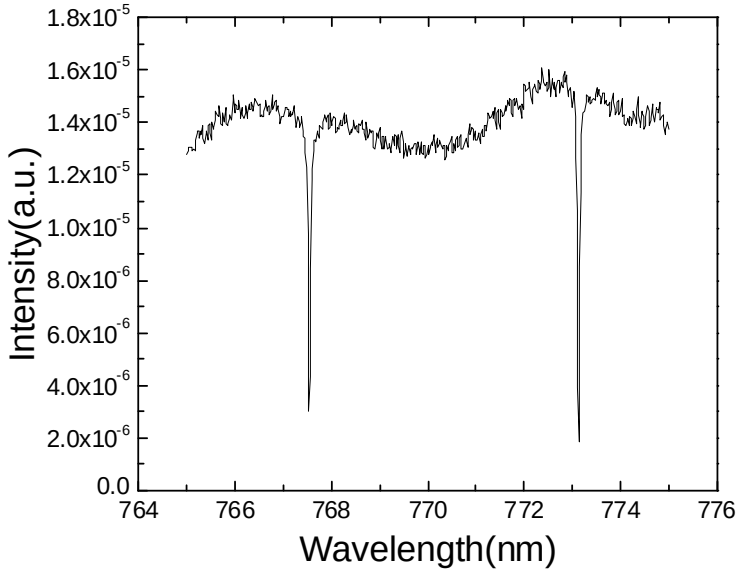

Figure 6.9 The transmission spectrum of polymer microrings with R=10μm on substrate with 400nm thick HSQ film on 4μm thermal oxide wafer.

One way to improve the device's Q is to use a much higher refractive index polymer material as the waveguide's core material, such as Poly(chloro-p-xylene) (n=1.629), Poly(vinyl phenyl sulfide) (n=1.6568), Poly(N-vinyl carbazole) (n=1.6863). But the problem is that those materials normally have very high glass transition temperatures (above 180^{o}C), which will prevent us to use the thermal nano-imprint process to fabricate mciroring devices. Also it is really hard to form a relative thick film (above 500nm) by normal spin coating method because of its low dissolution rate in the solvent. Therefore a conventional waveguide fabrication process, such as a photolithography combined with a dry etching process, will not fit for fabricating those high refractive index polymer waveguides. Another way to increase the device's Q factor is to reduce the refractive index of the bottom substrate. A couple of low refractive index materials can be considered as the candidates, such as HSQ (n=1.4), Cytop (n=1.34), SSQ (n=1.42). After

a few tests, we choose HSQ material as the low index material in our experiment. This is because the material's property is very stable after it is thermal cured.

The transmission spectrum of R=10um polymer microring fabricated on substrate with 400nm HSQ film on 4μm thermal oxide is shown in the figure 6.9, we can see that resonance dip's linewidth is much narrower than linewidth of the resonance dip in figure 6.8 and the Q factor of the device in the water can reach $2x10^4$ which is 5 time higher than the one without 400nm HSQ film in the bottom substrate.

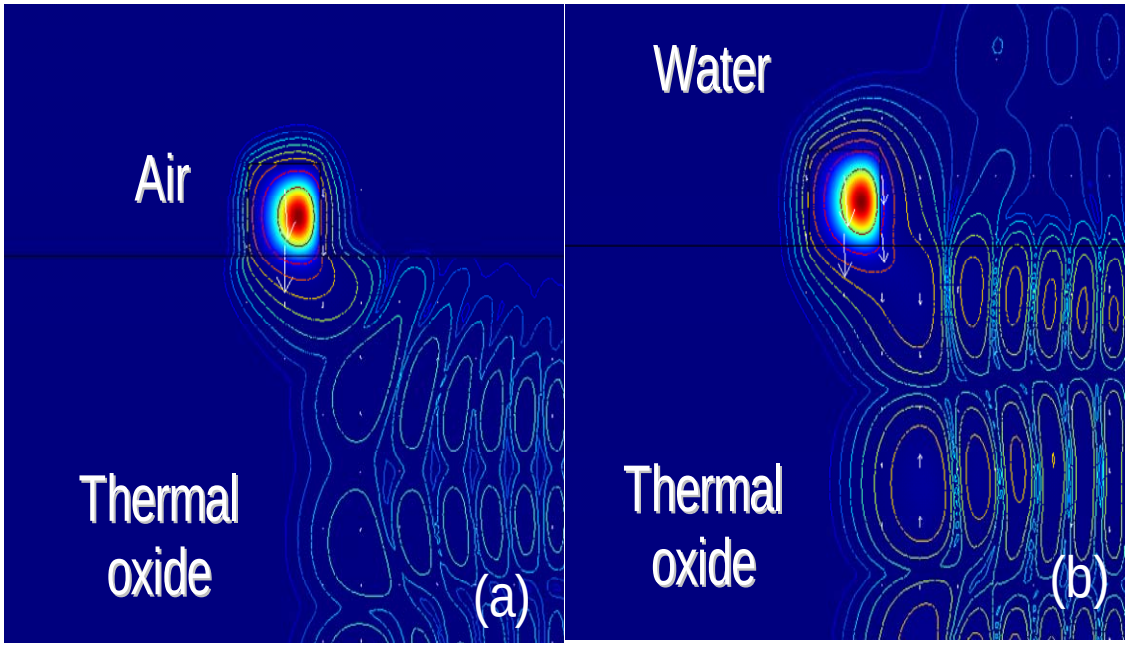

Figure 6.10 Simulated field distribution of R=10um polymer microring on thermal oxide substrate in the air (a) and in the water (b)

Another interesting way to reduce the device's bending loss is to hybrid the device with a metal. But directly fabricate the waveguide on the metal will cause too much loss to guide mode in the waveguide, one way to reduce the loss from the metal is to introduce a low index thin buffer layer between the waveguide material and metal. Figure 6.10 shows the simulated the field distribution in the air (a) and water (b) of the R=10um polymer microring on thermal oxide substrate. We can clearly see from figure 6.10(a)

that there is a large mount of optical field is leaking down to the substrate which is mainly due to the low index contrast between the polymer and thermal oxide. After the device is merged in the water, we can find from figure 6.10(b) that the leakage to the substrate is getting increased and also the leakage to the water also starts to show up. And the simulated Q in the air and water are $2x10^4$, $4x10^3$, respectively. Figure 6.11 shows the simulated results of the field distribution in water and air of R=10um polymer microring on the silicon substrate coated with a metal film and a 400nm low index buffer layer. As we have anticipated that the metal film really can help to reduce the leakage field to the bottom substrate, but it could increase the metal related absorption loss due to the presents of the metal film. The simulation shows that the after adding metal and low index buffer layer the Qs have been in improved to$3x10^5$ and $3x10^4$ in the air and water, respectively.

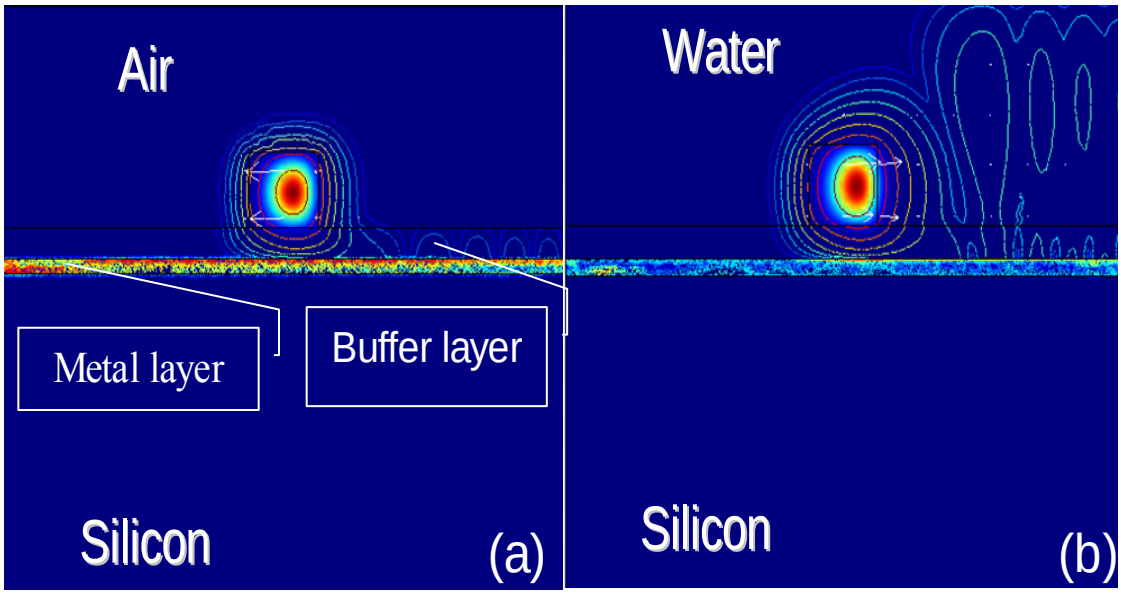

Figure 6.11 Simulated the field distribution of in water and air of R=10um polymer microring on the silicon substrate coated with a metal film and a 400nm HSQ buffer layer

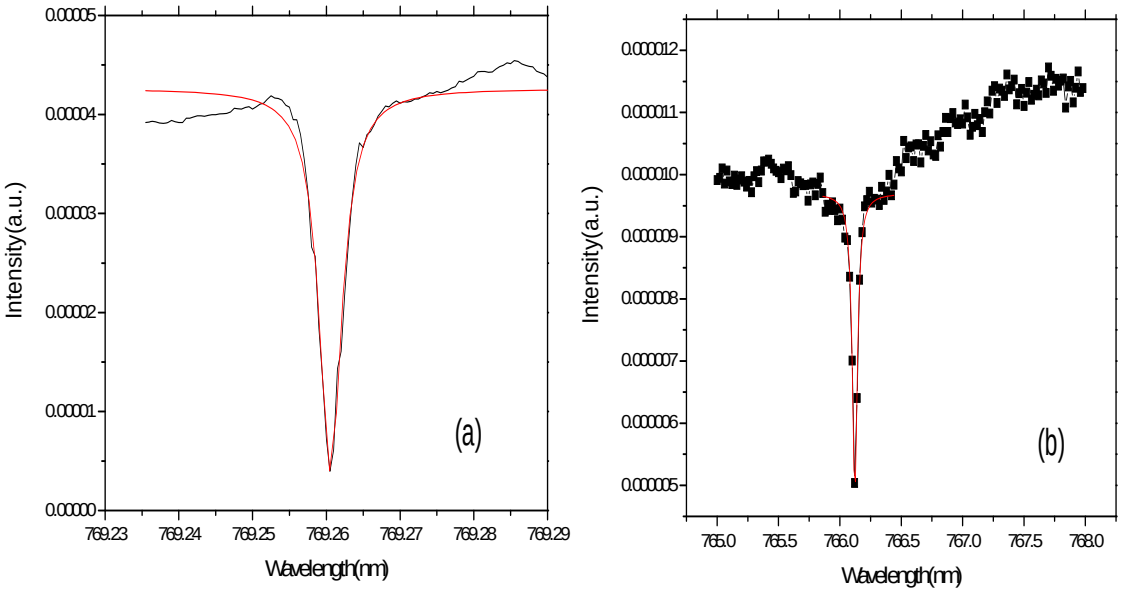

Figure 6.12 Transmission spectrum of R=10um polymer microring on the silicon substrate coated with a metal film and a 400nm HQS buffer layer in the air (a) and in the water (b).

The transmission spectrum (Figure 6.12) of f R=10um polymer microring on the silicon substrate with a metal film and a 400nm low index buffer layer has been measured in the air and in the water, respectively. In the air the device's Q factor is around $2x10^5$ and in the water the Q factor is around $2x10^4$, which matched well with the simulation results from the COMSOl. This metal hybrid with low index materials substrate has also been characterized to act as a substrate for ultrahigh Q device which has been fabricated on our previous sections in this chapter. Experimental measured device's Q in water is around $3x10^5$ (Figure 6.13) which is very close to the result we got from the device on 4μm thermal oxide substrate. This tells us that metal hybrid with low index polymer substrate can have the same or better confinement property compared to 4μm thermal oxide substrate. Another interesting thing is that it can be fabricated on various substrates, such as flexible plastic films and metal blocks. This makes it easy to fabricate low optical loss devices on flexible or metal substrates.

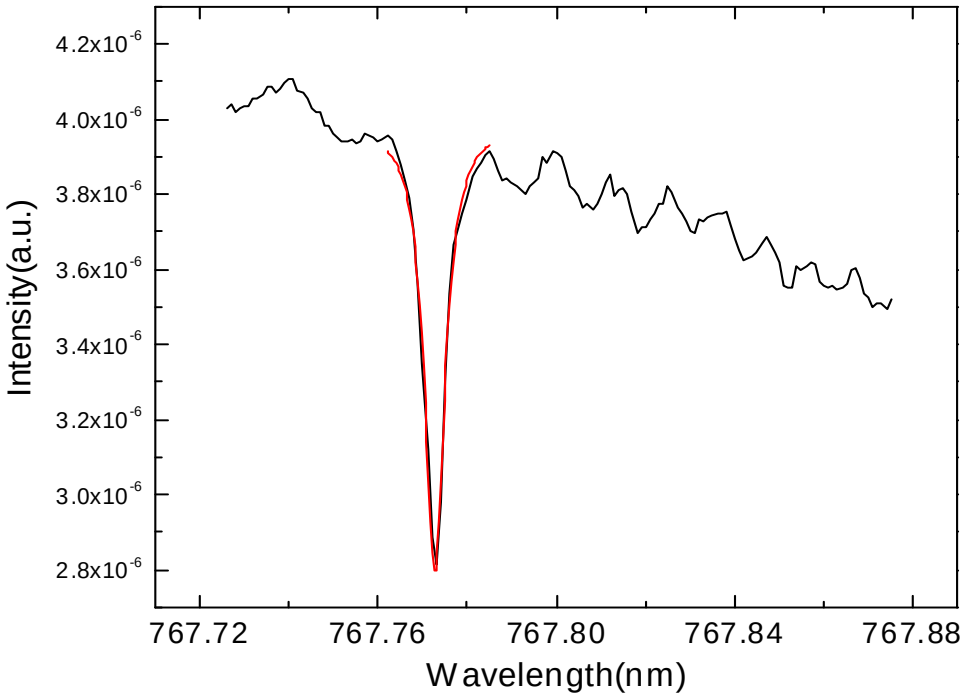

Figure 6.13 Transmission spectrum of R=30um polymer microring on the silicon substrate coated with a metal film and a 400nm low index buffer layer in the water

6.7 Photoacoustic microscopy using polymer microrings

With our current polymer micro-ring resonators detector's very wideband response and high sensitivity, we hope that micro-rings can provide high axial resolution in photoacoustic microscopy. In the experiment, a thin film optical resonator is used to replace the piezoelectric acoustic receivers. The inherent broad band frequency response of the optical thin film structure to acoustic waves, combined with a focused optical excitation beam can produce both axial resolution and lateral resolution comparable to that achieved in optical microscopy.

The left panel in Figure 6.14 presents the schematic of photoacoustic microscopy (PAM) setup based on the highly sensitive broad bandwidth microring resonator. The resonator has ring-shaped form coupled with a straight waveguide serving as optical input

and output. Such a microring detector has been shown to have an almost flat band response up to ~100 MHz. The microring resonator fabricated on a silicon chip was covered by a Mylar protective layer to screen out the exciting laser beam from a Nd:YAG laser (Spot-10-200-532, Elforlight Ltd, UK). The Nd:YAG laser working at 532nm wavelength has a pulse duration of 2 ns and a repetition rate (PRR) of 1KHz. The laser light was spatially filtered by an iris and then expanded to a parallel beam which was rastered over the tissue object by 2D Galvanometers. The intensity and the stability of the laser beam was monitored and calibrated by a photodiode (DET10A, Thorlabs, NJ). An achromatic lens with a focal length of 50 mm was used as the objective lens. On the Mylar protective layer, one coupling pad layer was used to optimize the coupling of the photoacoustic signal from the sample into the micro-ring resonator detector. A tunable laser (TLB-6312, NewFocus, CA) provided the light source for the micro-ring resonator at a wavelength tuned to the maximal slope of the resonance peak of the micro-ring's transmission spectrum. A low noise photodiode (1801-FC, New Focus, CA) was used to record the change of the intensity of the light through the micro-ring resonator which reflects the waveform of the photoacoustic signal. The photo-detector has a DC output gain of 1 V/mA and AC output gain of 40 V/mA with nominal -6dB electrical bandwidth of 25kHz-125MHz. Using the DC output, the microring's transmission spectrum can be measured. Throughout the experiment, a commercial calibrated Onda transducer (HNC-1500, Onda, CA) with -10dB bandwidth of 300 kHz-20 MHz was utilized to realize conventional PAM as a control to evaluate the performance of the PAM. The PAM with Onda transducer shared the same optical focusing and scanning components with microring based PAM. The Onda transducer operated on a reflection mode at a same

distance from the target as the microring resonator working on a transmission mode.

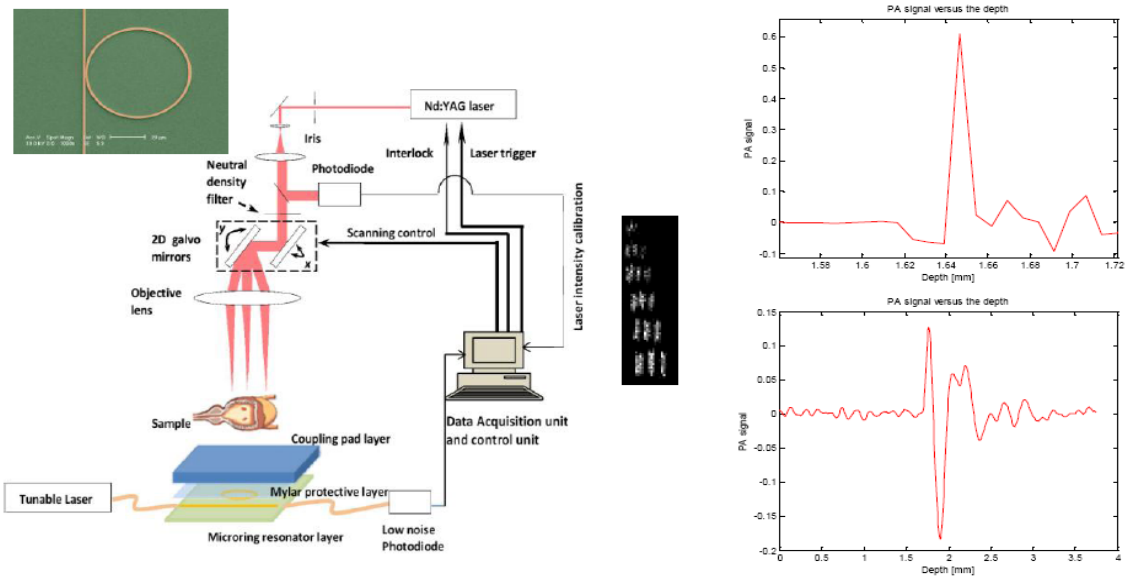

Figure 6.14 (left panel) schematic of a microring based PAM system based on a microring resonator. (middle panel) maximum amplitude projection (MAP) image of the USAF resolution template group 7. (right panels) A-line signals along the Z axis of the images of the USAF resolution template with a microring based PAM (right upper panel) and conventional PAM with Onda transducer (right lower panel). The inset at upper left shows a scanning electron micrograph of a polystyrene microring with 30 μm radius used in this experiment.

The microrings used in this study have a size of 60 μm in diameter and the polymer waveguides have a cross section of 1.4 × 1 μm^2. A single-mode and a multi-mode optical fiber were aligned with the input and output of the straight waveguide, respectively, and then fixed using UV curable epoxy. Polymer microring device is favorable in photoacoustic microscopy because of its ultra-low noise and broad bandwidth. A much lower noise equivalent pressure (NEP) compared with other types of optical resonant structures [97] has been demonstrated and further improvement of NEP is possible by designing much higher-Q device and/or by coupling more power into waveguides. From optical point of view, the detector's response time will be limited by the cavity's photon lifetime which is the time required for energy to decay to e^{-1} its original value and is

given by $\tau = Q/\omega$ [98]. Inverse of the response time will give the cut-off frequency. So our current device's frequency response can be up to 6.7 GHz. From acoustic point of view, a maximum modulation frequency of 570 MHz can be estimated considering the 1.4-μm-thick PS waveguide and the acoustic impedance of the cladding, polymer, and the substrate [99]. If assuming strong acoustic reflections from the rigid substrate and negligible reflections from the cladding-polymer boundary, an approximated formula gives a quick estimation on the bandwidth limit:

$$| P_l(k) | = \frac{2 | \sin(kl) |}{kl} \quad , \tag{6-1}$$

where P is the mean distribution of stress across the thickness *l* of the sensing film due to an normally incident plane acoustic wave with wave number *k*. The photoacoustic microscopy with microrings has the potential to achieve higher axial resolution if more broadband signals can be detected, which requires a photodetector with higher frequency response than used in the current experiment.

The lateral resolution of the microring based potoacoustic microscopy was measured by imaging an USAF resolution template (T-20-P-TM, Applied Image Inc, NY). The middle panel in Figure 6.14 shows the maximum amplitude projection (MAP) image of the resolution template, where the 6 bar elements of the group 7 can be resolved with the gaps up to 2.19 μm with modulation transfer function (MTF) value of 34%. Fitting the MTF to 50% yields a lateral resolution of 2.5 μm. The PAM with Onda transducer shows the same lateral resolution because they shares the same optical focusing and scanning architecture which determines the lateral resolution of the system. In tissue imaging, the lateral resolution will deteriorate mildly due to the optical scattering. However, when the

sample is optically thin (i.e. within one mean free path), the deterioration of the lateral resolution is insignificant [100]. To quantify the axial resolution, typical A-line signals extracted from the images of the USAF resolution template were used as approximations of axial point-spread-functions (PSFs). The right upper panel in Figure 6.14 depicts the axial PSF of microring based PAM; while the right lower panel in Figure 6.14 depicts the axial PSF of conventional PAM with Onda transducer. According to Rayleigh criterion, the PSFs show that this initial experiment of microring based PAM based on the microring resonator provided an axial resolution of 8 μm, close to the lateral optical resolution achieved; while PAM based on the Onda transducer gave a much larger axial resolution of 105 μm.

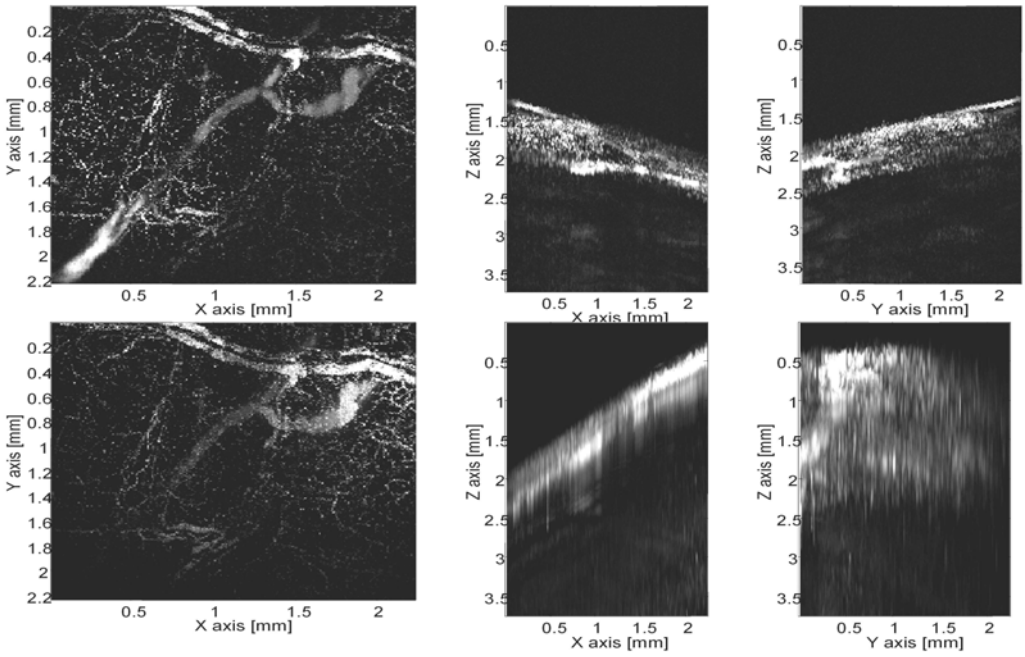

Figure 6.15 MAPs on XY,XZ, YZ planes of the ex vivo images of the vasculature in a mouse bladder wall acquired with AOPAM (upper row) using microring and conventional PAM using Onda transducer (lower row).

The bladder excised from CD1 mouse (CD1, Charles River, MA) was imaged ex vivo. The MAPs (Figure 6.15) of the images of the vasculature of the mouse bladder

acquired with microring based PAM (upper row) and conventional PAM with Onda transducer (lower row) show the same views in the sample, since the microring based PAM and PAM shared the same optical scanning and the sample was not moved between scans. MAPS on the XY planes acquired with microring based PAM and PAM render a consistent structure of the bladder vasculature with same resolutions. The difference of the contrast distributions between them is due to the different positions of the microring resonator and onda transducer, one working in transmission mode and another working in reflection mode. MAPS on the XZ and YZ planes acquired with PAM indicated a tail-trail from microscale vessels along the axial direction, initially thought to be due to the limited bandwidth of the Onda transducer. MAPS on the XZ and YZ plane acquired with microring based PAM indicated no tail-trail effect. The microscale capillary net with apparently large vasculature hiding in it can be clearly rendered. All the images in Figure 4.3 were acquired without averaging and proving maximum contrast to noise ratios of 26 dB for AOPAM and 29 dB for PAM. The commercial Onda transducer has a high sensitivity providing noise equivalent detectable pressure (NEDP) value of 19 Pa. The results of microring based PAM give an estimation of the sensitivity of microring resonator of NEDP value of 29 Pa, comparable with Onda transducer, much higher than other optical resonant structures available for acoustic measurement with NEDP on the order of magnitude of hundreds of Pascal. And this NEDP value is quiet close to the characterize device NEP (around 21Pa) in section 6.3.

6.8 Conclusion

Ultra-high Q polymer microring device has been realized by both switching the working wavelength to near visible wavelength where polymer material has lower absorption loss and further reducing the device's sidewall roughness to minimize the optical scattering loss. The device's Q as high as $4x10^5$ has been measured with device's radius R=30μm and again the detector's NEP has been characterized to be 21.4Pa over 1-75MHz frequency range. We have improved our device's NEP by over fourfolds. With our device's high sensitivity and broadband response, it greatly improved the photoacoutsic microscope's axial resolution to 8μm. Also high sensitivity, smaller size devices (R=20μm, and R=10μm) have been developed to improve the image resolution in beam forming imaging applications.

Chapter 7

Conclusion

7.1 Achievement in high sensitivity bio-chemical sensors

In this thesis, a prism coupled silica micro-tube bio-chemical sensor platform has been demonstrated for the first time to my knowledge. This platform not only overcome the device's reliability problem by using a thick wall silica micro-tube as a sensing element, but also realize high sensitivity detection by picking up higher order resonance modes in the silica micro-tube resonator. Compared to other demonstrated silica micro-tube sensors by using fiber coupled method with a wall thickness around hundred nanometers to few microns, our platform has realized high sensitivity sensing experiment with silica micro-tube wall thickness around 32μm. Even thicker wall also can be used in our sensing platform because of the nature of the prism coupled method which allows us to choose different orders of resonance modes in the micro-tube resonator. By tuning the incident angle to pick up different resonance mode which can be used to realize different sensitivity sensing functions.

In the bulk sensing experiment, we have successfully demonstrated device's sensitivity around 100nm/RIU at the incident angle around 37^{o} and this is typical belong to a sensitivity of a resonance mode with only evanescent wave in the liquid region (low index region). The optical wave in this mode is well confined at the inner and outer

boundary of the silica micro-tube by the total internal reflection which results in the evanescent wave at the outside of the silica region. By choosing a smaller incident angle, much higher order mode can be excited which could result in a much larger sensitivity. At incident angle at 35^{o}, we have observed a resonance mode with a sensing sensitivity around 600nm/RIU which is representing a resonance mode with more than 60 percent of the optical field located inside of the liquid region. The optical wave in mode is still well confined by total internal reflection at outer boundary, but due to the low index contrast between the silica and water Such a high sensing sensitivity has never been observed in normal micro-tube based sensor systems except one system has been demonstrated using extremely thin wall silica micro-tube (from zero to few hundred of nanometers). But the wet etching process used to thin down the wall thickness causes too much roughness on the surface and makes the device with very low Q factor. The silica micro-tube which was used in our experiment doesn't need any extra treatment and it maintains the same surface property as its coming out of the factory. With current Q factor around $2x10^{4}$ and high sensitivity around 600nm/RIU, we can claim that our device's refractive index detection limit is around $2.5x10^{-6}$. Further improve the Q factor by switching the device's working wavelength from near IR to near visible or visible rang to reduce water absorption can greatly lower down the device's refractive index detection limit to 10^{-8}.

In surface sensing experiment, first we characterized our device's bulk refractive index sensing property and then combined with the simulation results to pick up one resonance mode with relative high response to the surface binding. This resonance mode has been used to sense the binding of lipid monolayer, lipid bilayer and self assemble layer-by-layer to the inner surface of the silica micro-tube. With 4-5nm POPC lipid

membrane with refractive index around 1.46 absorbed on the inner wall, we can observe the resonance peak shift around 44pm. And in lipid monolayer experiment, we observed 22pm resonance wavelength shift which is the half of the shift in the lipid bilayer case. In the sensing electrostatic self assemble layer by layer experiment, the alternative coating of PDDA and Poly dye s-119 film has been observed with resonance wavelength shift at 9pm and 24pm, respectively. The reason of this difference is that the refractive index of poly dye s-119 is much higher than that of PDDA. Mie scattering simulation of the resonance peak shift due to the bio-chemical film absorbed onto the inner wall agrees very well with the experiment results. We also observed resonance peak shift with the membrane protein Annexin V and Alamethicin bonding to the lipid membrane. With the present Q factor 6×10^4 at 1.55μm wavelength, we estimate that our devices can detect the presence of 0.1nm thick absorbed film on the inner wall of the tube. The device's sensitivity can be greatly enhanced by switching the working wavelength from infrared wavelength to visible wavelength where water absorption is minimized.

In order to better understand the sensing property of the silica micro-tube, a theoretical study on various sensing properties, such as bulking refractive index sensing property, surface sensing property, absorption sensing property, have been provided. We found that the bulk refractive index sensing sensitivity increases with the radial order number in the evanescent sensing regime and oscillates in the non-evanescent sensing regime. The non-evanescent mode is particularly suitable for bulk refractive index sensing and the sensitivity can achieve around 600nm/RIU in our structure. The evanescent mode, having a high electric field magnitude at the inner boundary, is preferred in the surface sensing experiment with sensitivity as high as 10pm/nm. Also, a

high *Q* resonator sensor is desirable for absorption-based sensing. Also a coupled cavity platform, which can be realized by coating a low refractive index material at the inner surface of the silica microtube, was proposed to achieve device's bulk refractive index sensing sensitivity above 1000nm/RIU.

7.2 Achievement in high sensitivity ultrasonic sensors

Another important achievement in this thesis is to further improve polymer micro-ring resonators' performance in high sensitivity ultrasonic detection. By combining polymer's high optical elastic coefficient and high deformability which can provide a sensitive response under acoustic pressure with micro-rings' high Q factor, high sensitivity ultrasonic detection has been realized using polymer micro-rings fabricated by nano-imprint technique in our previous publications. But the fabrication process which involved shallow mold and deep mold fabrication result in too much variations on the coupling gaps and roughness on the sidewall of the ring waveguide. In order to make more repeatable process, we developed a simplified method to make a silicon oxide deep mold with reasonable Q factor around 6000. The simplified method replaced the lift-off process by directly etching the metal film with Cl_2 gas based reactive ion etching process which can generated more controllable gap and reasonable sidewall roughness. With the newly developed process, we can repeatedly achieve our polymer micro-ring devices with Q factor around 6000. By using calibrated transducer, our polymer microring detector has been characterized with relative low NEPs around 0.14, 0.20, and 0.23 kPa over 1-25, 1-50 and 1-75MHz, respectively. The device's NEPs are comparable to

state-of-art piezo-electric transducer with a similar size. By using a board band acoustic source generated by photo-acoustic method, the device's frequency responses of over 90 MHz at –3 dB were measured. Such a broadband detector could greatly benefit the high resolution ultrasonic image.

Further improved the device's NEP could play an important role in obtaining good imaging quality, especially for *in vivo* PA imaging where a low laser energy is required for safety reasons. We have developed a new fabrication process to enhance the device's performance by improving the Q factor of the polymer micro-ring. In this new developed process, two important steps have been added to reduce the sidewall roughness of the fabricated silicon mold. The first important step is the resist reflow process which could help to harden the edge of the resist and reduce the damage to the sidewall during the reactive ion etching process. The second step is the thermal oxidation process followed by buffered HF etching process, which will help to smooth out the roughness generated on the reactive ion etching process. By applying those two steps in the mold fabrication process, the imprinted polymer microring resonators with Q as high as 10^5 has been measured in the air. In the water the Q factor is around $2\text{-}3\text{x}10^4$ and the reduction of the Q is mainly due to the water absorption loss and reduced refractive index contrast induced bending loss. The device's NEPs have been measured around 51, 74, and 88 Pa for 1–25, 1–50, 1–75 MHz bandwidths, respectively. Therefore we have improved the NEPs nearly three times as compared with our previous best result of 230 Pa, which represents the highest sensitivity ultrasound transducer of similar physical size. We find that the device's Q is limited by the materials absorption loss, after a detail analysis of various optical losses in our current devices. Further improved the device's Q factor still

will be possible by switching the device's working wavelength from near IR to visible or near visible wavelength range where both water and polymer material have relative low absorption loss.

We can reduce the water and polymer material's absorption loss by switching the working wavelength to 780nm wavelength range, however the optical scattering loss will increased because it is proportional to $1/\lambda^4$. In order to further improve the device's Q factor, we not only have to switch the working wavelength, but also have to further reduce the surface scattering loss. So developing a process to fabricate microrings with a very smooth sidewall is the key to achieve a polymer micro-ring device with very low NEP. The developed fabrication process includes a resist thermal reflow process which has been used in our pervious devices fabrication process and optimized etching process. In the etching process, a low platen bias was used to reduce the damage to the reflowed PMMA mask and the SF_6 gas and C_4F_8 gas flow were optimized to minimize the sidewall roughness. The combination of resist reflow and modified Bosch process for Si etching are the keys to produce silicon master with smooth sidewalls. The imprinted polymer microring device with radius R=30μm has been measured with Q around $4x10^5$ and the device has been tested with NEPs of 10.5 Pa, 15.2 Pa, and 21.4 Pa for 1-25, 1-50, 1-75MHz bandwidth, respectively. We have improved our device's NEPs by over fourfolds. With our device's high sensitivity and broadband response, it greatly improved the photoacoutsic microscope's axial resolution to 8μm. Also the devices' relative small size (R=30μm, R=20μm, and R=10μm) can be used to improve the image resolution to 75μm, 50μm and 25μm in beam forming applications, respectively.

7.3 Future work

7.3.1 Ultra-small device

The small size device will greatly benefit the tomographic imaging, enabling a uniformly high resolution and high contrast over a large region of interest. Using the single-element low-noise small size detector with linear translation stages, we have shown high-resolution photoacoustic imaging applications by synthetic one-dimensional and two-dimensional microring arrays. But it is really hard to make a smaller size polymer microring device (R<10μm) with relative high Q factor, because polymer materials relative low refractive index (typically <1.6) is not good at confining optical wave when it starts to bend too much. But if we can hybridize the polymer material with high index materials, such as silicon (n=3.5) or silicon nitride (n=2.0), it will be very promising to realize devices size as small as R=5μm or R=2.5μm with relative high Q factor. Figure 7.1 shows a silicon slot waveguide hybridize with polymer material with bending radius R=5μm and we can clearly see that optical field is well confined even with a 5μm bending radius. With such a compact device size, we could further improve the beam forming imaging resolution down to few microns.

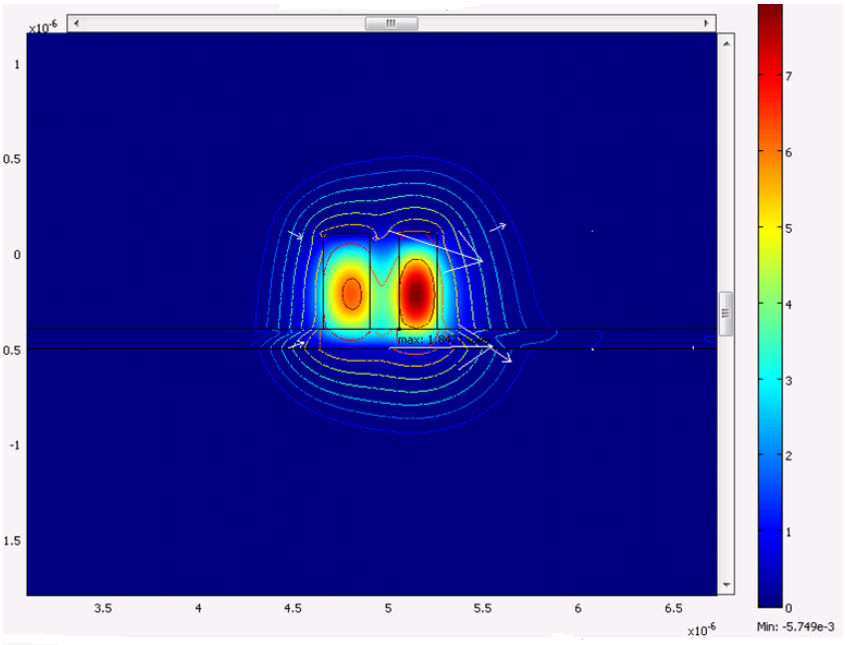

Figure 7.1 shows a silicon slot waveguide hybrid with polymer material with radius R=5μm

7.3.2 Ultra-high Q factor device

Only PMMA has been demonstrated with very low absorption loss and polymer micro-resonator made by PMMA can achieve Q factor up to 10^8 at visible wavelength range. But due to PMMA material's relative low refractive index (n=1.49), it will be very difficult to fabrication a compact size device with ultrahigh Q factor. But ultra-high Q factor can be realized with devices size above 500μm. Another promising way is to make an ultrahigh silicon nitride slot waveguide ring resonator covered by PMMA. By pushing the device's Q factor up to 10^6, we could reduce our devices' NEPs down to 10Pa which could greatly lower down the required pump power in real photoacoustic imaging applications.

7.3.3 Acoustic detectors on fiber tip

In order to improve the our polymer microring acoustic probe for more clinical application, such as photoacostic endoscopy, more advanced design to further reduction of size are needed. One proposed idea is to fabricate the polymer microring on the fiber tip. In order to realize that, the input and output waveguide need to merge together to form a single input and output device. Also an optical grating is needed to be fabricated on the input/output part to couple the light from vertical direction to in-plane. Another possible way is to fabricate polymer coated high Q optical grating on the fiber tip to act as the high sensitivity acoustic detector. The excitation laser need be carried by another optical fiber which could put just beside the optical fiber with the polymer microring or optical grating detector on the tip.

7.3.4 Micro-ring arrays for imaging applications

Two-dimensional ultrasonic detector arrays are really good for real time high resolution three dimensional imaging applications. Normal high-frequency piezoelectric 2D array would naturally suffer from larger noise level and fabrication complexities due to large element count and small element size and spacing. Optical arrays can be a great candidate to realize small element size and larger array numbers. We have demonstrated polymer microring with size around D=20μm with the Q factor around $3x10^4$. With such a small device size (D=20μm) the free spectrum range of the microring is about 6.25nm and the device's Q factor of $3x10^4$ can be translated to full wave half maximum of resonance peak about 0.026nm. So 240 channels can be made within 6.25nm free

spectrum range, which also means we can make a 14x14 2-D microring arrays by using our current devices. Furthermore, much smaller device's size and much higher Q factor can be achieved by using polymer hybridized with silicon or silicon nitride microring structures. Suppose we can have a polymer hybridized silicon microring with D=5μm (free spectrum range 50nm) and Q factor can be easily realized around $5x10^4$ (full wave half maximum of resonance peak around 0.03nm). 1666 channels can be placed in one free spectrum range of the microring and a 40x40 2-D microring arrays can be realized by utilizing 1600 microring devices.

Bibliography

1. E.A.J. Marcatili, Bends in optical dielectric guides. Bell System Technical Journal, 48, pp.2103-2132 (1969)
2. R.E. Benner, P.W. Barber, J.F. Owen, R.K. Chang, Observation of structure resonances in the fluorescence-spectra from microsphere. Physical Review Letters, 44, pp.475-4780(1980)
3. S.X Qian, J.B Snow., H.M Tzeng., R.K Chang, Lasing droplets-highlighting the liquid-air interface by laser-emission. Science, ,231, pp.486-488 (1986)
4. S.L. Mccall, A.F.J. Levi, R.E. Slusher, S.J. Pearton, R.A. Logan, Whispering gallery mode micro-disk lasers, Applied Physics Letters, 60, pp.289-291 (1992)
5. B.E. Little, et al, Micro-ring resonator channel dropping filters. Journal of lightwave Technology, 15, pp.998-1005 (1997)
6. S.T. Chu, et al., Second-order filter response from parallel coupled glass microring resonators, IEEE Photonics Technology Letters, 11, pp.1426-1428 (1999)
7. M. Cai, G. Hunzike, K. Vahala, Fiber-optic add-drop device based on a silica microsphere whispering gallery mode system, IEEE Photonics Technology Letters, 11,pp. 686-687 (1999)
8. S.T. Chu, et al, An eight-channel add/drop filter using vertically coupled microring resonator over a cross rid. IEEE Photonics Technology Letters, 11,pp.691-693 (1999)
9. J. Djordjev, et al, Microdisk tunable resonator filters and switches, IEEE Photonics Technology Letters, 14,pp.828-830 (2002)
10. D.X. Dai, L. Yang, and S.L. He, Ultrasmall thermally tunable microring resonator with a sub-micrometer heater on Si nanowaires, Journal of Lightwave Technology, 26, pp.704-709 (2008)
11. F. Vollmer, et al, Protein detection by optical shift of a resonant micro-cavity, Applied Physics Letters, 80, pp.4057-4059 (2002)
12. R.W. Boyd and J.E Heebner. Sensitive disk resonator photonic biosensor. Applied Optics, 40, pp.5742-5747 (2001)
13. E. Krioukov, et al, Sensor based on an integrated optical microcavity, Optics Letters, 27, pp.512-514 (2002)
14. C.Y. Chao, and L.J. Guo, Biochemical sensors based on polymer microrings with sharp asymmetrical resonance, Appl. Phys. Lett., 83, pp.1527-1529 (2003)
15. I.M White., H. Oveys, and X.D. Fan, Liquid core optical ring resonator sensors, Optics Letters, 31, pp.1319-1321 (2006)
16. V.S. IIchenko, et al, Coupling and tenability of optical whispering gallery mode—a basic for coordinate meter, Opt. Commum., 107, pp.41-48 (1994)
17. S.W. Huang, S.L. Chen, T. Ling, A. Maxwell, M. O'Donnell, L.J. Guo, S. Ashkenazi, Low-noise wideband ultrasound detection using polymer microring resonators, Appl. Phys. Lett. , 92, pp.193509 (2008)

18. S. Ashkenazi, C.Y. Chao, L.J. Guo, and M. O'Donnell, Ultrasound Detection Using Polymer Microring Optical Resonator, Appl. Phys. Lett. , 85(32), pp. 5418-5420 (2004)
19. J.C. Knight et al, Core resonance capillary fiber whispering gallery mode laser, Optics Letters, 17, pp.1280-1282 (1992)
20. L. Yang and K.J. Vahala, Gain functionalization of silica microresonators, Optics Letters, , 28, pp.592-594 (2003)
21. S.M. Spillane, T.J Kippenberg. and K.J. Vahala, Ultralow threshold raman laser using a spherical dielectric microcavity, Nature, 415, pp.621-623 (2002)
22. A.B. Matsko, et al, On cavity modification of stimulated raman scattering, J.Opt.B., 5,pp.272-278 (2003)
23. M. Haraguchi, et al, Optical switching due to whispering gallery mode in dielectric microsphere coated by a Kerr material, J. Microscopy, 201, pp.229-233 (2003)
24. V. Van, et al, All optical nonlinear switching in GaAs-AlGaAs microring resonators, IEEE Photon. Techno.l Lett. , 14, pp.74-76 (2002)
25. V.S. IIchenko, et al, Sub-micro Watt Photonic Microwave receiver, IEEE Photon. Tech. Lett., 14, pp.1602-1604 (2002).
26. L.R. Brothers, et al, Terahertz optical frequency comb generation and phase locking of an optical parametric oscillator at 655 GHz, Optics Letters, 19, pp.245-247 (1994)
27. T.J. Kippenberg, et al, Kerr-nonlinearity optical parameteric oscillation in an Ultrahigh-Q Toroid Microcavity, Physical Review Letters., 93, pp.083904 (2004)
28. T. Carmon and K. J. Vahala, Visible continuous emission from a silica microphotonic device by third harmonic generation, Nature Physics, 3, pp.430-435 (2007)
29. T. Carmon, H. Rokhsari, L. Yang, T.J. Kippenberg, and K.J. Vahala, Temporal behavior of radiation-pressure-induced vibrations of an optical microcavity phonon mode, Physical Review Letters 94, pp. 223902 (2005)
30. C.Y. Chao, W. Fung, and L. J. Guo, High Q-Factor Polymer Microring Resonators for Biochemical Sensing Applications, IEEE Special Topic in Quantum Electronics., 12, pp.134-142 (2006)
31. I. M. White, J.D. Suter, H. Oveys, X.D. Fan, Universal coupling between metal-cald waveguide and optical ring resonators, Opt. Express, 15 ,pp.646-651 (2007)
32. A. Yalcin, K.C. Popat, O.C. Aldridge, T.A. Desai, J. Hryniewicz, B.E. Little, O. King, V. Van, S. Chu, D. Gill, M. Anthes-Washbun, M.S. Unlu and B.B. Goldberg, Optical sensing of biomolecules using Microring resonators, IEEE J. Sel. Top. Quantum Electron.,12, pp.148-155 (2006)
33. V. Zamora, A. Díez, M.V. Andrés and B. Gimeno, Refractometric sensor based on whispering gallery modes of thin capillaries, Opt. Exp. ,15, pp.12011-12016 (2007)
34. H. Nakano, Y. Matsuda, S. Nagai, Ultrasound detection by using a confocal Fabry-Perot interferometer with phase-modulated light, Ultrasonic, 37, pp.257-259 (1999)
35. S. Ashkenazi, Y. Hou, T. Buma, M. O'Donnell, Optoacoustic imaging using thin polymer etalon, Appl. Phys. Lett. , 85, pp.134102 (2005)
36. P.C. Beard and T.N. Mills, Miniature optical fibre ultrasonic hydrophone using a Fabry-Perot polymer film interferometer, Electronic Lett.,33, pp.801-803 (1997)
37. E.Z. Zhang and P. Beard, Ultra high sensitivity, wideband Fabry Perot ultrasound sensors as an alternative to piezoelectric PVDF transducers for biomedical

photoacoustic detection, Proc. of SPIE, ,5320, pp.222-229 (2004)
38. M. Cai, O. Painter, K.J. Vahala, P.C. Serecel, Fiber-couple microsphere laser, Opt. Lett., ,25, pp.1430-1432 (2001)
39. M. Borselli, K. Srinivasab, P.E. Barclay, O. Painter, Rayleigh scattering, mode coupling, and optical loss in silicon microdisks, Appl. Phys. Lett., 85, pp.3693-3695 (2004)
40. T.J. Kippenberg, S.M. Spillane, D.K. Armani, K.J. Vahala, Fabrication and coupling to planar high-Q silica disk microcavities, Appl. Phys. Lett. , 83, pp.797-799 (2003)
41. A. Gondarenko, J.S. Levy and M. Lipson, High confinement micro-scale silicon nitride high Q ring resonator, Opt. Exp., 17, pp.11366-11370 (2009)
42. P. Rabiei, W.H. Steier, C. Zhang, L.R. Dalton, Polymer micro-ring filters and modulators, J. Light. Tech. , 20, pp.1968-1975 (2002)
43. H.S. Sun, A.T. Chen, B.C. Olbricht, J.A. Davies, P.A. Sullivan, Y. Lian and L.R. Dalton, Direct electron beam writing of electro-optic polymer microring resonators, Opt. Exp., ,16, pp.6592-6599 (2008)
44. T. Ling, L.J. Guo, A unique resonance mode observed in a prism-coupled micro-tube resonator sensor with superior index sensitivity, Opt. Exp.,15, pp.17424-17432 (2007)
45. L. Rayleigh, The Problem of the Whispering Gallery, Philosophical Magazine, 20, pp.1001–1004 (1910)
46. J. D. Jackson, *Classical Electrodynamics*, 2nd ed. (John Wiley & Sons, Inc., New York, NY, 1975)
47. A. Yariv and P. Yeh, *Photonics: Optical Electronics in Modern Communications*, 6th ed., Oxford University Press, New York, 2007
48. B. E. Little and S. T. Chu, Estimating surface-roughness loss and output coupling in microdisk resonators, Optics Letters, 21, pp.1390-1392 (1996)
49. J. P. R. Lacey and F. P. Payne, Radiation loss from planar waveguides with random wall imperfections, IEE Proc. Pt. J., 137, pp. 282-288, (1990)
50. P.P. Absil, Ph.D. Dissertation: Microring resonators for wavelength division multiplexing and integrated photonics applications, (2000)
51. V. Van, et al., Propagation loss in single-mode GaAs-AlGaAs microring resonator: measurement and model, Journal of Lightwave Technology, 19, pp.1734-1739 (2001)
52. M. Tomes, K. J. Vahala, T. Carmon, Direct imaging of tunneling from a potential well, Optics Express, 17, pp.19160 (2009)
53. D. Marcuse, Bending losses of asymmetric slab waveguide, Bell system Technical Journal, , 50, p. 2551-2563 (1971)
54. A.M. Armani, A Srinivasan, and K.J. Vahala, soft lithography fabrication of high Q polymer microcavoty arrays, Nano Letters, 7,pp.1823-1826 (2007)
55. J.R. Schwesyg, T., Beckmann A.S. Zimmermann, K. Buse, and D. Haertle, Fabrication and characterization of whispering-gallery-mode resonators made of polymers, Opt. Exp., 17, pp.2573-2578 (2009)
56. H. Li and X.D. Fan, Characterization of sensing capability of optofluidic ring resonator biosensors, Applied Physics Letters, **97**, 011105 (2010)
57. W. Liang, Y.Y. Huang , Y. Xu, R.K. Lee, and A. Yariv, High sensitive fiber Bragg grating refractive index sensors, Appl. Phys. Lett. ,86, pp.151122 (2005)
58. C.F. Bohren, D.R. Huffman, Absorption and scattering of light by small particles

(Wiley, 1998)
59. P.W. Barber, S.C. Hill, *Light Scattering by Particles: Computational Methods* (World Scientific 1990), Chapter 2.
60. H.J. Moon, K. An, Interferential coupling effect on the whispering-gallery mode lasing in a double-layered microcylinder, Appl. Phys. Lett. 80,3250-3252 (2002)
61. J. W. Park and G.U. Lee, Properties of Mixed Lipid Monolayers Assembled on Hydrophobic Surfaces through Vesicle Adsorption, Langmuir, 22(11), pp.5057-5063, (2006)
62. X. Cheng,, and L.J., Guo, Electrostatic self assembly of nanocompostite polymer in garting structure , J. Vac. Sci. Technol. B,19, (2001)
63. S. Majd, D.J. Estes, M. Mayer, Assays for studying annexin binding to artificial bilayers, Calcuim Binding Proteins, 1, pp.26-29 (2006)
64. D. Voges, R. Beredes, A. Burger eta la. Three-dimensional structure of membrane-bound annexin V:A, correlative electron microscopy X-ray crystallography study, J. Mol. Biol, , 238 ,pp.199-213 (1994)
65. C. Kaduk, H. Duclohier, M. Dathe, H. Wenschuh, M. Beyermann, M. Molle, and M. Bienert, Influence of Proline Position upon the Ion Channel Activity of Alamethicin, Biophysical Journal, 72, pp.2151-2159, 1997
66. I. Teraoka and S. Arnold, Enhancing the sensitivity of a whispering gallery mode microsphere sensor by a highrefractive index surface layer, J. Opt. Soc. Am. B. ,23, pp.1434–1441 (2006)
67. I. Teraoka and S. Arnold, Theory of resonance shifts in TE and TM whispering gallery modes by nonradial perturbations for sensing applications, J. Opt. Soc. Am. B, 23, pp.1381–1389. (2006)
68. X. D. Fan, I. M. White, H. Y. Zhou, J. D. Suter, and H. Oveys, Overview of novel integrated optical ring resonator bio/chemical sensors, Proc. SPIE 6452, pp.64520M (2007).
69. O. Gaathon, J. Culic-Viskota, M. Mihnev, I. Teraoka and S. Arnold, Enhancing sensitivity of a whispering gallery mode biosensor by subwavelength confinement, Appl. Phys. Lett. 89, pp.223901 (2006).
70. M. Sumetsky, R. S. Windeler, Y. Dulashko, and X.D. Fan Optical liquid ring resonator sensor, Optics Express 15, pp.14376-14381 (2007)
71. Q. H. Song and H. Cao, Improving Optical Confinement in Nanostructures via External Mode Coupling, Phys. Rev. Lett., 105, pp.053902 (2010)
72. Y.F. Xiao, C.L. Zou, B.B. Li, Y. Li, C.H. Dong, Z.F. Han, Q. Gong, High-Q exterior whispering-gallery modes in a metal-coated micro-resonator, Phys Rev Lett., 105, pp.153902. (2010)
73. Y.Z. Sun and X.D. Fan, Analysis of ring resonator for chemical vapor sensor development, Optics Express, 16, pp. 10254-10268 (2008)
74. N. Lin, L. Jiang, S.M. Wang, H. Xiao, Y.F. Lu and H.L. Tsai, Design and optimization of liquid core optical ring resonator for refractive index sensing, Applied Optics, 50, pp. 3615-3621 (2011)
75. J. Wiersig, Formation of Long-Lived, Scarlike Modes near Avoided Resonance Crossings in Optical Microcavities, Phys. Rev. Lett. 97, pp.253901 (2006)
76. C. Y. Chao and L. J. Guo, Polymer Micro-ring Resonators Fabricated by Nanoimprint Technique, J. Vac. Sci. Technol. B 20(6), pp.2862–2866 (2002).

77. C.Y Chao, Ph. D. thesis, Polymer Microring Resonator and Its Application as a Biosensor, 2005.
78. A. Maxwell, S.-W. Huang, T. Ling, J.-S. Kim, S. Ashkenazi, and L. J. Guo, Polymer Microring Resonators for High-Frequency Ultrasound Detection and Imaging, IEEE Journal of Selected Topics in Quantum Electronics, 14(1), pp.191 (2008)
79. T. Sun and M. I. Khan Photoacoustic Monopole Radiation in One, Two, and Three Dimensions,Phys. Rev. Lett. 67, pp.3384 (1991)
80. T. Buma, M. Spisar, and M. O'Donnell, Thermoelastic generation of ultrasound using an erbium doped fiber amplifier, Proc.-IEEE Ultrason. Symp., pp. 1253-1256 (1999)
81. H. C. Liu, Y. H. Lin, and W. Hsu, Sidewall roughness control in advanced silicon etch process, Microsyst. Technol., 10, 29–34 (2003).
82. C. Y. Chao, and L. J. Guo, Reduction of Surface Scattering Loss in Polymer Microrings Using Thermal-Reflow Technique, IEEE Photon. Technol. Lett. 16, pp.1498–1500 (2004).
83. K. J. Vahala, *Optical Microcavities* (World Scientific 2004), Chapter 7.
84. M. Oxborrow, How to simulate the whispering gallery modes of dielectric microresonator in FEMLAB/COMSOL, Proc. SPIE 6452, pp.64520J-12 (2007).
85. R. K. Chang, and A. J. Campillo, *Optical Processes in Microcavities* (World scientific 1996), Chapter 6.
86. V. R. Almeida, and M. Lipson, Optical bistability on a silicon chip, Opt. Lett. 29, pp.2387–2389 (2004)
87. M. Borselli, T. J. Johnson, and O. Painter, Beyond the Rayleigh scattering limit in high-Q silicon microdisks: theory and experiment, Opt. Express, 13, pp.1515–1530 (2005),
88. R. G. Hunsperger, *Integrated Optics: Theory and Technology* (Springer Science and Business Media 2009), Chapter 5.
89. J. R. Schwesyg, T. Beckmann, A. S. Zimmermann, K. Buse, and D. Haertle, Fabrication and characterization of whispering-gallery-mode resonators made of polymers, Opt. Express, 17, pp.2573–2578 (2009)
90. H. F. Zhang, K. Maslov, G. Stoica, and L. V. Wang, "Functional photoacoustic microscopy for high-resolution and noninvasive *in vivo* imaging," Nat. Biotechnol., 2, pp.848–851 (2006)
91. M.C. Oh, et al., Integrated Photonic Devices Incorporating Low-Loss Fluorinated Polymer Materials, Polymers, 3, pp.975-997 (2011)
92. M.H. Xu and L.V. Wang, Analytic explanation of spatial resolution related to bandwidth and detector aperture size in thermoacoustic or photoacoustic reconstruction, Phys. Rev. E 67, pp.056605 (2003)
93. S.L Chen, T. Ling, and L. J. Guo, Low-noise small-size microring ultrasonic detectors for high-resolution photoacoustic imaging Journal of Biomedical Optics,16, pp. 056001 (2011).
94. F. Gao, Y. Wang, G. Cao, X. Jia and F. Zhang, improvement of sidewall surface roughness in siliocn-on-insulator rib waveguide, Applied Physics B: Lasers and Optics, 81, pp.691-694 (2005)
95. S. Ashkenazi, Y. Hou, T. Buma, and M O'Donnell, Optoacoustic imaging using thin polymer etalon, Appl. Phys. Lett., 86, pp.134102 (2005)
96. D. T. Blackstock, Fundamentals of Physical Acoustic (Wiley, New York, 2000).

97. E. Zhang, J. Laufer, and P. Beard, Backward-mode multiwavelength photoacoustic scanner using a planar Fabry-Perot polymer film ultrasound sensor for high-resolution three-dimensional imaging of biological tissues, Appl. Opt., 47, pp. 561-577 (2008).
98. D.K. Armani, T.J. Kippenberg, S.M. Spillane and K.J. Vahala, Ultra-high-Q toroid microcavity on chip, Nature, 421, pp. 925-928 (2003)
99. P. C. Beard and T. N. Mills, Extrinsic optical-fiber ultrasound sensor using a thin polymer film as a low-finesse Fabry-Perot interferometer, Appl. Opt., vol. 35, pp. 663–675 (1996)
100. K. Maslov, H. F. Zhang, S. Hu, and L. V. Wang, Optical-resolution photoacoustic microscopy for in vivo imaging of single capillaries, Opt. Lett., 33, pp. 929–931 (2008)